Aberration-corrected high-resolution transmission electron microscopy of the misfit layered compound $(PbS)_{1.14}NbS_2$

Dissertation

zur Erlangung des akademischen Grades
Doktor der Naturwissenschaften
(Dr. rer. nat.)

der Technischen Fakultät
der Christian-Albrechts-Universität zu Kiel

Magnus Garbrecht

Kiel

2008

1. Gutachter	Prof. Dr. Wolfgang Jäger
2. Gutachter	Prof. Dr. Werner Mader
Datum der mündlichen Prüfung	17. 4. 2009

Zusammenfassung

Konventionelle und aberrations-korrigierte Hochauflösungs-Transmissionselektronenmikroskopie (HRTEM) sowie Raster-TEM (STEM) und Elektronenbeugung (ED) wurde in dieser Arbeit experimentell auf den Fehlanpassungsschichtkristall $(PbS)_{1.14}NbS_2$ angewendet.

Ziel war es, die individuellen Atomsäulenpositionen an den Grenzflächen des Systems mit einer Präzision im sub-Ångstrom Bereich bestimmen zu können. Mit der so erreichten Genauigkeit in der Bestimmung von Atomsäulenabständen sollten quantitative Auswertungen an Modulationen der atomaren Struktur sowie Inhomogenitäten des Gitters entlang der Grenzflächen durchgeführt werden. Eine besondere Herausforderung stellt hierbei die Auflösung der leichten Schwefel Atomsäulen in unmittelbarer Nachbarschaft zu den weitaus schwereren Blei- und Niobsäulen dar.

Die Entwicklung einer neuen Generation von Hochauflösungs-Mikroskopen, die durch Aberrations-Korrektur Messungen mit räumlichen Auflösungen unterhalb von 1 Ångstrom ermöglichen, hat einen signifikanten Fortschritt in der Genauigkeit von experimentellen Untersuchungn von Materialien auf atomarer Ebene in der Festörperphysik und Materialwissenschaft bewirkt.

Speziell die Technik des negativen sphärischen Bildkontrastes (NCSI contrast imaging) ermöglicht durch die Kombination von stark unterdrückter Bilddelokalisierung bei gleichzeitigem optimalen Kontrasttransfer die Auflösung atomarer Säulen auch bei Abständen von unter einem Ångstrom und stark unterschiedlichen Kernladungszahlen und somit atomaren Streufaktoren.

Die Technik der Austrittswellenfunktions-Rekonstruktion ermöglicht weiterhin durch numerische Verfahren das Berechnen der Phase und Amplitude der quantenmechanischen Elektronenwellenfunktion aus Fokusserien. Die Kenntnis der genauen Werte der Aberrationen der Objektivlinse in einem aberrations-korrigierten Mikroskop steigert die Genauigeit der Rekonstruktion.

Der Schwerpunkt der Arbeit lag auf dem Verfahren der oben beschrieben NCSI Technik, um die Auflösung der individuellen Schwefel, Niob- und Bleisäulen entlang der Grenzflächen der Subsysteme PbS und NbS_2 zu ermöglichen, was auch gelang.

Benutzt wurden hierfür das jüngst installierte konventionalle HRTEM Tecnai F 30 S-Twin im Kieler Nanolabor und das aberrations-korrigierte Titan T 80-300 kV am Ernst Ruska-Centrum für Mikroskopie und Spektroskopie mit Elektronen des Instituts für Fest-

körperphysik am Forschungszentrum Jülich. Dieses geschah im Rahmen einer DFG geförderter Kollaboration.

Unterstützt wurden diese so entstandenen experimentellen Bilder stets durch sogenannte *multislice* Simulationen, die Elektronenbeugung und Bildentstehung bei der Elektronenmikroskopie auf numerischer Basis berechnen und ergänzend zur besseren Bewertung von experimentellen Resultaten herangezogen wurden.

Der Fehlanpassungsschichtkristall $(PbS)_{1.14}NbS_2$ weist entlang seiner inkommensurablen Grenzflächen, die aufgrund seiner sandwich-artigen Schichtstruktur in sehr hoher Zahl vorkommen, verschiedene Modulationen der atomaren Säulenstruktur und Inhomogenitäten auf, von denen einige hier erstmalig beschrieben werden. Mit Hilfe der NCSI Technik wurden diese charakterisiert und erstmalig detailiert auf lokaler Ebene, d.h. direkt durch Auswertung von Atomsäulenpositionen quantifiziert, im Einzelnen:

- Die Störung der Stapelfolge des PbS Subsystems;
- Die Tetragonale Verzerrung des PbS;
- Langreichweitige Undulationen des Gesamtgitters.

Vergleichbare neuste Arbeiten [5] mit aberrations-korrigierter HRTEM an komplexen Systemen liefern Genauigkeiten von 3-5 pm in der Atomsäulenpositionsbestimmung. Die im Rahmen dieser Arbeit beste erreichte statistische Genauigkeit bei der Bestimmung von Atomsäulenabständen liegt mit 6 pm zwar unter der Genauigkeit von Röntgenbeugungsexperimenten [13], im Gegensatz zu diesen Verfahren ist die Aussagekraft jedoch nicht durch räumliche Mittellungen beschränkt, sondern ermöglicht direkte Einsicht in die lokale atomare Gitterstruktur des Kristalls.

Contents

1 Introduction **1**

2 Fundamentals of (aberration-corrected) HRTEM **3**
2.1 HRTEM and image intensity simulation 4
2.1.1 Basic principles 4
2.1.2 Dynamic electron scattering 5
2.1.3 Approximations for thin objects 11
2.1.4 Contrast transfer in a HRTEM 15
2.1.5 The effects of lens aberrations 16
2.1.6 Aberration-corrected HRTEM 21
2.1.7 Exit-wave reconstruction 25
2.1.8 Numerical aberration correction 30
2.2 Fundamentals of HAADF-STEM 31

3 The misfit layered compounds **35**
3.1 Transition metal dichalcogenides 35
3.2 The cubic monochalcogenide PbS 38
3.3 Misfit layered compounds 39
3.4 The crystal structure of $PbS_{1.14}NbS_2$ and its properties 41

4 Experimental **45**
4.1 Crystal growth and sample preparation 45
4.1.1 Chemical vapor transport 45
4.1.2 Preparation of ultra-thin samples for HRTEM 47
4.2 Conventional HRTEM & STEM 51
4.3 Aberration-corrected HRTEM 52
4.4 Electron diffraction 54
4.5 Comparison of conventional and aberration-corrected HRTEM imaging . . 56

5 The structure of $(PbS)_{1.14}NbS_2$: Experimental data and image simulations **59**
5.1 Lattice parameters and commensurability: Electron diffraction study . . . 59
5.1.1 Lattice projection along the [001] axis of $(PbS)_{1.14}NbS_2$ 60
5.1.2 Lattice projection along the [100] axis of $(PbS)_{1.14}NbS_2$ 62

5.1.3 Lattice projection along the [010] axis of $(PbS)_{1.14}NbS_2$ 64
5.2 Conventional Z-contrast imaging 66
5.3 Plan-view imaging 67
5.4 Conventional and aberration-corrected HRTEM imaging 70
5.5 NCSI contrast imaging 72
5.6 Focal series and reconstruction of the exit-plane wave function 72
5.7 Stacking disorder 78
5.8 Tetragonal distortion 80
5.9 Long-period undulations 84
5.10 Imaging along the $[110]_{PbS}$ axis: Individually resolving the Pb and S columns 87

6 Discussion **95**
6.1 Methodological aspects of the HRTEM experiments 95
6.2 Quantitative HRTEM results: The misfit layered compound $(PbS)_{1.14}NbS_2$ 97

7 Summary and conclusions **100**

Bibliography **102**

Chapter 1

Introduction

In the last decade a completely new generation of high-resolution transmission electron microscopes (HRTEM) with aberration-corrected electron optics has been developed which enables solid state physics and materials science studies to be performed at sub-Ångstrom resolution. Such instruments can also be equipped with energy filters and spectrometers and thus allow studies not only of the structure but also the chemical composition and electronic properties of materials at high spatial resolution.

Since the invention of the technique, experimental TEM images suffered from the effects of lens aberrations. In particular, the spherical aberration (C_s) of the objective lens delocalizes the object information and causes a strong degradation of the image. The effect of distortion of the electron wave due to the spherical aberration is used to produce phase contrast in conventional HRTEM by combining this aberration with a negative defocus of the objective lens, that acts then like a Zernike phase plate [1]. Unfortunately, high spatial frequencies corresponding to electrons that are scattered at large angles show strong delocalization and complicated contrast transfer which makes experimental images inaccessable to direct interpretation.

The invention of spherical aberration correctors that allow the value of the C_s of the optical system to be tuned like a parameter to small negative values solves these problems and opens a new dimension for the resolution limits [2] [3] [4]. In fact the enhanced contrast transfer together with the strong suppression of image delocalization under negative C_s imaging (NCSI) conditions is capable of resolving the atomic lattice structure of even complex systems, and the accuracy of spatial measurements has reached a few picometers [5]. Atomic column positions of even very light elements like oxygen situated next to heavy elements have been detected with sub-Ångstrom accuracy [6]. The high precision in atomic column position determination makes this technique perfectly applicable for the investigation of certain lattice structure features like defects and other inhomogeneities.

The transition metal dichalcogenide (TMDC) misfit layer compounds consist of alternating stacking of up to three layers of hexagonal transition metal dichalcogenides and double layers of cubic rock salt monochalcogenide with the general formula $(MX)_n(TX_2)_m$ (M = Sn, Pb, Bi or rare earths; X = S, Se, Te; T = Ta, Ti, Nb, V; n = 1.08....1.19; m

= 1,2,3) [7] [8]. Such layered systems can be understood as an intercalated TMDC with the monochalcogenide being intercalated into the van-der-Waals gaps of the TMDC compound [9]. As a result of different lattice constants in one crystallographic direction, these systems have incommensurate interfaces between each MX and TX_2 slab. This is the origin of the term misfit layered compound. These systems were prepared for the first time in 1970 but not immediately recognized as misfits [10] [11] [12].

The misfit layered compound $(PbS)_{1.14}NbS_2$ was first decribed in detail by Wiegers et al [13] who derived the crystal structure from x-ray diffraction data. Although this experimental technique is very precise in terms of accuracy in lattice parameter determination it lacks any local information about the lattice structure as the data are assembled by averaging over relatively large volumes of the samples.

In early literature [14], hints on several lattice inhomogeneities and defects in this particular system can be found that might be related to the incommensurate interfaces. In prior articles [15] [16] that were published during the work on this thesis, it was demonstrated that it is possible to detect and qualitatively describe certain lattice inhomogeneities along the incommensurate direction of this system with the experimental technique of aberration-corrected HRTEM.

The goal of this study is to investigate the methodological advantages of aberration-corrected HRTEM and NCSI contrast imaging techniques on the accuracy of atom column position determination at interfaces by quantitative comparison with x-ray diffraction data. The method of NCSI contrast imaging was applied successfully to resolve the individual atomic columns at the interfaces of the misfit layered compound $(PbS)_{1.14}NbS_2$, where weakly scattering sulphur columns are located close to the much more strongly scattering niobium and lead columns. A detailed quantitative analysis from NCSI contrast images with local lattice structure determination accuracies down to some picometers on several defects and inhomogeneities is presented.

This work was performed in close collaboration with the Ernst Ruska-Centre for Microscopy and Spectroscopy with Electrons (Institute of Solid State Research) at the Research Centre Jülich where the aberration-corrected HRTEM experiments were performed. The work was funded by the German Research Foundation (DFG) [17]. The samples were provided by the surface science group of Prof. Kipp (former group leader Prof. Skibowski) of the Departement of Experimental and Applied Physics at the Christian-Albrechts-University Kiel in the framework of a DFG Research Group [18].

Chapter 2

Fundamentals of (aberration-corrected) HRTEM

For decades object information in transmission electron microscopy was limited by the sperical aberration of the objective lens that introduces strong delocalization effects. When imaging very thin objects, spherical aberration can be used to produce phase contrast which is indeed applied in high-resolution transmission electron microscopy: The objective lens acts analogous to a Zernike plate for phase contrast imaging in light optics by compensating the distortion of the electron wave due to the spherical aberration with a negative defocus by mimicking a distortion with opposite sign [1]. Unfortunately high spatial frequencies corresponding to electrons that are scattered at large angles show strong delocalisation and rather complicated contrast transfer under these conditions. This can be partly minimized by selecting certain defocus values but never for the whole frequency range that is transferred by the microscope.

The invention of spherical aberration correctors that allow the C_s of the optical system to be tuned like a parameter to small negative values solves most of these problems and opens a new dimension for the resolution limits [2] [3]. In fact the enhanced contrast transfer together with the strong suppression of image delocalisation under negative C_s imaging (NCSI) conditions is capable of resolving the atomic lattice structure of even complex systems like the TMDC misfit compounds as will be demonstrated in chapter 5. In line with that, computational exit-wave reconstruction of the phase from focal series allows direct interpretation of the HRTEM image contrast features. The basic theory and progress from conventional HRTEM to aberration-corrected instruments including dynamic electron scattering, contrast transfer and the physical principles behind modern image simulation algorithms and the exit-wave reconstructions will be described in this chapter.

Additionally a short overview on high-angle annular dark field scanning transmission electron microscopy (HAADF-STEM) will be given as this technique was also applied on the misfit compound for the first time with the recently installed Tecnai F 30 S-Twin instrument in Kiel in order to acquire Z-contrast images.

2.1 HRTEM and image intensity simulation

The high-resolution transmission electron microscopy (HRTEM) imaging process allows to gain structure information down to the scale of atomic distances in solids ($\approx$ 2Å). In contrast to other scattering techniques like x-ray or neutron experiments that gather information averaged over a mesoscopic or macroscopic object area the HRTEM gives direct localized insight into the specimen. In the following sections the basic principles of the HRTEM, the interactions of the electron beam with the object and the contrast transfer and its effect on the image formation are explained.

2.1.1 Basic principles

As invented by Ernst Ruska and co-workers in the 1930s (Nobelprize Ernst Ruska 1986), the basic principles of transmission electron microscopes hold also true for its successor, the HRTEM: An accelerated electron beam penetrates through a thin ($\leq$ 10 nm) object and reassembles in a magnified image that can be visualized by a fluorescence screen. The optical path of the electron rays is directed by an electromagnetic lens system.

With increasing quality of the microscopes due to technical progress in e.g. the high voltage supply, the electron emitting source and the electromagnetic lenses the image resolution increased more and more but at the same time their interpretation became incremental difficult. Two main reasons can be specified that lead to these problems: First, the electron does not act as a classical particle when traversing through the sample. Instead it has quantum mechanical properties associated with it, i.e. it is an electron wave that can interfere. Therefore the intensity observed at the screen is the square of the absolute of the electron wavefunction, which means that any information about the phase is lost. The second reason is of technical origin: The elecromagnetic lenses used in modern HRTEMs cannot be compared in their quality to optical ones of light-optical systems, such as e.g. in space telescopes. The comparatively low imaging quality of the lenses limits the resolution and even worse introduces distortions to the wave function from lens aberrations. When trying to obtain the information about the object from a HRTEM image one has to solve three independent problems:

- The object information is encrypted by interference within the wavefunction.
- The exit-plane wave function is distorted due to optical aberrations.
- The phase information is lost.

In order to deal with those problems many successful approaches both on the technical (e.g. field emission guns for increased coherence [19]) as well as on the computational side (contrast interpretation with numerical image simulation software [20]) have been developed and set to standard for use in commercial instruments so far. With the help of image simulation software the electron scattering in the object and the electromagnetical imaging process is computed and compared with the experimental data. In an iterative process the input model is changed until the calculated image matches the experimental

image. The physical process is computed in the order it naturally takes place in the microscope.

In contrary, another approach is to invert this problem and try to reconstruct the exit-plane wave function from the images [21] [22]. This method will be explained in more detail later, as it was also used in this work. As an experimental alternative the electron holography [23] [24] is capable to nearly directly measure the wavefunction of an object. The latest development which is now available in new microscopes is the aberration-corrector [2] [3], that is able to push the resolution limit below 1 Å. Both such an instrument (the Titan T 80-300 kV in Jüelich) and a conventional HRTEM (the Tecnai F 30 S-Twin in Kiel) were used to study the misfit compound $(PbS)_{1.14}NbS_2$ in this work and it's principles will be discussed in the following sections.

2.1.2 Dynamic electron scattering

As decribed above two processes are relevant for image formation within a HRTEM, the interaction of the electrons with the object in the form of diffraction and the electron-optical imaging of the exit-plane wave function by the electromagnetical lens system. This section will give an overview about the first step, the scattering of the electron waves in the crystal potential.

In the initial situation an incident plane wave is modified in amplitude and phase by the potential of the atoms in the object and thus in case of a crystalline solid transfers information about the lattice when leaving the object as the exit-plane wave function. The electron interaction with the scattering potential is very strong and so the thickness of the sample plays an important role and prohibits easy predictions about the quantity of the modulations. In fact a crystal structure under the same microscope parameters lead to totally different exit-plane wave functions and thus to totally different images when only the sample thickness is altered. An ab-initio analytical derivation of the whole scattering process in real materials is impossible, but several successful approaches of numerical calculations of the diffraction exist. Two of them will now be described in more detail, the Bloch-wave and the multislice method. Both methods allow at known object parameters (like the scattering potential) to compute the associated exit-plane wave function of crystalline specimens for varying sample thicknesses. It is important to understand these algorithms in detail in order to ba able to judge mits importance when interpreting the experimental results by accompanying image intensity simulations.

It must be stated that in the following certain simplifications need to be made to deal with such a complex process as the dynamical electron scattering. First the incident beam direction is always considered to be exactly along a zone axis of the crystalline structure. Furthermore inelastic scattering will not be discussed and effects from thermal diffuse scattering will be neglected.

After the derivations of the Blochwave and multislice algorithms, a short description of some useful approximations for the case of thin objects is given for practical purposes.

The Blochwave algorithm

The Bethe-Bloch method [25] [26] starts with the relativisticly corrected Schrödinger equation for an electron wave $\Psi(\mathbf{r})$ that is accelerated by the microscope's high voltage E in the crystal potential $V(\mathbf{r})$:

$$\nabla^2\Psi(\mathbf{r}) + \frac{2me}{\hbar^2}[E^* + V(\mathbf{r})]\Psi(\mathbf{r}) = 0, \tag{2.1}$$

with e being the elementary charge, $m = m_0(1 + eE/E_0)$ the relativisticly corrected electron mass and

$$E^* = E\frac{2E_0 + eE}{2(E_0 + eE)} \tag{2.2}$$

the relativisticly corrected acceleration potential with $E_0 = m_0c^2$ the rest energy of the electron. The crystal potential is periodic and can thus be expressed as a Fourier series of the reciprocal lattice vectors h:

$$V(\mathbf{r}) = \sum_h V_h \exp(2\pi\mathrm{i}\mathbf{h}\cdot\mathbf{r}). \tag{2.3}$$

As an ansatz for the wave function the well known Blochfunction is used

$$\Psi(\mathbf{r}) = C(\mathbf{r})\exp(2\pi\mathrm{i}\mathbf{k}\cdot\mathbf{r}), \tag{2.4}$$

where $C(\mathbf{r})$ possesses the periodicity of the crystal and can as well be expanded as a Fourier series.

Inserting those terms into equation (2.1) and exploiting the fact that V_0 is generally four orders of magnitude lower than E^* one ends up with a full set of equations for each value of $\mathbf{g}$, i.e. for each scattered beam:

$$[K^2 - (\mathbf{k} + \mathbf{g})^2]C_g + \sum_{h\neq g} U_{g-h}C_h = 0 \tag{2.5}$$

with

$$K^2 = \frac{2me}{\hbar^2}(E^* + V_0) \tag{2.6}$$

as an averaged wave vector of the electrons in the crystal and

$$U_h = \frac{2me}{\hbar^2}V_h \tag{2.7}$$

as the modified potential.

Using an infinite number of beams as in the real microscope is of course not viable so one has to approximate the algorithm for practical reasons. In the case of the two-beam diffraction condition for the beams $\mathbf{k}$ and $(\mathbf{k} + \mathbf{g})$ one starts with the wave function

$$\Psi(\mathbf{r}) = C_0\exp(2\pi\mathrm{i}\mathbf{k}\cdot\mathbf{r}) + \mathrm{C_g}\exp(2\pi\mathrm{i}(\mathbf{k} + \mathbf{g})\cdot\mathbf{r}), \tag{2.8}$$

and arrives at, according to (2.5), with the equations

$$\begin{aligned}[K_2 - (\mathbf{k}+\mathbf{g})^2]C_g + U_g C_0 &= 0 \\ (K^2 - k^2)C_0 + U_{-g}C_g &= 0.\end{aligned} \tag{2.9}$$

This equation system can be solved in the case that the determinant vanishes

$$\begin{pmatrix} K^2 - k^2 & U_{-g} \\ U_g & K^2 - (\mathbf{k}+\mathbf{g})^2) \end{pmatrix} = 0. \tag{2.10}$$

As can be seen this equation is of the order of k^4. Generally using n beams leads to an equation of the order k^{2n} with 2n roots of which n are positive and n negative according to forward- and backscattering. The backscattered electrons can be neglected for high energies and therefore the general solution for the wave function is a linear combination of n Blochwaves with j different wave vectors:

$$\Psi(\mathbf{r}) = \sum_{j=1}^{n} \alpha^{(j)} \Psi^{(j)}(\mathbf{r}), \tag{2.11}$$

where $\alpha^{(j)}$ is the amplitude of the j-th Bloch wave.

The Bloch-states for the wave function become mixed, and this leads to interference effects for the waves with the different vectors $k^{(j)}$. When splitting the wave function into the individual beams one obtains

$$\Psi(\mathbf{r}) = \sum_{g} \Psi_g \exp(2\pi \mathrm{i}\mathbf{g}\cdot\mathbf{r}) \tag{2.12}$$

with the complex valued Fourier coefficients

$$\Psi_g(t) = \sum_{j} \alpha^{(j)} C_g^{(j)} \exp(2\pi \mathrm{i} k_z^{(j)} t) \tag{2.13}$$

where t denotes the sample thickness in the incident beam direction and $k_z^{(j)}$ the component of the j-th Blochwave vector along that direction. Important is to point out that now the propagation *perpendicular* to the incident beam direction is described in the exponential term of equation (2.12) alone while the propagation *parallel* to the incident beam is given by the Fourier coefficients of (2.13). The interference introduced by the sum in equation (2.13) is the origin of the thickness dependence of the Fourier coefficient's modulations.

Using the high energy approximation ($K \approx k^{(j)}$, $K \gg g$ and thus $K \approx |\mathbf{k}+\mathbf{g}|$) and splitting the Blochwave vectors into a component perpendicular and one tangential to the Laue plane, one gets two equations analog to (2.9).

Now one can go a step further and add more beams in the same manner. The set of equations keeps its form and can generally for many beams be written as

$$\frac{1}{2K}\begin{pmatrix} -k_t^2 & U_{-g} & U_{-h} & \cdots \\ U_g & -(k_t+g)^2 & U_{g-h} & \cdots \\ U_h & U_{h-g} & -(k_t+h)^2 & \cdots \\ \vdots & \vdots & \vdots & \ddots \end{pmatrix} \begin{pmatrix} C_0^{(j)} \\ C_g^{(j)} \\ C_h^{(j)} \\ \vdots \end{pmatrix} = (k_z^{(j)} - K) \begin{pmatrix} C_0^{(j)} \\ C_g^{(j)} \\ C_h^{(j)} \\ \vdots \end{pmatrix}. \tag{2.14}$$

The matrix has the size $(n \times n)$ where n is the number of beams. This equation can be solved by diagonalisation and with a few assumptions, one obtains the final expression for the coefficient vector $\mathbf{\Psi}$

$$\mathbf{\Psi}(t) = \begin{pmatrix} \Psi_0(t) \\ \Psi_g(t) \\ \Psi_h(t) \\ \vdots \end{pmatrix} = C[\exp(2\pi \mathrm{i} k_z^j t)]_D C^{-1}\mathbf{u}, \tag{2.15}$$

where C is the matrix with the eigenvectors $\mathbf{C}^{(j)}$ in it's columns, $[\cdots]_D$ a diagonal matrix and $\mathbf{u} = (1, 0, 0, \cdots, 0)$. The Fourier coefficients are thus completely described by the eigenvalues and eigenvectors of the matrix from equation (2.14) and can be computed numerically by diagonalisation algorithms. This is only possible for a limited number of beams n because the run-time is up to the order of n^3. This approach is therefore only viable for simple periodic crystals without defects or distortions in the lattice. As soon as complexities or interfaces between different crystal lattices and the like occur, the Blochwave method is no longer feasible. A numerically superior method is the multislice method that will be discussed now.

The multislice method

The interaction of the incident electron wave and the periodic lattice potential $V(\mathbf{r})$ is described as a sequence of phase shifts on consecutive diffraction planes within the multislice approach [27] [28]. Figure 2.1 shows such a sequence of "slices"schematically: A slice contains an infinitely thin diffraction plane perpendicular to the incident beam direction that induces a phase shift to the wave funtion $\Psi(\mathbf{r})$. Between the diffraction planes vacuum of the thickness Δz is assumed. Such a slice reflects the distribution of the atom potential originating from the atoms within the slice that modifies the passing electron waves. The potential is projected onto a plane and the thickness is mimicked by the vacuum. The phase shift modulation is mathematically described by the phase-grating function and the dispersion between the diffraction planes via the propagator function.

(a) The phase-grating function

The incident electron beam is described by

$$\Psi(\mathbf{r}) = \Psi_0 \exp(2\pi \mathrm{i} \mathbf{k_0} \cdot \mathbf{r}), \tag{2.16}$$

with the relativistically corrected wavevector $\mathbf{k_o}$ in the vacuum

$$|\mathbf{k_0}| = \left(\frac{2meE^*}{\hbar^2}\right)^{1/2}, \tag{2.17}$$

and

$$|\mathbf{k_i}(\mathbf{r})| = \left(\frac{2me(E^* + V(\mathbf{r}))}{\hbar^2}\right)^{\frac{1}{2}} \overset{V \ll E^*}{\approx} |\mathbf{k_0}| + \frac{meV(\mathbf{r})}{\hbar^2 |\mathbf{k_0}|}, \tag{2.18}$$

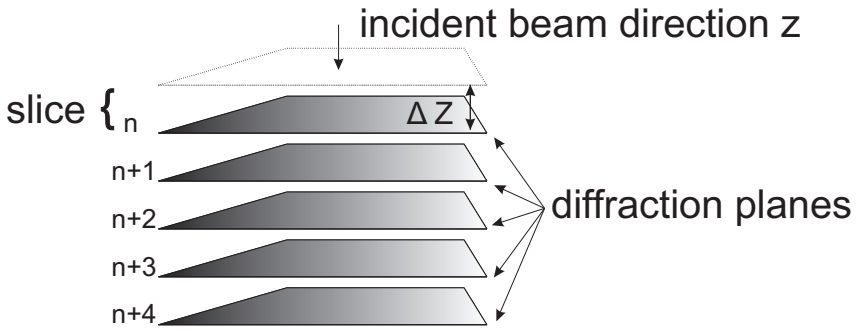

Figure 2.1: *Illustration of the basic principle of the multislice method: 5 slices are schematicly drawn that consist each of an infinitely thin diffraction plane and vacuum of the thickness Δz. The atomic potential is projected onto each diffraction plane.*

in the crystal, where E^* is the accelerating potential and $V(\mathbf{r})$ the crystal potential. After being transmitted by a slab of the crystal with the thickness dz the wave function has experienced a phase shift compared to a wave in the vacuum which can mathematically be written as

$$\Psi(x, y, z + dz) = \Psi_0 \exp(2\pi \mathrm{i} \mathbf{k_0} \cdot \mathbf{r}) \exp\left[\frac{2\pi \mathrm{i} m e V(\mathbf{r}) dz}{\hbar^2 |\mathbf{k_0}|}\right], \tag{2.19}$$

and after integration along Δz

$$\Psi(x, y, z + \Delta z) = \Psi(x, y, z) \underbrace{\exp\left[\frac{2\pi \mathrm{i} m e}{\hbar^2 |\mathbf{k_0}|} \int_0^{\Delta z} V(x, y, z) dz\right]}_{Q}, \tag{2.20}$$

with the phase-grating function Q. The phase shift induced by the scattering at the crystal potential is thus described by a multiplication of the wave function with the phase-grating function. The projected crystal potential $V_p(x, y)$ that is constant along the slice in z direction can be calculated and Q becomes

$$Q(x, y) = \exp\left[\frac{2\pi \mathrm{i} m e}{\hbar^2 |\mathbf{k_0}|} V_p(x, y) \Delta z\right], \tag{2.21}$$

with

$$V_p(x, y) = \frac{1}{\Delta z} \int_0^{\Delta z} V(x, y, z) dz. \tag{2.22}$$

The result shows that the phase-grating function has the form of a phasefactor that is a function only of the transmitted object thickness Δz and the projected crystal potential.

(b) The propagator function

The wave dispersion between two slices n and $n + 1$ can be understood in analogy to classical wave mechanics: Every point in the diffraction plane n generates a coherent

spherical wave. All waves sum up in the $n+1$ plane, according to the Huygens-Fresnel principle. Due to the fact that the added waves differ in their optical path lengths their phases are then different too.

Consider a spherical wave $\Psi_n(X,Y)\exp(2\pi \mathrm{i} kr)$ that started from the point (X, Y) in the n-th diffration plane. To calculate the resulting wave at the point (x,y) of the $n+1$ plane one has to integrate over all possible points of origin of the plane n:

$$\Psi_{n+1}(x,y) \sim \int_{-\infty}^{+\infty}\int_{-\infty}^{+\infty} \Psi_n(X,Y)\exp(2\pi \mathrm{i} kr)dXdY. \tag{2.23}$$

Using the parabolic approximation for the spherical wave fronts and ignoring the phase-factor of $\exp(2\pi \mathrm{i} k\Delta z)$ that is the same for all beams emitted from any point in the n-th plane, this can be rewritten to

$$\Psi_{n+1}(x,y) = \frac{\mathrm{i}k}{\Delta z}\int_{-\infty}^{+\infty}\int_{-\infty}^{+\infty} \Psi_n(X,Y)\exp\left(\frac{\pi \mathrm{i} k}{\Delta z}[(x-X)^2+(y-Y)^2]\right)dXdY. \tag{2.24}$$

The normalisation constant accounts for the intensity conservation. Mathematically this expression is a convolution of the wave function in the n-th plane and the so-called *Fresnel propagator* function $P(x,y)$ that describes the spatial dispersion of the wave:

$$\Psi_{n+1}(x,y) = \Psi_n(x,y) * P(x,y), \tag{2.25}$$

with

$$P(x,y) = \frac{\mathrm{i}}{\lambda\Delta z}\left(\frac{\pi \mathrm{i}(x^2+y^2)}{\lambda\Delta z}\right), \tag{2.26}$$

using $k = 1/\lambda$.

Equation (2.26) can be transformed into the Fourier space for practical reasons:

$$\mathcal{F}(P(\mathbf{r})) = P(\mathbf{g}) = \exp(\pi \mathrm{i}\lambda\Delta z|\mathbf{g}|^2). \tag{2.27}$$

(c) The multislice algorithm

In real space the exit wave function of the $(n+1)$-th plane is given by the recursion formula

$$\Psi_{n+1}(\mathbf{r}) = [\Psi_n(\mathbf{r}) * P(\mathbf{r})]\cdot Q_{n+1}(\mathbf{r}). \tag{2.28}$$

Presuming an object thickness $t = m\cdot\Delta z$ with $m \in \mathbb{N}$, one gets the exit-plane wave function through recursive application. Run-time considerations lead to mixed algorithms where the real- and Fourier representation of the formula are used alternatingly to avoid the intricate convolution in real space that becomes a simple multiplication in Fourier space:

$$\mathcal{F}[\Psi_n(\mathbf{r}) * P(\mathbf{r})] = \mathcal{F}[\Psi_n(\mathbf{r})]\mathcal{F}[P(\mathbf{r})] = \Psi_n(\mathbf{g})P(\mathbf{g}). \tag{2.29}$$

Therefore the algorithm can also be written as

$$\Psi_{n+1}(\mathbf{g}) = \mathcal{F}(\mathcal{F}^{-1}[\Psi_n(\mathbf{g})P(\mathbf{g})]Q_{n+1}(\mathbf{r})). \tag{2.30}$$

Although the physical process of the dynamic electron scattering is not described as figurative in the multislice method as in the Bloch wave algorithm, the run-time advantages are huge: Practical tests show that in order to compute a wave function in a single point in the plane $(n+1)$ it is not necessary to sum up the wave function over all points in the nth plane (with run-times $\sim N^2$ for N points) but only those in the neighbourhood of the position vector of the point. These N points are referred to as "beams"and the bigger the unit cell is expanded in the xy plane, the more beams have to be taken into account.

During the recursion the Fourier transformations define the run-time of the algorithm and thus for N beams the Fast Fourier Transform (FFT) method provides run-times $\sim N \log_2 N$ which, compared to the N^3-dependence of the Bloch wave approach (see above), lead to much shorter computation times.

Concluding, for real crystals with defects and other lattice distortions where a large supercell is needed to describe the systems probabilities realistically, the multislice algorithm is superior in terms of run-time economy compared to the physically more intuitive Blochwave method.

2.1.3 Approximations for thin objects

Simplifications in the form of approximations can be useful tools and help to better understand this complex physical process of dynamic electron scattering in a qualitative way. The numerical approaches described above deliver quantitatively correct data, but for special constraints like for very thin objects it might be helpful to use certain approximations.

The phase-grating approximation

The phase-grating approximation [29] assumes that in the multislice algorithm the propagation of the electron waves between the slices can be neglected. Therefore only a sequence of phase shifts described by the phase-grating function has to be calculated. This is achieved by putting the Fresnel propagator to

$$P(\mathbf{r}) = \delta(\mathbf{r}) \tag{2.31}$$

in real space and

$$P(\mathbf{g}) = 1 \tag{2.32}$$

in Fourierspace in equations (2.26) and (2.27), respectively, because a convolution with a delta function in real space is a neutral operation. The same is of course true for the multiplication with 1 in Fourierspace.

Assuming furthermore that the crystal lattice is homogeneous parallel to the incident beam direction even the slices can be reduced to a single phase shift when the projected potential is taken from the whole thickness of the object. Then the wave function for an object with thickness t becomes

$$\Psi(\mathbf{r}) = \exp[\mathrm{i}\Phi(\mathbf{r})] = \exp[\mathrm{i}\sigma V_p(\mathbf{r})t], \tag{2.33}$$

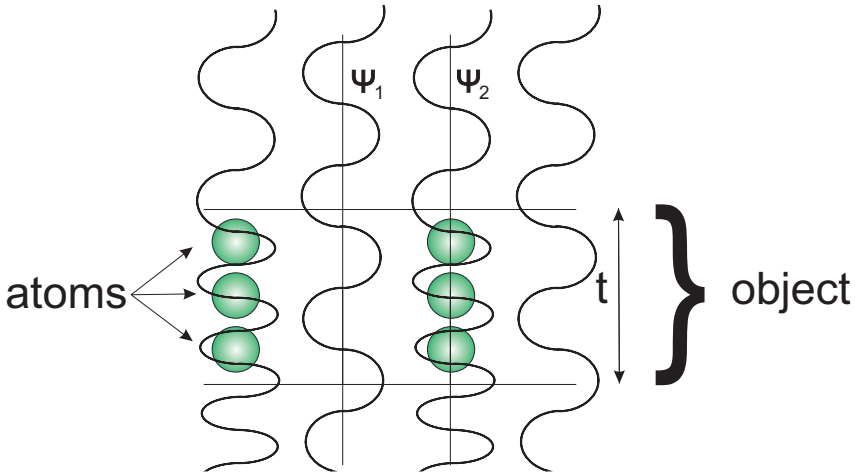

Figure 2.2: *Illustration of the phase-grating approximation after [29]: The phase of the electron wave that passes the object on a path of high projected potential (sites of the atoms) with thickness t becomes contracted in wave length and thus its phase is shifted compared to the unscattered wave where the potential is lower.*

with the interaction constant σ:

$$\sigma = \frac{2\pi me}{\hbar^2 |\mathbf{k}_0|}.$$

The consequences are illustrated in figure 2.2: The scattering potentials $V(\mathbf{r})$ are positive and thus the phase $\Phi(\mathbf{r})$ of the scattered electron wave hurries ahead compared to the phase of the unscattered wave. One also recognizes that this approximation neglects any amplitude modulation in real space so that $I(\mathbf{r}) = |\Psi(\mathbf{r})|^2 = 1$ for any given $\mathbf{r}$, which can obviously not be true and is an effect of the missing lateral wave propagation: Only scattering events along the optical path of Ψ_2 affect its amplitude at the exit-plane, interference with Ψ_1 does not occur. This is a major disadvantage of the phase-grating approximation.

The weak-phase-object approximation

The weak-phase-object approximation neglects the wave propagation in the same way as the phase-grating approximation and assumes additionally that the phase shift is very small, i.e. $|\Phi(\mathbf{r})| \ll 1$ which is true when the interaction of the electron wave and the scattering potential is very weak. This situation is, to a reasonable degree, given for objects not thicker than ≈ 3 nm. Then the exponential term can be derived as $\exp(\mathrm{i}\Phi(\mathbf{r})) \approx 1 + \mathrm{i}\Phi(\mathbf{r})$ and the wave function at object thickness t becomes

$$\Psi(\mathbf{r}) = 1 + \mathrm{i}\Phi(\mathbf{r}) = 1 + \mathrm{i}\sigma V_p(\mathbf{r})t. \tag{2.34}$$

This implies that the incident plane wave at the object surface is real ($\Psi_0 = 1$) and thus only the imaginary part is proportional to the potential V_p and the thickness t. The

problem with equation (2.34) is that the intensity of the incident wave equals 1 at any given $\mathbf{r}$ ($I_0 = \Psi_0\Psi_0^* = 1$) but obviously $I(\mathbf{r}) = \Psi(\mathbf{r})\Psi^*(\mathbf{r}) > 1$ for any $\mathbf{r}$ in the crystal. That means the electron intensity is increased in the crystal and the conservation of particles is violated. This effect becomes more dramatic with increasing thickness.

The equation (2.34) shows also, that for thin objects the imaginary part of the wave function corresponds directly to the projected potential. Because the potential is located at the positions of the atoms, the imaginary part projects the object structure, which is the main reason why the weak-phase-object approximation is so popular. For thin objects this relation is also true for the phase $\Phi(\mathbf{r})$ of the exit-plane wave function and the projected potential, which plays an important role for exit-plane wave reconstruction algorithms that will be discussed later.

The kinematic approximation

In the phase-grating and the weak-phase-object approximations the wave propagation in the object is neglected. In the kinematic approximation the diffraction within a slice is approximated by a weak-phase object and multiple scattering events are excluded. This exclusion means that the diffracted part of the wave function propagates to the exit plane without being further scattered at other diffraction planes. Basically the kinematic approximation uses the full wave propagation formalism while the description of the scattering events is simplified. Therefore weak interactions between the incident wave and the scattering potentials (e.g. in the case of x-ray and neutron scattering) are well described within the kinematic approximation while for many-beam interactions in transmission electron microscopy it is not fully satisfactorily applicable.

The Fourier transform of the wave function in the weak-phase-object approximation (equation (2.34)) for a slice of thickness Δz is

$$\Psi_s(\mathbf{g}) \approx \delta(\mathbf{g}) + \mathrm{i}\sigma V_p(\mathbf{g})\Delta z, \tag{2.35}$$

where Ψ_s describes the wave function after a *single* (in contrary to (2.34)) scattering event. At the exit-plane these waves from all the diffraction planes sum up to the Fourier transform of the wave function $\Psi(g_x, g_y)$ while the propagation is described by the Fresnelpropagator in (2.27). Then the object is assumed to be infinitely large in the (x, y) plane perpendicular to the incident beam direction and the object thickness t to be much higher than the slice thickness Δz so that the sum has to be calculated only for the z component and can be replaced by an integration from 0 to t:

$$\Psi(g_x, g_y) \approx \mathrm{i}\sigma V(g_x, g_y) \int_0^t \exp[\pi \mathrm{i}\lambda|g|^2 z]\mathrm{d}z \tag{2.36}$$

describes the scattered part ($\mathbf{g} \neq 0$) of the wave function at the exit plane. Note that $V_p(\mathbf{g}) = V(g_x, g_y, 0) = V(g_x, g_y)$. The integral reads then

$$\Psi(g_x, g_y) \approx \mathrm{i}\sigma V(g_x, g_y) t \frac{\sin(\pi s_z t)}{\pi s_z t} \exp[\pi \mathrm{i} s_z t], \tag{2.37}$$

with the so-called *excitation error*:

$$s_z = \frac{1}{2}\lambda(g_x^2 + g_y^2). \tag{2.38}$$

Comparison of (2.37) with the weak-phase-object approximation (eq. (2.35)) shows two additional factors in the part of the wave function describing the scattering: First, the exponential term is only a result of the relative frame of reference where the exit-plane was chosen as the origin of the coordinate system. By taking the object center as that and then integrating from $-t/2$ to $+t/2$ lets the exponential expression vanish. Secondly and more important is the $\sin x/x$ term with the excitation error s_z in its argument. The intensity of the scattered beam is

$$I(g_x, g_y) = |\Psi(g_x, g_y)|^2 \approx \sigma^2 V^2(g_x, g_y) t^2 \frac{\sin^2(\pi s_z t)}{(\pi s_z t)^2}, \tag{2.39}$$

which is consistent with the expression for the general diffraction intensity (see e.g. [29]) for three dimensional objects and for an arbitrary incident beam direction. In that case the unit cell is given by (a_x, a_y, a_z), the object is spatially limited by $N_x \times N_y \times N_z$ unit cells and the intensity is calculated to

$$I(\mathbf{g}) \approx \lambda^2 |F(\mathbf{g})|^2 |G(\mathbf{g})|^2 = \lambda^2 |F(\mathbf{g})|^2 \frac{\sin^2(\pi s_x N_x a_x)}{(\pi s_x a_x)^2} \frac{\sin^2(\pi s_y N_y a_y)}{(\pi s_y a_y)^2} \frac{\sin^2(\pi s_z N_z a_z)}{(\pi s_z a_z)^2}. \tag{2.40}$$

Considering the geometry and the relation between the *structure factor* $F(\mathbf{g})$ and the potential coefficient $V(\mathbf{g})$:

$$F(\mathbf{g}) = \frac{2\pi m_0 e V_E}{\hbar^2} V(\mathbf{g}), \tag{2.41}$$

equation (2.41) is equivalent to eq. (2.37), that was derived in a much simpler way under certain restrictions. The structure factor is a sum over all atoms of a unit cell with the *atomic scattering amplitudes* $f(\mathbf{g})$, that denotes the scattering strength of an atom for an electron wave in the direction $\mathbf{g}$:

$$F(\mathbf{g}) = \sum_i f_i(\mathbf{g}) \exp[-2\pi i \mathbf{g} \cdot \mathbf{r}_i]. \tag{2.42}$$

The value of $f(\mathbf{g})$ depends on the element and can be numerically calculated [30] [31].

The *lattice amplitude* $G(\mathbf{g})$ in equation (2.40) correlates the crystal dimensions with the diffraction intensity. The well-known Ewald sphere construction shows for an infinitely large crystal that only for the exact fulfillment of Bragg's law $\mathbf{k} - \mathbf{k}_0 = \mathbf{g}$, i.e. the Ewald sphere surface crosses a reciprocal lattice point, any diffraction contrast exists for a certain $\mathbf{g}$. The excitation error $\mathbf{s}$ describes the deviation from the exact Bragg law $\mathbf{k} - \mathbf{k}_0 = \mathbf{g} + \mathbf{s}$ where still contrast occurs. The broadening of the reciprocal lattice points is decribed by $G(\mathbf{g})$ and is inversly proportional to the object thickness t. The streaking of the lattice points to rods by the convolution of the point $\mathbf{g}$ and the amplitude $G(\mathbf{g})$ is the origin of the diffraction intensity. In fact without this streaking mechanism for high symmetry

incident beam directions no intensity contrast would be produced at all because no point $\mathbf{g}$ is exactly crossed by the Ewald sphere in this case!

The smaller the object is extended into a real space direction, the more is the reciprocal lattice point streaked into the appropriate direction in the Fourier space. That is also a direct representation of Heisenbergs position-momentum uncertainty principle for the electron. The excitation error can be found in the equations for the Fresnel propagator of the multislice algorithm (2.27) as well as in the Blochwave eigenvalue equation (2.14) (in the diagonal elements of the matrix).

2.1.4 Contrast transfer in a HRTEM

While in the previous sections the interaction of the electron wave and the object was described, this chapter deals with the aspects of the imaging process of the exit-plane wave function which is also of relevance for the image simulations.

One of the main problems that was already mentioned in section 2.1.1 is the loss of the phase information due to $I(\mathbf{r}) = \Psi(\mathbf{r})\Psi^*(\mathbf{r}) = A^2(\mathbf{r})$. In the case of a thin object in the phase-grating approximation the whole object information is enclosed in the phase and the amplitude is just a constant background $A(\mathbf{r}) = 1$. Therefore no contrast would occur at all in the image. The wave function is complex and is projected onto a real function during the imaging process. In Fourierspace the intensity for a periodic object with discrete wavevectors (often referred to as *spatial frequencies*) can be expressed as

$$I(\mathbf{g}) = \sum_{\mathbf{k}} \Psi(\mathbf{g}+\mathbf{k})\Psi^*(\mathbf{k}). \tag{2.43}$$

The summand represents the interference of two beams, i.e. two plane waves, that add up to the image intensity and only those contribute whose difference is exactly a wave vector $\mathbf{g}$. But in general it is possible to find many combinations of beams whose differences yield a certain $\mathbf{g}$, so an image can contain frequencies that are not part of the object at all, and thus it is important to differentiate between *image* frequencies and *object* frequencies.

Equation (2.43) depicts furthermore that a wave function that consists of N beams produces an image frequency spectrum of $2N-1$ beams with N^2 terms, because all pairs of beams whose difference is the same contribute to the same image frequency. This can lead to a major error when the resolution of a microscope is determined from an image, because its spectrum contains frequencies up to two times larger than those of the object spectrum. These image frequencies are called artefacts.

And worse, even image frequencies that are equal to those of the object contain interference terms that are not exclusively composed of object interferences where one wave vector equals zero (those are called *linear* terms). The interference terms where both frequencies are not equal zero are refered to as *non-linear* terms. Hence, all artefact frequencies are purely non-linear and an object spectrum that contains N frequencies hosts N^2 interference terms of which only N are linear.

Furthermore linear terms always show up in pairs (e.g. $(\mathbf{g}, 0)$ and $(0, -\mathbf{g})$) in the image spectrum and thus the information from two different object frequencies $\mathbf{g}, -\mathbf{g}$ is

superimposed in the image frequency $\mathbf{g}$. The reason is the so-called *Friedel symmetry* law which states that for the image intensity $I(-\mathbf{g}) = I^*(\mathbf{g})$ holds true for every Fourier transform of a real parameter $I(\mathbf{r})$. The origin of the appearance of the Friedel symmetry here is obviously the real-valued image intensity.

The assumptions made so far have not taken into account any possible influence of the lens system of a real microscope on the image intensity. The imaging process of a wave function by the formation of the square modulus itself induces artefacts by interference. If the object of interest can be approximated as a weak-phase-object (which is normally not the case for systems with an application in the materials science), the imaging can be restricted to the linear contrast transfer. In that case equation (2.43) reduces to

$$I_L(\mathbf{g}) = \Psi^*(0)\Psi(\mathbf{g}) + \Psi(0)\Psi^*(-\mathbf{g}). \tag{2.44}$$

Here $\Psi(0)$ and $\Psi^*(0)$ are the Fourier transforms of the unscattered zero beam and its conjugate-complex, i.e. unmodulated plane waves. The superposition of both interference terms leads to the loss of the phase in the real image intensity. In the electron holography a separation of these terms is achieved by interference of the exit-plane wave function with an unscattered reference beam to image the wave function directly.

Considering a weak-phase object with $\Psi(\mathbf{g}) = \mathrm{i}\sigma V(\mathbf{g})t$, $(\Psi(0) = 1)$ the linear contrast can be calculated using equation (2.44). A real microscope uses electromagnetic lenses for the image contrast transfer that modulate the wave function in the form of a phase angle $\chi(\mathbf{g})$, so that the linear intensity that is transferred can be expressed as

$$I_L(\mathbf{g}) = \mathrm{i}\sigma V(\mathbf{g})t\exp(\mathrm{i}\chi(\mathbf{g})) - \mathrm{i}\sigma V^*(-\mathbf{g})t\exp(-\mathrm{i}\chi(\mathbf{g})) = -2\sigma V(\mathbf{g})t\sin\chi(\mathbf{g}), \tag{2.45}$$

where $\sin(\chi(\mathbf{g}))$ is called the coherent *contrast transfer function* (CTF). Therefore a weak-phase object in a microscope without any phase modulation ($\chi(\mathbf{g}) = 0 \Rightarrow \sin(\chi) = 0$) shows no image contrast at all. The contrast becomes a maximum if $\chi(\mathbf{g}) = n \cdot (\pm\pi/2)$, with $n = 1, 3, 5, ...$ [1]. In analogy to light optics, where a $\lambda/4$ phase plate induces a phase shift of $\pi/2$ [32] [33], optimal phase contrast can be produced by an analogous mechanism in the electron microscopy that is described in the next section.

2.1.5 The effects of lens aberrations

Electron microscopes suffer from several aberrations of the electromagnetic lenses due to technical difficulties in the construction of the lenses. One severe aberration is the spherical aberration described by the spherical aberration constant (C_s) that is illustrated in figure 2.3: Beams under different incident angles θ become more (for higher θ) or less (for smaller θ) diffracted so that they don't coincide with each other in the focal point. as a result, the wave fronts are bended more at the outer parts and diverge from the spherical form that is given by the Gaussian lens equation:

$$\frac{1}{f} = \frac{1}{a} + \frac{1}{b}, \tag{2.46}$$

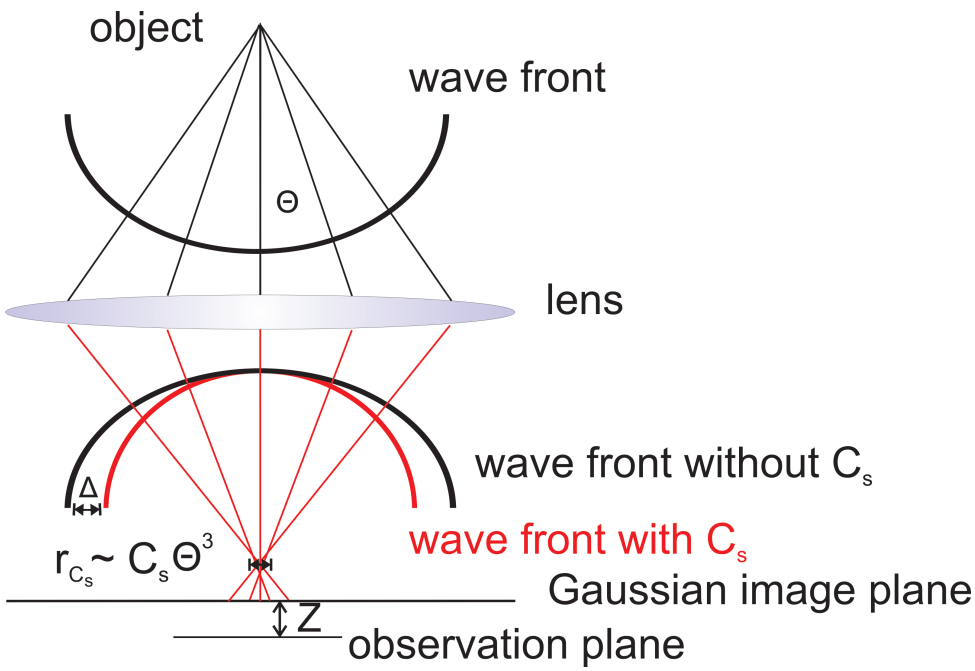

Figure 2.3: *Spherical aberration: Beams with higher incident angles θ are diffracted more strongly. In the Gaussian plane the waves form a disc instead of a point whose radius is proportional to the spherical aberration constant C_s. The distance between Gaussian image plane and the plane of observation is the defocus Z.*

with f the focal length of the lens, a the object width and b the image width.

Therefore beams with a higher incident angle θ converge in a point above the Gaussian image plane. The result in the Gaussian image plane is a divergent beam that - when all beams are considered - forms a disc. The radius of this error disc in the image plane is proportional to the spherical aberration constant C_s:

$$r_{C_s} = MC_s\theta^3, \tag{2.47}$$

where M is the magnification. By the bending of the wave fronts a difference in the optical path length Δ and thus a phase shift is introduced. Tuning the spherical aberration (which is a property of the electromagnetic lenses and therefore a constant in conventional microscopes) like a parameter by using a corrector [2] [3] allows to adjust the phase shift according to the $\pi/2$ criterion .

An analogous can be achieved by changing the focal length $f + \Delta f$ of the lens or the object width $a + \Delta a$ to over- and underfocus: The distance between the gaussian image plane and the plane where the image is observed is given by the *defocus* $Z = \Delta a - \Delta f$, where $Z > 0$ is defined by the signs as overfocus and $Z < 0$ as underfocus. The radius of the image plane disc by defocusing is

$$r_Z = MZ\theta. \tag{2.48}$$

The angle difference ϵ from the Gaussian path of rays introduced by defocus and spherical aberration for a beam with distance R to the optical axis becomes

$$\epsilon = \frac{r_{C_s} + r_Z}{b} = C_s \frac{R^3}{f^4} + Z\frac{R}{f^2}, \tag{2.49}$$

with $M \simeq b/f$ and $\theta \simeq R/f$. The electron optical path difference compared with an ideal beam is $\mathrm{d}s = \epsilon \mathrm{d}R$ and integration over the lens radius in equation 4.49 yields the phase shift that is called *aberration function* $\chi(\theta)$:

$$\chi(\theta) = \frac{2\pi}{\lambda}\Delta s = \frac{2\pi}{\lambda}\int_0^R \epsilon \mathrm{d}R = \frac{2\pi}{\lambda}\left(\frac{1}{4}C_s\frac{R^4}{f^4} + \frac{1}{2}Z\frac{R^2}{f^2}\right)$$

$$\overset{\theta\simeq R/f}{=} \frac{2\pi}{\lambda}\left(\frac{1}{4}C_s\theta^4 + \frac{1}{2}Z\theta^2\right). \tag{2.50}$$

From the relationship between the diffraction angles and the spatial frequencies $g = \theta/\lambda$ one gets

$$\chi(g) = 2\pi\left(\frac{1}{4}C_s\lambda^3 g^4 + \frac{1}{2}\lambda Z g^2\right). \tag{2.51}$$

To get an impression for which range of parameters the aberration function delivers phase shifts according to the $\pi/2$ criterion it is useful to introduce the unit-less generalized parameters θ^*, g^*, Z^* with

$$\theta^* = \theta(C_s/\lambda)^{1/4} = g^* = g(C_s\lambda^3)^{1/4}, Z^* = Z(C_s\lambda)^{-1/2}, \tag{2.52}$$

so that the aberration function is now independent of the microscope-related constants C_s and wavelength λ and becomes:

$$\chi(\theta^*) = 2\pi\left(\frac{\theta^{*4}}{4} + \frac{\theta^{*2}}{2}Z^*\right). \tag{2.53}$$

This function is plotted in figure 2.4. The goal is to find a value for the defocus Z, where the contrast $\sin(\chi(g))$ becomes a maximum, which is achieved when $\chi(\mathbf{g}) = n \cdot (\pm\pi/2)$, with $n = 1, 3, 5, ...$ At the same time the contrast should change as little as possible with the spatial frequency. This is usually the case where the aberration function has a local extremum, which only exists for negative values of the defocus. Figure 2.4 shows some selected $\chi(\theta^*)$ plots for values of Z^* that produce minima which are odd multiples of $-\pi/2$. This is true for $Z^* = -\sqrt{2n-1}$ with $n \geq 1$. Around the minima, a range of frequencies is transferred with a similar phase shift, with the optimum achieved for $Z^* = -1$. Such a frequency range is called *passband*.

The phase shifts of several hundred degrees are by all means typical for high resolution images, which indicates that the exit-plane wave function is modified in a strong way.

The passbands are even better visible when one takes a look at the CTF of a microscope's objective lens: Figure 2.5 shows the calculated CTF for a conventional HRTEM

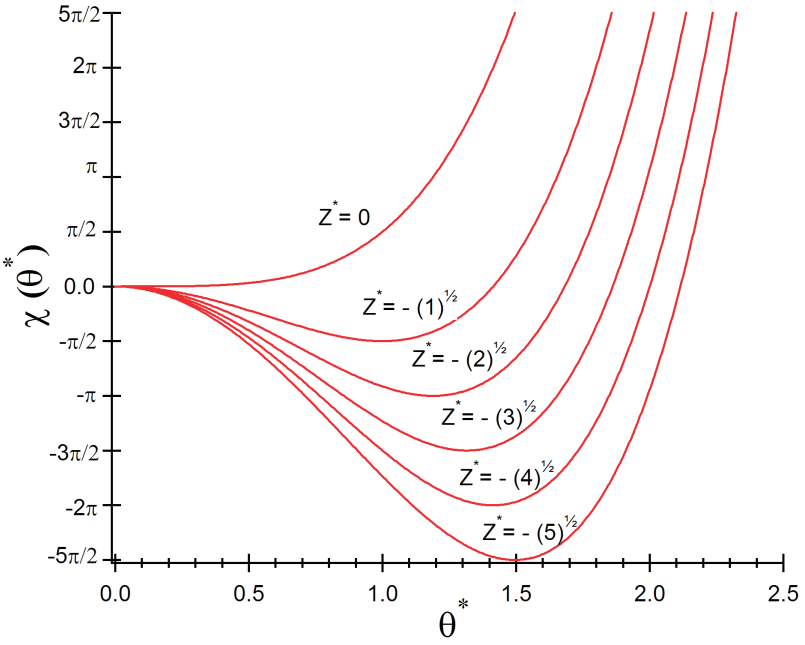

Figure 2.4: *Aberration function $\chi(\theta^*)$ as function of the generalized diffraction angle θ^* for different values of the defocus Z^*. Optimal phase contrast is achieved over a large range of spatial frequencies ($\pi/2$ criterion) for $Z^* = -\sqrt{2n-1}$ with $n \geq 1$.*

(red curve, Tecnai F 30 S-Twin) under conditions of the so-called *Scherzer defocus*, that corresponds to $Z^* = -1$ with a phase shift of approximately $-2\pi/3$.

In that case the spherical aberration phase shift and that of the defocus compensate each other over a large range of frequencies. Inserting the values into equation 2.51 the Scherzer defocus [1] becomes

$$Z_s = -(\frac{4}{3}C_s\lambda)^{1/2}. \tag{2.54}$$

The first root of the CTF defines the *point resolution* of the microscope. For Scherzer defocus it is given by g_s with

$$g_s = (\frac{3}{16}C_s\lambda^3)^{-1/4}. \tag{2.55}$$

The passband for the low frequency regime is explicitly visible in figure 2.5, for higher spatial frequencies strong oscillations occur, that forbid a direct interpretation of the image intensity. The smallest real space distance that is resolved can be calculated to:

$$d_s = \frac{1}{g_s} = \left(\frac{3}{16}C_s\lambda^3\right)^{1/4} = 0.66(C_s\lambda^3)^{1/4}, \tag{2.56}$$

which is the usual definition of the point resolution of a microscope. Note, that for this definition any information from higher spatial frequencies beyond the first root of the CTF

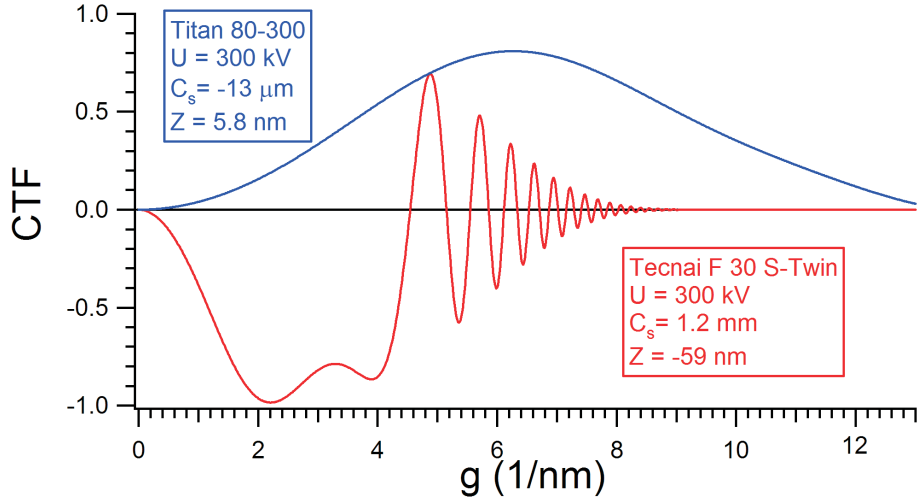

Figure 2.5: *Contrast transfer function for the conventional high-resolution microscope Tecnai F 30 (semiconvergence angle $\alpha = 0.3$ mrad, defocus spread $\delta Z = 5.3$ nm) at Scherzer defocus and for an aberration-corrected Titan 80-300 instrument (semiconvergence angle $\alpha = 0.2$ mrad, defocus spread $\delta Z = 2.9$ nm) with negative C_s.*

is cut off arbitrarily. A possibility to indicate the smallest object detail by the imaging system is given by the *information limit* d_f. The wave amplitude at the information limit is assumed to be damped to a value of $1/e^2 \equiv 13\%$:

$$d_{inf} = \left(\frac{\pi\lambda\Delta}{2\sqrt{2}}\right)^{1/2}, \tag{2.57}$$

where Δ is the *defocus spread* that is an important quantity for the stability of modern field emission gun microscopes and is given by

$$\Delta = C_C\sqrt{\left(\frac{\Delta E}{E_0}\right)^2 + \left(\frac{\Delta V}{V_0}\right)^2 + \left(\frac{2\Delta I}{I_0}\right)^2}, \tag{2.58}$$

with the constant of chromatic aberration C_C, mean energy E_0, potential V_0 and lens current I_0 and their variations in time $\Delta E, \Delta V, \Delta I$. The defocus spread is driven by the Maxwell distribution of the energy of the electron source and the instabilities of the accelerating voltage and the lens current and causes a decoherence in time. LaB6 emitters suffer from spatial damping envelopes of the aberration function that suppress higher spatial frequencies due to spatial incoherence. In contrary to that, modern FEG microscopes like the Tecnai F 30 in the Nanolab Kiel allow to work with nearly parallel illumination and thus very low convergence angles θ. The resolution is then limited mainly by the coherence in time given by the defocus spread.

The oscillations in figure 2.5 are due to the spherical aberration of the objective lens that is included in equation (2.51) with the 4th power of g. The strong gradient of the

aberration function has a big influence on the image, because it is similar to the radius of the error disc in equations (2.47) and (2.48). In the presence of defocus and spherical aberration, the lateral displacements of all beams from the Gaussian optical path have to be taken into account (and not only the ones with the highest θ), because both might compensate each other to a certain degree. With $\theta = \lambda|\mathbf{g}|$ the lateral displacement in the image plane induced by defocus is $\Delta\mathbf{r}_Z(\mathbf{g}) = Z\lambda\mathbf{g}$ and that induced by spherical aberration $\Delta\mathbf{r}_{C_s}(\mathbf{g}) = C_s\lambda^3\mathbf{g}^3$. For $Z > 0$ the sign of the displacement is the same for both terms while for underfocussing ($Z < 0$) a compensation is achieved. The total displacement is given by:

$$\Delta\mathbf{r}(\mathbf{g}, Z) = \Delta\mathbf{r}_{C_s}(\mathbf{g}) + \Delta\mathbf{r}_Z(\mathbf{g}) = (C_s\lambda^3\mathbf{g}^2 + Z\lambda)\mathbf{g} = \frac{1}{2\pi}\nabla\chi(\mathbf{g}, Z). \tag{2.59}$$

Here $\nabla\chi$ is just the partial derivation of χ:

$$\nabla\chi = \frac{1}{2\pi}\frac{\partial\chi(\mathbf{g}, Z)}{\partial\mathbf{g}} = (C_s\lambda^3 g^2 + Z)\mathbf{g}. \tag{2.60}$$

The maximum displacement $|\Delta\mathbf{r}|_{max}$ describes the radius of the disc for a frequency band $[0, \mathbf{g}_{max}]$ where g_{max} is given e.g. by the information limit. The radius is referred to as *delocalisation radius* R:

$$R(Z) = |\Delta\mathbf{r}(\mathbf{g}, Z)|_{max} = \frac{1}{2\pi}|\nabla\chi(\mathbf{g}, Z)|_{max}. \tag{2.61}$$

The delocalisation can be minimized by choosing a defocus value Z in such a way, that the radius is minimized for a given $\mathbf{g}_{max}$. This Z_{min} is called *Lichte defocus* according to [34] and becomes

$$Z_{min} = -\frac{3}{4}C_s\lambda^2 g_{max}^2 \tag{2.62}$$

with

$$R_{min} = \frac{1}{4}C_s\lambda^3 g_{max}^3. \tag{2.63}$$

While the values for optimal Scherzer defocus are about some 10 nm underfocus, a minimum in delocalisation and thus the Lichte defocus is approximately 100 nm or below underfocus, depending on the desired resolution. The passband is shifted to higher spatial frequencies for Lichte defocus conditions compared to Scherzer conditions. Oscillations occur both at very low and very high frequencies. For conventional HRTEM instruments like the Tecnai F 30, R_{min} of 1 - 2 nm is achieved, which is still one order of magnitude larger than the smallest resolvable object detail! The invention of aberration corrected instruments solves this problem as will be described in the following.

2.1.6 Aberration-corrected HRTEM

Shortly after the invention of the electron microscope in 1931 by Ernst Ruska and Max Knoll [35], Otto Scherzer published his famous electron-optical theorem in 1936 [36], which

says that the spherical aberration of a round electromagnetic lens is always positive and that there is no means to compensate this by the spherical aberration with opposite sign of another round lens. The only path to better resolutions seemed to be to minimize the aberrations of the lenses. Ironically, the man who had brought this problem over the young society of electron microscopists by his theorem, found the back door by himself in 1947 and proposed the correction would be possible by multipole lenses [37]. It took more than half a century until an attempt to solve this problem was successful in 1998 [38].

An improvement of the point resolution (equation (2.56)) is technically limited because the electron wavelength cannot be decreased by using much higher voltage power supplies beyond 1 MV (where beam damage of the specimen becomes an even more serious problem) and also the C_s cannot be lowered arbitrarily by improved lens fabrication.

In light optics spherical aberration and chromatic aberration as well can be corrected by doublets of a converging and diverging lens with different refractive index and dispersion. But in electron optics round lenses are always converging. The principle of the successful design of hexapole lenses as correctors is described in detail by [39] and [2]. A hexapole field with threefold symmetry introduces a small divergence to a bundle of rays with equal distance to the optical axis as well as a strong threefold symmetry as illustrated in figure 2.6. The ray displacement by the spherical aberration is proportional to r^3 (see equation (2.59)) and thus two opposite rays at distances r to the optical axis will gain small deflections that point into opposite directions in addition to the strong deflections into the same direction from the threefold symmetry of the field. The positive ray displacement of the objective lens, i.e. the spherical aberration, can now be fully compensated by the negative displacement that can be tuned by the strength of the hexapole field and the combined spherical aberration of the system becomes zero. By using a second hexapole system the threefold distortion can then be compensated by inserting a transfer system of round lenses between the two hexapoles that operates at magnification -1 and thus induces a point inversion between the hexapole planes: The threefold distortions cancel out while the divergences or convergences add up, producing positive or negative C_s.

The corrector is integrated into a transmission electron microscope by inserting another transfer doublet of round lenses between the objective lens and the hexapole system to image the coma-free point of the objector lens into the hexapole. The corrector elements are actually build as 12-poles for reasons of finer adjustment. Additional deflection coils are needed to match all optical axes of the elements. The final setup is schematically shown in figure 2.7.

Combining the small positive or negative spherical aberration with the defocus aberration of the objective lens allows to adjust for optimal phase contrast imaging. The information limit is given by the chromatic aberration. The approach by [40] is to extend the point resolution to the information limit and set $d_s = d_{inf}$ from equations (2.56) and (2.57), respectively, and calculate C_s:

$$C_s = \frac{16 d_{inf}^4}{3\lambda^3}, \tag{2.64}$$

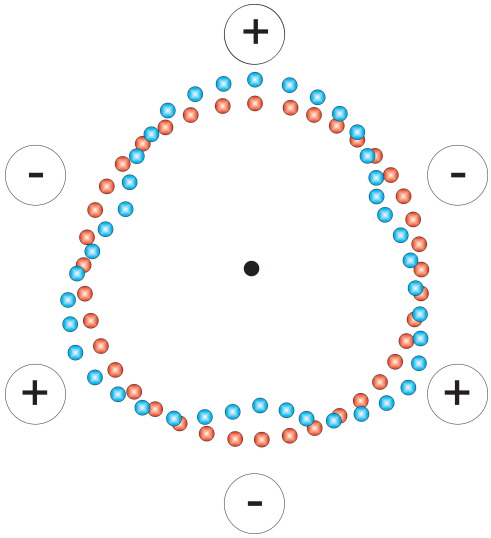

Figure 2.6: *Illustration of the threefold symmetry (blue circles) introduced by a hexapole field on the arrangement of a bundle of electron beams with initial equal distances (red circles) to the optical axis in the center. Minus and plus denotes the respective poles.*

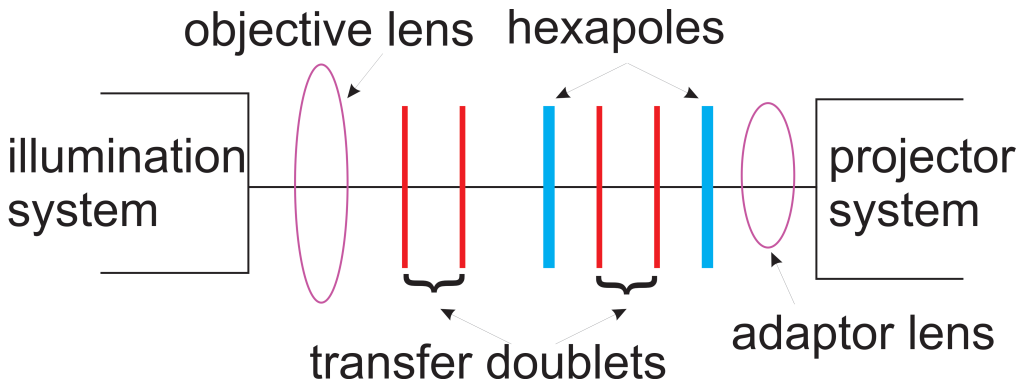

Figure 2.7: *Scheme of a transmission electron microscope with integrated double-hexapole corrector.*

and by inserting into equation 4.54 the optimum focus becomes

$$Z = -\frac{8d_{inf}^2}{3\lambda}. \tag{2.65}$$

The largest delocalisation for $g_{max} = 1/d_{inf}$ is then

$$R_{max} = \frac{8d_{inf}}{3}, \tag{2.66}$$

which is still quite large. It can be further reduced by optimising Z and C_s [40] to:

$$C_s = \frac{64d_{inf}^4}{27\lambda^3}, \tag{2.67}$$

and

$$Z = -\frac{16d_{inf}^2}{9\lambda}. \tag{2.68}$$

The result is a much smaller delocalisation of

$$R_{max} = \frac{16d_{inf}}{27}. \tag{2.69}$$

For this value of R_{max} the phase contrast is only reduced by about 10% which is still very good applicable for imaging. The setting above produces positive values for the spherical aberration and negative ones for the lens defocus. This derives from the strong positive spherical aberration of the objective lens and produces positive phase contrast, i.e. atom columns would appear dark compared to the mean intensity.

Under the weak-phase object approximation the object wave function was already derived (see equation (2.34)) and the *image plane wave function* from Scherzers $\pi/2$ criterion [1] estimated to

$$\Psi_{im}(\mathbf{r}) \approx 1 \pm \sigma V_p(\mathbf{r})t, \tag{2.70}$$

and thus the image intensity is

$$I(\mathbf{r}) \approx 1 \pm 2\sigma V_p(\mathbf{r})t + (\sigma V_p(\mathbf{r})t)^2. \tag{2.71}$$

For positive phase contrast now the minus in equation (2.71) would hold and the contrast is weakened by the linear and quadratic terms of opposite sign. Under negative phase contrast the linear and quadratic terms add up and the contrast modulation is enhanced. This situation is achieved with the double hexapole corrector by simply reversing all signs in the results of the optimum imaging conditions from equations (2.64), (2.65), (2.67) and (2.68)! The result is depicted by the blue curve in figure 2.5: The contrast transfer does not change in sign over wide regions of spatial frequencies by tuning C_s to negative values. The phase contrast extends to the information limit and the oscillations for high spatial frequencies do no longer occur.

The effect of negative phase contrast imaging (NCSI) of crystalline objects was first studied by numerical image simulations [41] and applied experimentally for atomic resolution imaging of oxygen columns in perovskite ceramics, confirming the theoretical results [6] [42]. One of the biggest advantages of this technique is the possibility to resolve weakly scattering atom columns in the direct neighbourhood of strong scattering ones.

The method of negative phase contrast imaging was applied successfully in this work to resolve the atomic columns at the interfaces of the misfit layered compound $(PbS)_{1.14}NbS_2$, where weakly scattering sulphur columns are located close to the much more strongly scattering niobium columns and even more strongly scattering lead columns.

2.1.7 Exit-wave reconstruction

The technique of exit-wave reconstruction (often also referred to as focal-series reconstruction) consists of two parts, an experimental and a computational one. In the experiment, a series of images with atomic resolution are taken under varying objective lens defocus conditions from the same sample area. Such a series can consist of 2 - 30 images that each exhibit different image contrast. During the second step the exit plane wave function is numerically computed from this series in order to generate the phase and amplitude information.

It was already stated that optimal imaging conditions in line with image simulations are appropriate techniques to reveal the atomic structure of an object. One might therefore ask, where the need for multiple image acquisition together with complicated numerical computations is. The answer lies in the fact that it *is* possible to take different images of the same object area by only changing some lens parameters. The object information is encoded in it and mixed with the information on the optical system that is used to image it. Considering now a very complicated object with hundreds of unknown atoms and positions, the method of (1) initial guess for image simulation, (2) comparison with experimental data and (3) changing the configuration of the lattice and start again with (1), will poorly work! For real systems this initial information is often simply not available and thus there is a need for a method that reliably delivers the wave funtion at the objects exit plane that is free from instrumental artefacts.

In order to understand the mathematical method of the focal-series reconstruction, the formal derivations of the last chapters are necessary. According to equation (2.45), the linear image intensity for a weak-phase object can be written as

$$I_L(\mathbf{g} \neq 0) = 2\mathcal{F}[\mathrm{Im}(\Psi_O(\mathbf{r}))] \sin(\chi(\mathbf{g})), \tag{2.72}$$

where Im denotes the imaginary part. The transition from the object wave function Ψ_O to the image plane wave function Ψ_I is given by

$$\Psi_I(\mathbf{g}) = \Psi_O(\mathbf{g}) \exp(-\mathrm{i}\chi(\mathbf{g})) = \Psi_O(\mathbf{g}) t(\mathbf{g}). \tag{2.73}$$

The complex valued *phase transfer function* $t(\mathbf{g}) = \exp(-\mathrm{i}\chi(\mathbf{g}))$ defines the *point-spread*

function $p(\mathbf{r})$, which is its inverse Fourier transform:

$$p(\mathbf{r}) = \mathcal{F}^{-1}[t(\mathbf{g})]. \tag{2.74}$$

Then the transition of the wave function from object to image plane can be described also in real space by a convolution:

$$\Psi_I(\mathbf{r}) = \Psi_O(\mathbf{r}) * p(\mathbf{r}). \tag{2.75}$$

Mathematically, a lateral delocalisation of information is described here, and the object wave function becomes blurred as a result. The radius of the point spread function was already derived in equation (2.61). There, $p(\mathbf{r})$ was written as $|\Delta r(\mathbf{g}, Z)|_{max}$. During the recording of a focal series for a thin film of given thickness t, parameters like wavelength, spherical aberration and information limit are fixed and the only remaining free parameter is the objective lens defocus. Since a series of many images is recorded, it is of no particular interest what defocus values are exacly used. But care should be taken not to waste information, which can occur in real space by choosing a defocus which causes an unnecessarily large radius of the point-spread function. Due to the convolution in (2.75), object points which are at a distance closer than R from the edge of the recorded area, spread information outside that will be lost. For this reason the reconstructed object area should always be smaller than the recorded one. The reconstructed object area can be maximized by keeping R and thus $\nabla\chi$ small, resulting in focus values nearby the optimum focus from equation (2.68) but with inverted sign. Practically it is sufficient to take the series around the zero defocus for a C_s corrected instrument due to a theoretical overestimation of the point spread and thus Z_{opt}. The reason for this are influences of the atomic scattering amplitude for higher scattering angles. For an uncorrected FEG instrument, the focal series should be taken at values around Scherzer or Lichte defocus.

In equation (2.72) a dispersive phase shift of a real objective lens was added to the wave function. Adding a cosine term to describe the dispersive nature of the imaginary part of the phase contrast transfer in addition to the real part described by the sine and defining

$$\begin{aligned} X(\mathbf{g}) &= 2\mathcal{F}[Re(\Psi(\mathbf{r}))] = \Psi(\mathbf{g}) + \Psi^*(-\mathbf{g}) \\ Y(\mathbf{g}) &= 2\mathcal{F}[Im(\Psi(\mathbf{r}))] = -\mathrm{i}\Psi(\mathbf{g}) - \Psi^*(-\mathbf{g}), \end{aligned} \tag{2.76}$$

yields:

$$I_L(\mathbf{g} \neq 0) = X_O(\mathbf{g})\cos(\chi(\mathbf{g})) + Y_O(\mathbf{g})\sin(\chi(\mathbf{g})). \tag{2.77}$$

$X(\mathbf{g})$ and $Y(\mathbf{g})$ are generally complex-valued Fourier coefficients that hold the Friedel symmetry $X(-\mathbf{g}) = X^*(\mathbf{g})$. The subscript O refers again to the object wave function (opposed to I for the image wavefunction). In linear algebra vector notation the equation can be rewritten to:

$$I_L(\mathbf{g} \neq 0) = \left[\begin{pmatrix} \cos(\chi(\mathbf{g})) & \sin(\chi(\mathbf{g})) \\ -\sin(\chi(\mathbf{g})) & \cos(\chi(\mathbf{g})) \end{pmatrix} \begin{pmatrix} X_O(\mathbf{g}) \\ Y_O(\mathbf{g}) \end{pmatrix} \right] \begin{pmatrix} 1 \\ 0 \end{pmatrix} = \begin{pmatrix} X_I(\mathbf{g}) \\ Y_I(\mathbf{g}) \end{pmatrix} \begin{pmatrix} 1 \\ 0 \end{pmatrix}. \tag{2.78}$$

Note, that the vector $(X(\mathbf{g}), Y(\mathbf{g}))$ carries now the real part transfer in the first and the imaginary part transfer in the second dimension. The term in the square brackets describes a frequency-dispersive rotation of the real and imaginary parts from the object wave function to the final image plane wave function. The multiplication with the vector $(1, 0)$ is a projection of the image-plane wave function onto the real-axis of the complex number plane, where only its real part contributes to the image intensity. This complex number plane should not be confused with the one in Fourier space that refers to the single vector coefficients X and Y.

As figure 2.8 shows, the equation can be visualized as a helical surface that is winding around the spatial frequency axis in the three dimensional (Re, Im, g) space. This surface represents the *complex valued phase transfer function* $t(\mathbf{g})$. The real and imaginary parts of the initial object wave function are mixed by the rotation matrix dependent on the spatial frequency. A projection of the helical surface onto the real axis yields the cosine transfer function $\cos(\chi(\mathbf{g}))$ and a projection onto the imaginary axis the sine transfer function $\sin(\chi(\mathbf{g}))$ that was already introduced with equation (2.45) as the CTF.

At low frequencies, the contrast is dominated by the cosine transfer function that is close to 1 while the sine is ~ 0. Therefore larger ($> 1nm$) object detail contrast is always transferred by the cosine function and thus the intensity is due to contributions nearly exclusively of the real part of the wave function.

As can also be seen in figure 2.8, the sign of the winding given by the sign of the gradient of $\chi(\mathbf{g})$ can change in direction, explicitly in the middle of the Scherzer passband where the spherical aberration and defocus have opposite signs. From equation (2.61) one can also see that strong beam displacements $\Delta\mathbf{r}(\mathbf{g})$ invoke high winding frequencies for the associated $\mathbf{g}$.

Equation (2.78) can also be written as:

$$\begin{aligned} I_L(\mathbf{g} \neq 0) &= \begin{pmatrix} X_O(\mathbf{g}) \\ Y_O(\mathbf{g}) \end{pmatrix} \left[\begin{pmatrix} \cos(\chi(\mathbf{g})) & -\sin(\chi(\mathbf{g})) \\ \sin(\chi(\mathbf{g})) & \cos(\chi(\mathbf{g})) \end{pmatrix} \begin{pmatrix} 1 \\ 0 \end{pmatrix} \right] \\ &= \begin{pmatrix} X_O(\mathbf{g}) \\ Y_O(\mathbf{g}) \end{pmatrix} \begin{pmatrix} \cos(\chi(\mathbf{g})) \\ \sin(\chi(\mathbf{g})) \end{pmatrix} \end{aligned} \tag{2.79}$$

Now the projection axis $(1, 0)$ is rotated in the image plane to form a new projection axis $(\cos(\chi), \sin(\chi))$. Taking a focal series with different Z and thus different χ values yields now a tomographic recording as a function of $\mathbf{g}$ of the object wave function into a direction of the complex number plane given by the right-hand side of the above equation, because the winding of the helical surface changes as a function of χ. Therefore the method is sometimes referred to as *defocus-variation principle*.

During the reconstruction the projection direction for each spatial frequency value g is different because of the non-linear correlation of $\nabla\chi$ and g in equation (2.60). The rotation axis on a particular (Re, Im) plane for a certain g has to be determined because the projection helix does not rotate as a whole, but slow for lower frequencies and faster for higher ones due to the quadratic term of g in (2.60). For each spatial frequency a different set of projections of the object wave function is included in a focal series.

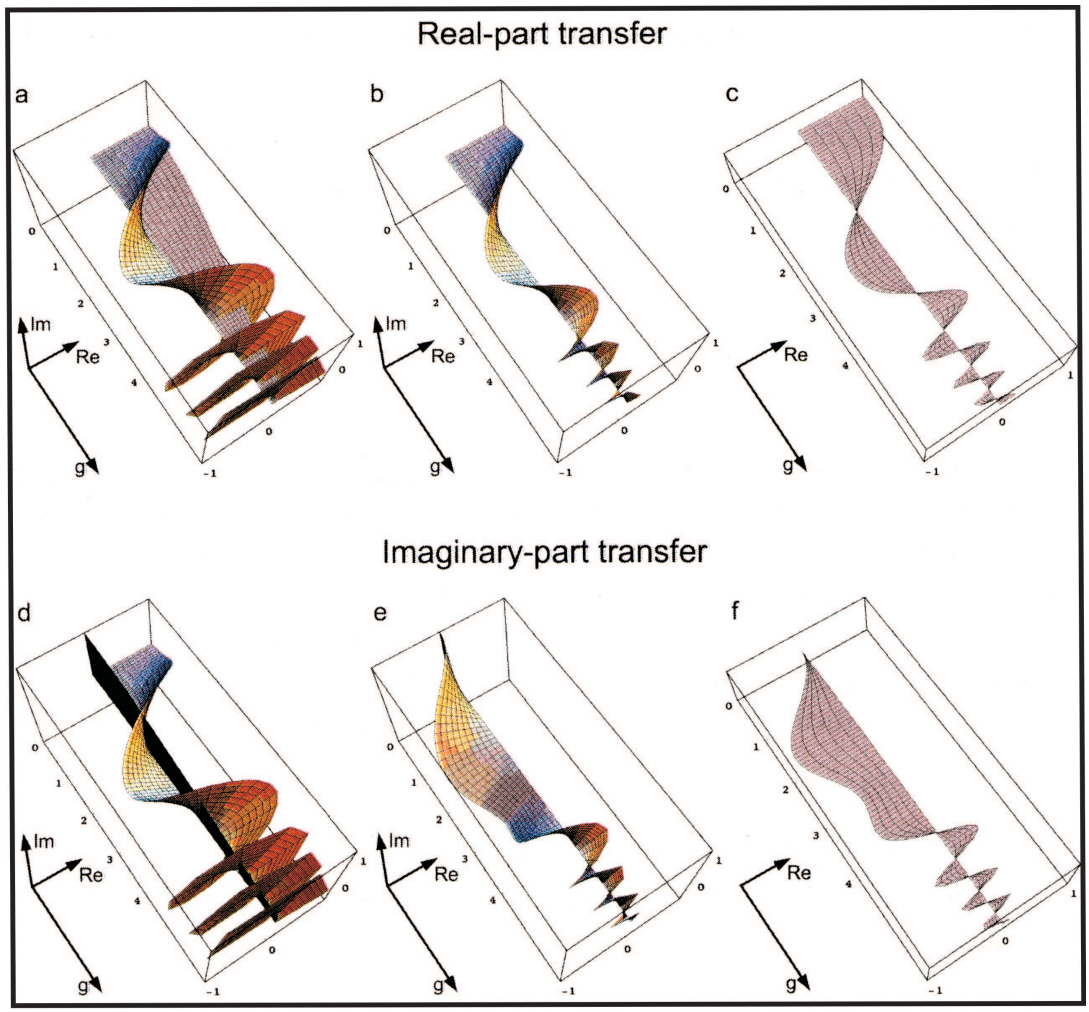

Figure 2.8: *Illustration of the frequency-dispersive linear real- and imaginary-part contrast transfer within an electron microscope at Scherzer defocus from [43]. The object wave function is for both the real-part (a-c) and the imaginary part (d-f) visualized as a Gaussian for simplification. The contrast is transferred by a projection onto the complex number plane (Re, Im) as described by equation (2.78) as a function of the spatial frequency g. (a) By the phase transfer function* $t = \exp(-i\chi(g))$ *the surface of the helix displayed is defined in such a way, that the object wave function is rotated around the g axis by an angle* $-\chi(g)$ *to yield its contribution to the image-plane wavefunction that is shown in (b). Its projection onto the real axis shown in (c) illustrates the real part object wavefunctions contribution to the linear image intensity. The imaginary part of the object wave funtion (again represented by a Gaussian) is transferred in the same way as shown in (d), (e) and (f). The projection onto the real axis in (f) yields the CTF.*

From the considerations above, the approach for the linear reconstruction of the real and imaginary part of the object wave function can be derived. A focal-series recorded with N different images and different focal values Z_n generates N aberration functions

$$\chi_n(\mathbf{g}) = 2\pi(\frac{1}{4}C_s\lambda^3\mathbf{g}^4 + \frac{1}{2}\lambda Z_n\mathbf{g}^2). \tag{2.80}$$

Multiplication of equation (2.77) with $\cos(\chi(\mathbf{g}))$ and $\sin(\chi(\mathbf{g}))$ and summation over the N images gives the two complex valued linear equations for $X_O(\mathbf{g})$ and $Y_O(\mathbf{g})$.

$$\sum_{n=1}^{N} I_{L,n}(\mathbf{g})\cos(\chi_n(\mathbf{g})) = X_O(\mathbf{g})\sum_{n=1}^{N}\cos^2(\chi_n(\mathbf{g})) + Y_O(\mathbf{g})\sum_{n=1}^{N}\cos(\chi_n(\mathbf{g}))\sin(\chi_n(\mathbf{g})),$$

$$\sum_{n=1}^{N} I_{L,n}(\mathbf{g})\sin(\chi_n(\mathbf{g})) = X_O(\mathbf{g})\sum_{n=1}^{N}\cos(\chi_n(\mathbf{g}))\sin(\chi_n(\mathbf{g})) + Y_O(\mathbf{g})\sum_{n=1}^{N}\sin^2(\chi_n(\mathbf{g})). \tag{2.81}$$

Those equations need to be solved for each $\mathbf{g}$ and one can find detailed information in the literature [44] [45] [46] [21] [47] [48] [49] [50] [51] on the analytical and numerical approaches that where derived over the past decades as well as on the expansion of the equations for non-linear reconstructions. In this context, only some important issues will be discussed that give practical hints for experimental work.

(i) A serious problem is the *low-frequency gap* that appears due to the nearly absent rotation of the projection helix for small g values. Nearly only the real part of the wave function is projected by the cosine transfer. This would then basically be the same as the intensity content for low frequencies of the recorded image.

A consensus states that projections are assumed to be sufficiently different for reconstructing a certain g when an angle of $\pi/4$ is exceeded by the helical surface between the first and last image. Then the lowest reconstructible frequency for the *total focal length* L with $L = (N-1)\delta$ of a series can be estimated to be:

$$g_{min} = \frac{1}{2}\sqrt{\frac{1}{\lambda L}}. \tag{2.82}$$

From this formula it becomes clear that by increasing the number of images N taken at equidistant focal steps δ (the step size should be always constant) the lowest reconstructible frequency is decreased.

(ii) A second problem is evoked when the images in an equidistant series are taken accidently in such a manner, that the projection direction changes from an image to the next in multiples of π, because in that way it would e.g. be possible that only the real part of the wave function for a certain frequency will be recorded again and again without any information of the imaginary part. This phenomenon of a frequency gap is called *blind spot*. Such a resonance frequency occurs when $\pi\lambda\delta g^2 = n\pi$ and thus blind spots can only be avoided up to the first resonance frequency of

$$g_{res} = \sqrt{\frac{1}{\lambda\delta}}. \tag{2.83}$$

Choosing δ in a manner that pushes this threshold beyond the information limit solves this problem.
newline

On the one hand the focal step size should be preferrably large to maximize L, on the other hand so small that resonances below g_{max} are avoided. By claiming that the phase changes should be below $3/4 \cdot \pi$ at g_{max}, an optimum step size of

$$\delta_{opt} = \frac{3}{4\lambda g_{max}^2} \tag{2.84}$$

is a good compromise to match both conditions at the same time.

Additionally, it is advised that the recorded series contains about 10 - 20 images. Lower numbers lead to increased blind spot regions and for much more images the effect of increasing beam damage will become a problem.

2.1.8 Numerical aberration correction

The ability of an aberration-corrected HRTEM to control the defocus and spherical aberration as well as higher order aberrations (that will be discussed in chapter 4) during the experiment leads to much more precise information about the instruments parameters during the image acquisition. Another goal of numerical aberration correction is to be able to correct for any residual objective lens aberrations *after* the images have been acquired. When used for this pupose, methods that are able to construct the phase of the object wave function like focal-series reconstruction are also very powerful tools.

The oversimplified picture that takes only the defocus and spherical aberration into account need to be expanded to include other aberrations that affect the wave function and thus the image. Those can not be entirely corrected by the hardware during the experiment and, even worse, some of them vary in time dramatically. It is well known, that reconstructed wave functions show those residual aberrations. Luckily, given that an aberration is known, it is much more easier to correct the wave function numerically afterwards that suffers from the aberration, than it is to remove the aberration from an image. Even more, in an optimal situation, the residual aberrations itself can be determined from the wavefunction [52].

Assuming a reconstructed wave function $\Psi_R(\mathbf{g})$ with a residual aberration χ_R, then

$$\Psi_R(\mathbf{g}) = \Psi_O(\mathbf{g}) \exp(-\mathrm{i}\chi_R(\mathbf{g})) \tag{2.85}$$

can be solved for the aberration-free object wave function $\Psi_O(\mathbf{g})$ by constructing a *numerical phase plate* $\chi_R(\mathbf{g})$.

The aberration function can be expanded as a series, which should be done in polar coordinates (g, φ), because unlike Z and C_s a general residual aberration is not isotropic. The contributions to $\chi_R(\mathbf{g})$ can then be written as

$$\chi_{mn}(g, \varphi) = 2\pi \left(\frac{1}{m} w_{mn} g^m \cos[n(\varphi - \varphi_{mn})] \right), \tag{2.86}$$

with $m \leq n$, $m+n$ even, and the wave aberration coefficients w_{mn}. For example, w_{20} equals Z in this notation and w_{40} the sperical aberration C_s.

The ability to correct for residual aberrations after the image aquisition is also included in the *TrueImage* software package that was used for the focal-series reconstructions of the aberration-corrected HRTEM images of the misfit layered compound $(PbS)_{1.14}NbS_2$.

2.2 Fundamentals of HAADF-STEM

With the scanning transmission mode of the electron microscope (STEM) an image is produced by scanning a strongly focussed electron beam across a thin sample and collecting the electrons scattered into large angles by a so-called high-angle annular dark field (HAADF) detector. The integrated number of scattered electrons that are collected for each probe postion are displayed on a synchronized display during the rastering process. STEM became an important and powerful complementary technique to the TEM method because also many types of analytical spectroscopic signals can be used to produce an image of the scanned area. Annular dark field (ADF) imaging using high-angle scattering that occurs localised near individual atoms became the primary imaging technique because it combines the advantage of a high sensitivity to the atomic number Z with high lateral image resolution and allows for a very direct interpretation of the images.

The STEM was invented shortly after the conventional TEM by von Ardenne in the late 30's [53] and could be improved about 3 decades later to a high degree by the addition of field-emission electron guns [54]. With the introduction of the annular dark field detector further advancement of the technique was achieved leading to the successful imaging of single atoms and atom clusters [55]. By increasing the collection angles of the detectors beyond the probe forming angle, the dependence of the signal on the atomic number Z dominates the coherent Bragg scattering contrast. The HAADF detectors reduce the degree of coherence by predominantly collecting thermally diffuse scattered electrons [56] [57]. The contrast produced by electrons at large scattering angles is strongly dependent on the atomic number Z and thus enables chemical maps of the specimen in two dimensions [58]. The performance of STEM microscopes was further improved and first ADF images were taken at atomic resolution with bright peaks denoting the atom sites and without any contrast reversals present in coherent imaging by HRTEM [59].

Figure 2.9 (a) shows a schematic illustration of a STEM geometry. Above and below the drawn section the condensor lenses, scanning coils and post specimen lenses of the combined STEM and TEM instruments would be situated but these are not shown here for simplifications. The focal length of the objective lens is typically about 3 mm and the illumination semiangles α are about 10-30 mrad for instruments with an acceleration voltage of 100 kV to 300 kV. The collection angles are in the range of a few 100 mrad for the high-angle diffracted electrons.

A focussed electron probe $\Psi_p(\mathbf{x}, \mathbf{x_p})$ of an incident electron beam $\Psi_{inc}(\mathbf{x})$ impinges onto a thin sample and the electrons become scattered. At the exit plane of the sample their amplitude distribution is described by the complex valued wave function $\tilde{\Psi}_t(\mathbf{k'}, \mathbf{x_p})$

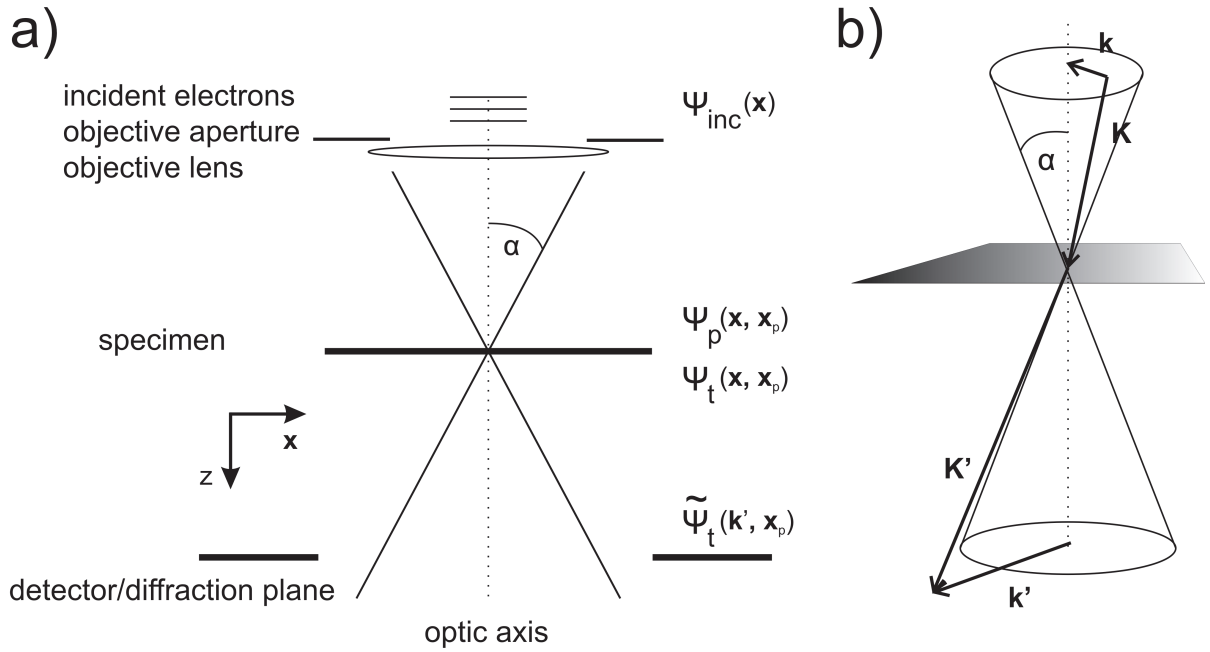

Figure 2.9: *(a) Sketch of a STEM with annular dark field detector in the diffraction plane. An incident electron wave function $\Psi_{inc}(\mathbf{x})$ is diffracted within a sample, its amplitude distribution can be described by the complex valued wave function $\tilde{\Psi}_t(\mathbf{k}', \mathbf{x_p})$ for each position $\mathbf{x}_p$ on the sample. (b) Illustration of the diffraction process that transfers the incident plane wave with wave vector $\mathbf{K}$ and its transverse component $\mathbf{k}$ within the objective aperture into an outgoing wave with wave vector $\mathbf{K}'$ and its transverse component $\mathbf{k}'$.*

for each position $\mathbf{x}_p$ on the sample. $\mathbf{k}'$ is the transverse component of the wave vector of the diffracted electron as figure 2.9 (b) shows. $\mathbf{k}'$ is two dimensional with $|\mathbf{k}'| = 2\sin(\theta/2)/\lambda$ with the diffraction angle θ and electron wavelength λ.

$\mathbf{k}'$ represents a point in the far field of the specimen and therefor $\tilde{\Psi}_t(\mathbf{k}', \mathbf{x_p})$ is given as the Fourier transform of the complex-valued amplitude function of the electron wave at the exit surface $\Psi_t(\mathbf{x}, \mathbf{x_p})$ of the sample:

$$\tilde{\Psi}_t(\mathbf{k}', \mathbf{x_p}) = FT[\Psi_t(\mathbf{x}, \mathbf{x_p})]. \tag{2.87}$$

The useful local information about the scattering properties of the specimen and the interaction between probe and specimen are included in the variations of $\Psi_t(\mathbf{x}, \mathbf{x_p})$ for different $\mathbf{x}_p$. $\mathbf{k}'$ represents a point on a detector situated in the diffraction plane. The image intensity observed as a function of the probe position is then given by

$$I(\mathbf{x}_p) = \int D(\mathbf{k}')|\tilde{\Psi}_t(\mathbf{k}', \mathbf{x_p})|^2 d^2k' \tag{2.88}$$

where $D(\mathbf{k}')$ describes the detector area in the diffraction plane.

For the determination of $\tilde{\Psi}_t(\mathbf{k}', \mathbf{x_p})$ another complex valued function $F(\mathbf{k}, \mathbf{k}')$ that represents the scattering amplitude of the initial partial plane wave with wave vector $\mathbf{k}$ in the probe into a plane wave with $\mathbf{k}'$ in the image plane.

Under coherent illumination the focussed probe in the specimen plane is calculated by an integration over the objective aperture $A(\mathbf{k})$ of the aberration function $\exp(-\mathrm{i}\chi(\mathbf{k}))$ of the objective lens [60]:

$$\Psi_p(\mathbf{x}, \mathbf{x_p}) = \int \underbrace{A(\mathbf{k}) \exp(-\mathrm{i}\chi(\mathbf{k}))}_{=:\hat{A}(\mathbf{k})} \exp(-2\pi\mathrm{i}\mathbf{k}(\mathbf{x} - \mathbf{x_p}))d^2k. \tag{2.89}$$

$A(\mathbf{k})$ represents a circular aperture with $A(\mathbf{k}) = 1$ for $|k| \leq k_{max} = \lambda\alpha$ and $A(\mathbf{k}) = 0$ for any other $|k|$.

The diffraction process modifies the wave function at the exit plane of the specimen to

$$\Psi_t(\mathbf{k}', \mathbf{x_p}) = \int \hat{A}(\mathbf{k}) \exp(-2\pi\mathrm{i}\mathbf{k}(\mathbf{x} - \mathbf{x_p}))F(\mathbf{k}, \mathbf{k}')d^2k \tag{2.90}$$

which can be inserted into equation (2.88) and yields then an expression for the image intensity that is collected when the electron probe is situated on the specimen at a position $\mathbf{x_p}$:

$$I(\mathbf{x}) = \int\int\int D(\mathbf{k}')F(\mathbf{k}, \mathbf{k}')F^*(\mathbf{k}+\mathbf{g}, \mathbf{k}')\hat{A}(\mathbf{k})\hat{A}^*(\mathbf{k}+\mathbf{g}) \exp(2\pi\mathrm{i}\mathbf{g}\cdot\mathbf{x}_p)d^2k'd^2kd^2g, \tag{2.91}$$

with a reciprocal lattice vector $\mathbf{g}$.

That is the Fourier transform of the expression

$$I(\mathbf{g}) = \int\int D(\mathbf{k}')F(\mathbf{k}, \mathbf{k}')F^*(\mathbf{k}+\mathbf{g}, \mathbf{k}')\hat{A}(\mathbf{k})\hat{A}^*(\mathbf{k}+\mathbf{g})d^2k'd^2k. \tag{2.92}$$

For the special case of incoherent imaging with an annular dark field detector $D(\mathbf{k}')$ with an inner and outer collection angle k_i' and k_o' respectively with $D(\mathbf{k}') = 1$ for $k_i' \leq |\mathbf{k}'| \leq k_o'$ and $A(\mathbf{k}) = 0$ for any other $|\mathbf{k}'|$, equation (2.92) can be simplified:

$$I(\mathbf{g}) \approx \int \hat{A}(\mathbf{k})\hat{A}^*(\mathbf{k}+\mathbf{g})d^2k \int D(\mathbf{k}')F(\mathbf{k}, \mathbf{k}')F^*(\mathbf{k}+\mathbf{g}, \mathbf{k}')d^2k' \tag{2.93}$$

$$= FT^{-1}(|PSF(\mathbf{x}, \mathbf{x_p})|^2)FT^{-1}(|O(\mathbf{x})|^2). \tag{2.94}$$

The point spread function in this equation is equal to the probe function $\Psi_p(\mathbf{x}, \mathbf{x_p})$. The object function $O(\mathbf{g}) = FT^{-1}(O(\mathbf{x}))$ carries the information about the scattering properties of the sample.

If the crystal is very thin with a periodic scattering potential in the direction of the incoming beam, the object function is a convolution of the square of the electrostatic potential with an Airy function with a diameter inversely proportional to the inner angle of the detector [61]. In the case when the detector inner angle is large enough so that

the diffraction limit does not destroy the resolution of object details, the object function represents a direct image of the specimen projected potential.

The ADF image intensity is thus given by the convolution of the square of the probe function and the object function:

$$I(\mathbf{x}_p) = |PSF(\mathbf{x}, \mathbf{x_p})|^2 * |O(\mathbf{x})|^2. \tag{2.95}$$

In this picture of image formation, the image is that of the object function altered by the probe shape but without interference effects. The detector geometry plays an important role if the incoherent image formation model should be valid. Its inner aperture has to be much larger than the object aperture that is used. The inner radius should be three times larger than the probe convergence angle to yield the incoherence [62].

As a characteristic feature, HAADF images show always bright dots at the position of atomic columns regardless of the focus setting.

Chapter 3

The misfit layered compounds

The class of transition metal dichalcogenide (TMDC) misfit layer compounds with the general formula $(MX)_n(TX_2)_m$ (M = Sn, Pb, Bi or rare earths; X = S, Se, Te; T = Ta, Ti, Nb, V; n = 1.08....1.19; m = 1,2,3) is built up by two very different subsystems consisting of distorted rock salt MX with a cubic NaCl structure and sandwich layers of TX_2. The MX layer hosts two atomic slices of a cubic monochalcogenide while the TMDC sandwich consists of three atomic layers stacked in a XTX-scheme. In a monocrystalline system, the properties of the two subsystems differ from each other significantly. In this chapter the structure and physical properties of the single constituents will be described first, followed by a detailed overview about the misfit compounds in general.

3.1 Transition metal dichalcogenides

The transition metal dichalcogenides TX_2 with a group IVb (Ti, Zr, Hf), Vb (V, Nb, Ta) or VIb (Cr, Mo, W) metal T and a chalcogen X (S, Se, Te) are often referred to as "sandwich"layered compounds, i.e. they are built up by three atomic layers that are stacked with the chalcogen on top and bottom and the metal in between. The transition metal atoms are arranged hexagonally and each of them is surrounded by six chalcogen atoms that are as well hexagonally ordered in the two layer planes above and below the metal (see figure 3.1) [7].

While within the sandwiches the bonds are of covalent and ionic character, they are saturated on the surface of the chalcogenide planes and therefore the interaction between neighbouring sandwich layers is of a weak van-der-Waals type. This leads to the phenomenon that physical properties like electrical and thermal conductivity as well as mechanical and optical attributes show a pronounced two-dimensional character. From this origin is the term "quasi 2-dimensional material"derived which is often to referred when the special features of the TMDCs are explained.

Despite their similar structure the TMDCs show still differences in their crystallography. As figure 3.1 (b) and (c) shows, the transition metal atom can be surrounded by the six nearest neighbouring chalcogen atoms in two different ways, reflected by the so called 1T and 2H structures. In the case of the 1T structure the chalcogen atoms form

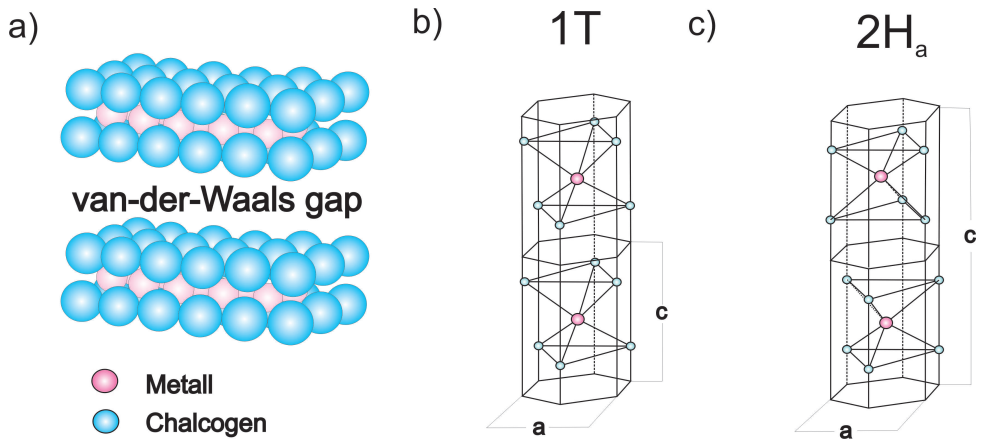

Figure 3.1: *(a) Schematic drawing of the sandwich structure of the transition metal dichalcogenides. (b) The unit cells of the octahedral 1T and (c) trigonal prismatic* $2H_a$ *polytype.* NbS_2 *possesses the* $2H_a$ *configuration.*

a octahedron and the unit cell consists of a single slab of this arrangement in c direction, the space group is the symmorphic $P\bar{3}m1$. The trigonal prismatic $2H_a$ structure with the non-symmorphic space group $P6_3/mmc$ is in contrary to that expanded over two sandwiches that are rotated by 180° towards each other, where the chalcogen atoms are stacked on top of each other within one slab. The compound under investigation in this thesis, NbS_2, possesses the $2H_a$ configuration. Other polytypes like $2H_b$, 3R etc. exist also and the nomenclature results from different stacking sequences of the layers with the integer indicating the number of layers present in a single unit cell.

The differences in structure finds direct representation in the electrical, magnetic and optical properties of the various compounds and were described first by Wilson and Yoffe [7] via the electronic structure by a simple model. Figure 3.2 shows the energy positions of the relevant band states near the Fermi edge. The s- and p- orbitals of the chalcogen atoms are divided into occupied and unoccupied (antibonding and bonding) σ and $\sigma*$ band states. The metal d states are positioned in the energy gap between those and split up into a twofold degenerated level e_g (the d_{xz} and d_{yz} orbitals) and a threefold degenerated level t_{2g} (the d_{z^2}, $d_{x^2-y^2}$ and d_{xy} orbitals). The authors describe the various characters of the compounds within a simple ionic picture by the amount of filling of the d bands: The transition metal loses two electrons to the chalcogen atoms to fill their p orbitals completely, while the remaining electrons can occupy the d_{z^2} states. In the case of the IVb transition metals the configuration is d^0 and the d_{z^2} band is unoccupied, resulting in semiconductive properties. In a TMDC with group Vb transition metals the band becomes half filled and the respective compounds are metallic. A system with a complete filled d_{z^2} band from electrons from group VIb elements then again induces semiconducting behaviour and the band is separated from the other d states and significantly lowered in energy.

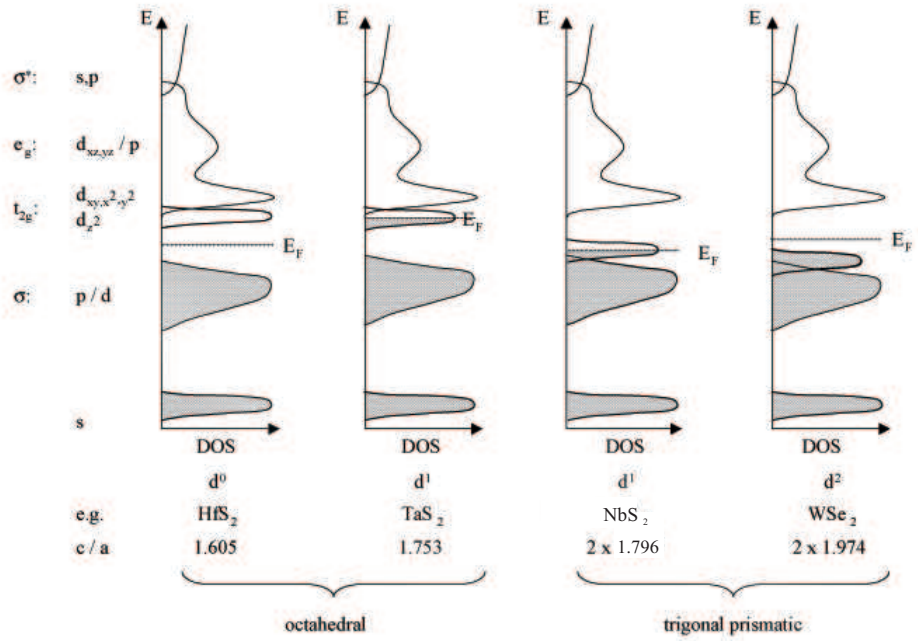

Figure 3.2: *Simplified model describing the electronic structure of the transition metal dichalcogenides after [7]. The bonding and antibonding σ and $\sigma*$ states are from the chalcogen compound, the mixed e_g and t_{2g} states are derived from the transition metal d states that split up.*

These electronic properties are directly linked to the structure, for the coordination of chalcogen atoms are octahedral for group IVb metals and trigonal prismatic for those of group VIb. Only Vb compounds can be found in both configurations.

Intercalation

The van-der-Waals gap between the layers of the TMDCs is of particular interest because of its ability to act as a host for intercalating atoms, molecules or even crystals. Intercalation here is defined as a reversible process of atom insertion into the van-der-Waals gap of a TMDC host structure without changing it. This can alter the physical properties of the whole system by modification of the electronic structure and is examined with regard to practical applications like designing semiconductor heterostructures with certain desired properties. Detailed studies on various intercalates [63] like alkali and other metals [8], 3d transition metals [64], and organic molecules [65] are described in the literature.

Noticable results from intercalation are e.g. the achievement of transitions from semiconducting to metallic behaviour or inducing superconductivity within a compound. As the driving force behind the intercalation a charge transfer from the guest to the host lattice is detected. There are two competing models describing this process, the rigid band and the band shift modell. While the latter describes the reduction of the perpen-

dicular dispersion of the electronic states and thus the change in band gaps and band widths, the former assumes the band structure of the host system to be unchanged and the conduction bands being filled up with electrons from the intercalate due to the charge transfer, which would bear the fact that only electron donors can be intercalated. But this assumption is not applicable by all means, as the host layers can be decoupled and change the band structure even at an early stage of the intercalation process.

Intercalation can be realised by varying methods, e.g. alkali metals can be intercaleted by immersion of the host in alkali-ammonia solutions [63], electrolysis or by *in-situ* deposition in vacuum onto a clean surface [76] or directly built in during the crystal growth process [64]. It is important to state that the process of the intercalation iself is until now not well understood and there is still a lively debate on that.

As the band shift model predicts, the strict definition of intercalation mentioned above is not satisfactory as additional other changes like modified layer interactions, altered layered spacings and so on are reported also [63]. Consequently the definition can be loosened to only state that TMDCs are called intercalated when the guest atoms, molecules or crystals doesn't disturb the layered character. The misfit layered compounds are according to that a strongly intercalated transition metal dichalcogenide with the guest being slabs of crystals itself.

Electric transport measurements show that this definition is not only formal: the observed properties are similar to those of metal atom intercalated compounds, giving rise to the assumption that the conduction happens exclusively in the TMDC layers [8].

However, the crystal structure is well known and the quality of the bulk and surface material of the samples after growth is astonishingly high, regarding the fact that those systems are grown by the chemical vapour transport method, which is described in more detail in chapter 4.

3.2 The cubic monochalcogenide PbS

The MX constituent of the misfit layered compounds is a cubic rock salt monochalcogenide with M being divalent Sn, Pb, Bi or trivalent rare earths, and X the chalcogen S or Se. PbS, which is the MX part in the misfit layered compound investigated in this thesis, exists in nature as a natural mineral called galena and crystallizes in the rock salt structure as depicted in figure 3.3. It consists of two face centered cubic (fcc) lattices, resulting in a body centered cubic (bcc) Brillouin zone.

The bonding is of ionic and covalent type [66] and the structure exists only in this monotype as opposed to e.g. SnS that shows a temperature dependent transition between two structural phases α and β [67]. PbS and SnS are group IV-VI semiconductors with a direct band gap of 0.41 eV and 1.08 eV at room temperature respectively [68] [69]. Actually PbS was one of the first semiconductors ever used industrially and is today applied in a broad number of electronic devices like detectors or lasers.

The group V element Bi doesn't exist in a BiS configuration with the oxidation state 2+ like the two other compounds, but is observed as Bi_2S_3 in a 3+ state.

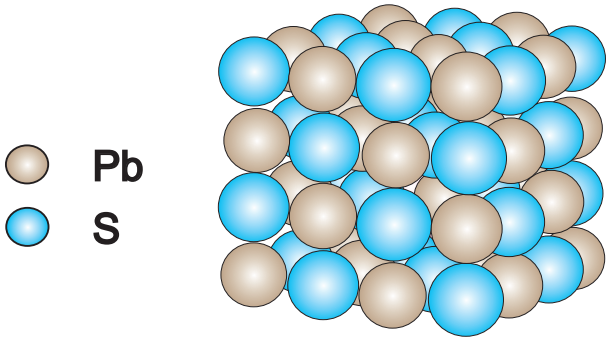

Figure 3.3: *Scheme of the rock salt crystal structure of PbS (galena).*

While the bulk properties are well understood, aspects of changes in the surface geometry and thus the electronic structure were discussed controversally in the literature up to the present days. Since in the crystal structure of the misfit layered compound one finds the MX compound consisting of surfaces exclusively, potential influences of that have to be taken into account. Discrepencies arise from theoretically predicted surface core level shifts for both the Pb and S states [66] that could not be veryfied in experiments. Possible explanations would be the strong electron-phonon coupling in PbS [70] or a relaxation of the partial [71] or entire [66] surface plane resulting in a structural change.

A further phenomenon regarding the surface structure is reported by [72]: During cleavage under ultra high vacuum conditions, a small percentage (about 0.1%) of the S atoms evaporate into the vacuum. Hence a Fermi level shift towards the conduction band appears and the surface becomes an n-type semiconductor after some hours while the bulk states remain unchanged. After some more hours of oxygen evaporation and repeated measurements this shift can no longer be observed and the surface band structure is the same as before. This can be explained in a way, that the oxygen atoms fill the sulfur vacancies and restore the surface structure. Of analogical interchanges between the Pb and metal atoms at interfaces or after evaporation is furthermore reported in [73] and [74].

The ability of the surface to relax and to reconstruct by atom interchange is particularly interesting when one considers that in the misfit layered compound the surfaces of the PbS slabs are in direct contact with the transition metal and chalcogen atoms of the TMDC.

3.3 Misfit layered compounds

As described in the previous sections the misfit layered compounds consist of alternating stacking of up to three hexagonal transition metal dichalcogenides and double layers of cubic rock salt monochalcogenide with the general formula $(MX)_n(TX_2)_m$ (M = Sn, Pb, Bi or rare earths; X = S, Se, Te; T = Ta, Ti, Nb, V; n = 1.08....1.19; m = 1,2,3). Such layered systems can be understood as an intercalated TMDC with the monochalcogenide

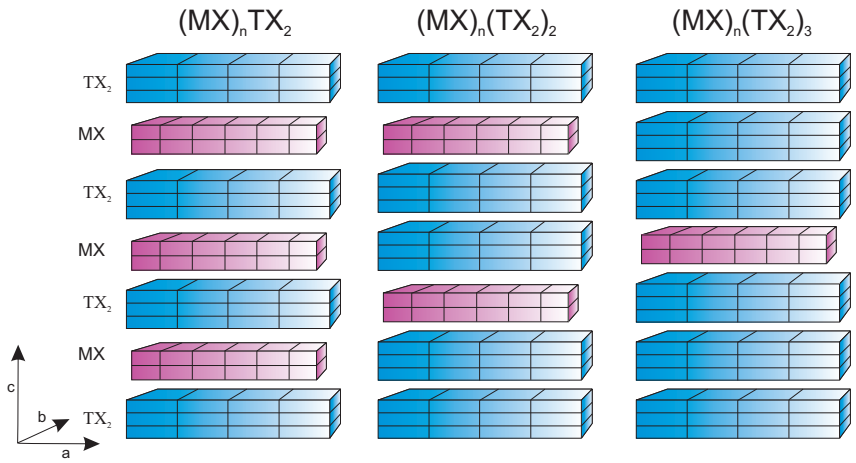

Figure 3.4: *Scheme of the three main types of transition metal dichalcogenide misfit compounds* $(MX)_n(TX_2)_m$ *(n = 1.08....1.19) for m = 1, 2, 3. The differences in the lattice constants in* **a** *direction lead to the incommensurability and thus to the term misfit.*

being intercalated into the van-der-Waals gaps of the TMDC compound [9]. Figure 3.4 shows schematically the structures of the compounds for m = 1, 2, 3.

As a result of the different lattice constants in **a** direction these systems have incommensurate interfaces between each MX and TX_2 slab. This is the origin of the term misfit compound. In contrast the crystal structure is commensurate in the **b** direction.

Figure 3.5 shows the general misfit layered compound and its lattice in more details: The directions of the lattice vectors **a**, **b**, **c** of the TMDC subsystem are the same as those of the MC compound, called **a'**, **b'** and **c'** in the following. For the hexagonal TMDC one can define **b** as orthogonal to **a** with $b = a \cdot \sqrt{3}$ and for the undistorted TMDC and MC layers **a'** and **b'** are then parallel to **a** and **b** respectively, as well as **c** and **c'**.

In real misfit layered compound systems one always finds individual layers to be distorted due to multiple reasons. E.g., the subsystems show mutual modulations with the goal to make the **b** and **b'** lattice parameters fit. The distortion in the MX plane is considered in the projected crystal structure drawing along the commensurate axis in figure 3.5 (b). Whenever the ratio of **a** and **a'** is irrational, the interface is called incommensurate and the lattice mismatch is defined as $1 + \delta$ with $\delta = 1 - \frac{a}{a'/2}$. While in that case **c** and **c'** can still be associated with each other, the presence of both an incommensurate and commensurate direction demands a description as given by [75], who introduce a (3 + 1)-dimensional superspace group to describe the misfit compounds including the modulations.

The misfit layered compounds were prepared the first time in 1970 but interestingly not immediately recognized as such [10] [11] [12]. The structure of the compound $(PbS)_{1.14}NbS_2$ that is dicussed in this thesis and the accompanying physical properties are described in the following two sections.

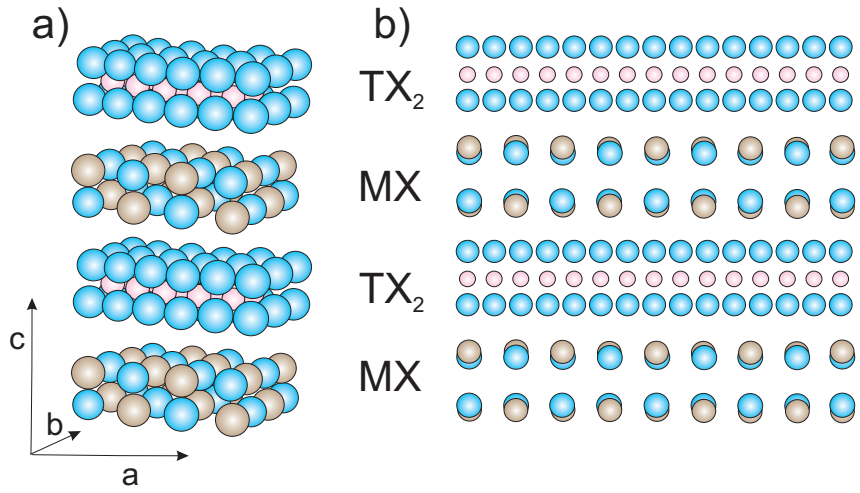

Figure 3.5: *(a) Schematic side view of the 3-dimensional structure of a misfit layered compound with the formula $(MX)_nTX_2$ ($n = 1.08....1.19$). The incommensurability direction is **a**, the layers are stacked along **c** direction. (b) The projected crystal structure along the commensurate direction **b** for the same compound.*

3.4 The crystal structure of $PbS_{1.14}NbS_2$ and its properties

The misfit layered compound $PbS_{1.14}NbS_2$ was first described in detail by Wiegers et al [13] who derived the crystal structure from x-ray data. The averaged lattice parameters can be measured very precisely with such methods and were determined to the values listed in table 3.1.

constituent	a_{misfit} (Å)	a_{pure} (Å)	b_{misfit} (Å)	b_{pure} (Å)	c_{misfit} (Å)	c_{pure} (Å)
NbS_2	3.313	3.31	5.801	5.73	23.80	11.89
PbS	5.834	5.936	5.801	5.936	11.90	5.936

Table 3.1: *Lattice constants of the misfit layered compound $PbS_{1.14}NbS_2$ [13] and the pure [7] constituents determined from x-ray data.*

Compared to the pure compound the lattice properties of the TMDC subsystem such as the hexagonal symmetry or the in-plane lattice constants appear to be nearly unaltered in any way, while the PbS is noticably modulated: The reason for that is easy to understand when one takes into account that the NbS_2 subsystem lacks any dangling bonds at the interfaces. Therefore no additional binding forces appear compared to the mere TMDC crystal. But for the double layers of PbS the binding forces have dramatically changed

compared to the galena bulk structure: With the abscence of the bulk the slabs hosted between two NbS_2 layers consist only of surface atoms with dangling bonds. The in-plane lattice constants are reduced (see table 3.1) from $a_{pure} = b_{pure} = 5.936$ Å to $a_{misfit} = 5.834$ Å and $b_{misfit} = 5.801$ Å to fit in the commensurate direction with the NbS_2 and thus the Pb atoms protrude out of the layer and the S atoms loom inside [9] approximately 0.25 Å each so that the total distance between them is increased to compensate the distortion. The changes within the PbS subsystem are in detail discussed in chapter 5.

Consequently the modulations in the crystal structure are described in such a way that the TMDC compound distorts the PbS guest lattice so that the in-plane parameters fit to each other. The spacing in c direction is on the other hand determined by the MC compound [75]. The distance between the Pb atoms and the sulphur of the TMDC varies due to the incommensurability, but is not smaller than about 1.8 Å. Thus an interlayer gap exists that is very similiar in size with that of the pure TMDC compounds [7]. This large separation between the layers supports the picture that the two-dimensional character of the misfit layered compound is conserved and the resulting system is an intercalated TMDC with its geometric probabilities being a mix of the two sublattices of which it consists of.

Figure 3.6 gives a detailed overview of the $(PbS)_{1.14}NbS_2$ lattice structure based on earlier x-ray diffraction data obtained by [13] from misfit crystals. The 3-dimensional sketch in the middle of the drawing shows the alternating PbS and NbS_2 sandwiches. The incommensurate [100] direction with the lattice constants $a_{PbS} = 5.834$ Å and $a_{NbS_2} = 3.313$ Å is indicated as "**a**"in the coordinate system for simplification, the same holds true for the commensurate [010] direction ("**b**") with $b_{PbS} = b_{NbS_2} = 5.801$ Å and the [001] direction ("**c**") perpendicular to the layers with $2 \cdot c_{PbS} = c_{NbS_2} = 23.80$ Å. The insets (a) - (f) show the detailed projected lattice structure in the zone axes as derived from the x-ray diffraction data [13]. The appropriate selected area electron diffraction patterns (EDPs) are shown here for comparison and are described in detail in chapter 5.

The projected top view along the [001] direction is constructed in (a): The distorted cubic structure of the PbS (indicated by the red squares) overlaps with the hexagonal NbS_2 (indicated by the red hexagon) structure and forms complex atomic arrangements. In **b** direction the lattice constants of PbS and NbS_2 are the same and thus commensurate. In **a** direction this is not the case, the ratio of a_{PbS} and a_{NbS_2} cannot be writen as a fraction of integers. As described above and in [75], one can nevertheless construct a supercell to deal with this problem and approximate the commensurability with $4 \cdot a_{PbS} = 7 \cdot a_{NbS_2}$. As a result one obtains the supercell that is indicated by the grey shaded box as a guide to the eye. The corresponding electron diffraction pattern is shown in (b): The hexagonal and cubic patterns can be easily identified and are highlighted by the red line. Weak spots in between the main reflections can be attributed to multiple diffraction with both subsystems involved.

The projected side view of the layers along the incommensurate direction is shown in c): Again the commensurability in **b** direction can be identified and the perpendicular stacking leads to the relationship of $2 \cdot c_{PbS} = c_{NbS_2}$. The signs denote here the atoms

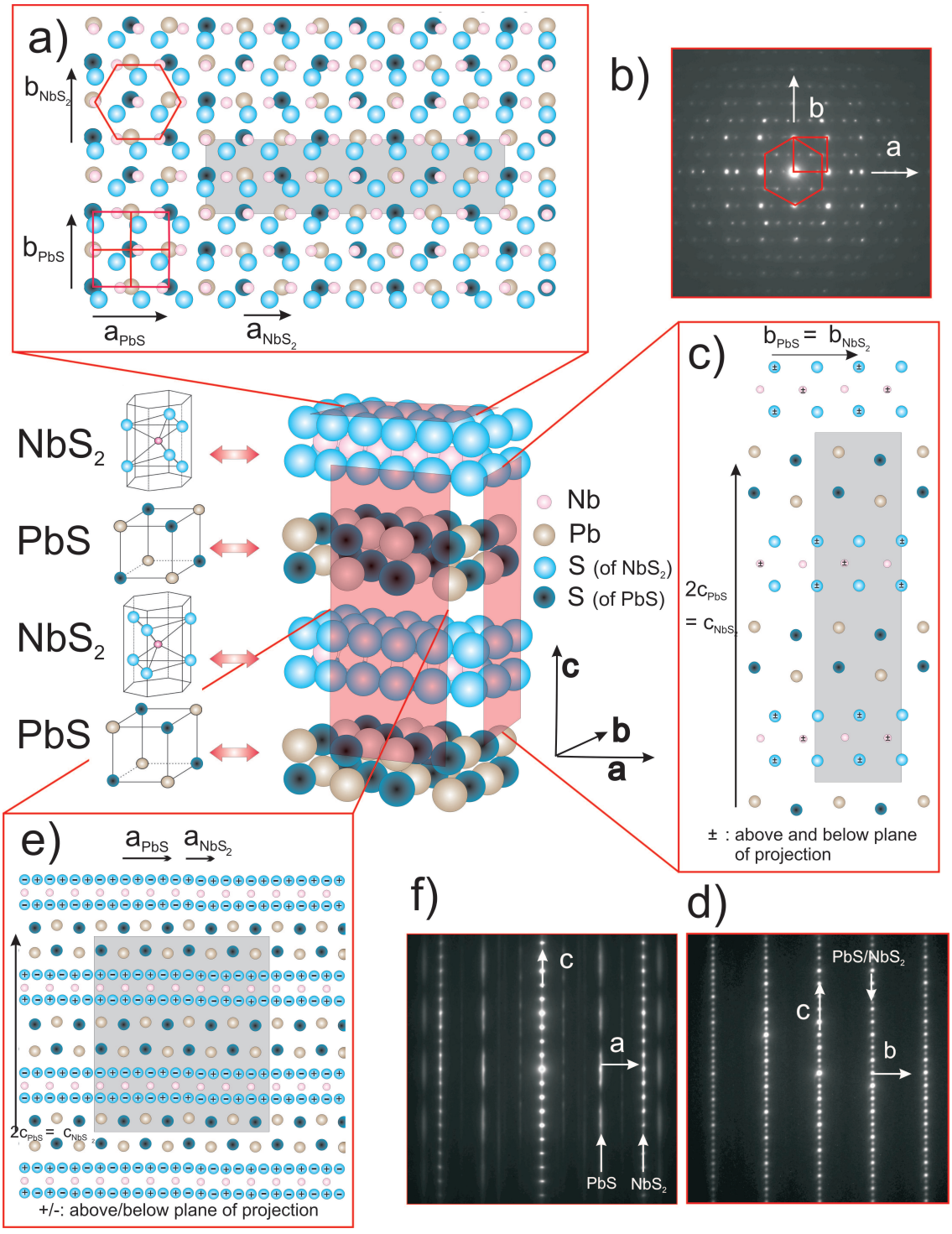

Figure 3.6: *Atomic configuration of the $(PbS)_{1.14}NbS_2$ misfit crystal derived from x-ray data [13]: In the middle the layered structure is schematicly shown with the unit cells of the single constituents to the left. The projected crystal structure is in detail shown as (a) top view (along [001] direction), (c) commensurate side view (along [100] direction) and (e) incommensurate front view (along [010] direction). The supercell of the structure for which the commensurability is approximated with $4a_{PbS} = 7a_{NbS_2}$ is indicated by grey-shaded areas. The electron diffraction patterns taken for this work in the appropriate zone axes are shown in (b), (d) and (f) and are in detail discussed in chapter 5.*

beeing above and below the plane of projection, the grey box shows the supercell of the combined misfit compound and the modulations of the PbS whose structure is no longer cubic are clearly visible in this projection. In the EDP the commensurability is mirrored by the parralel arrangements of spots with the same distance from the center in **b** direction for both subsystems.

Figure 3.6 (e) shows the projection of a single slab of the crystal structure parallel to the (010) plane with + and - indicating the site of the atom to be above or below the plane of projection respectively. The atomic configuration at the incommensurate interface direction with the x-ray derived lattice constants $a_{PbS} = 5.834$ Å and $a_{NbS_2} = 3.313$ Å is investigated in detail in this work. It gives rise to varying local inhomogeneities that are described in chapter 5, where aberration-corrected HRTEM investigations on the atomic arrangements at the interfaces are presented. Those investigations are indeed locally in contrast to the spatial averaging x-ray experiments. The $(4 \cdot a_{PbS} = 7 \cdot a_{NbS_2}) \times (2 \cdot c_{PbS} = c_{NbS_2})$ supercell is framed by the grey box.

The electron diffraction pattern (f) in the same zone axis is shown for comparison and is dominated by arrangements of spots parallel to the stacking direction indicating the layered structure. Due to the incommensurability the reflections corresponding to the PbS and NbS_2 subsystems are clearly separated from each other in the **a** direction. A remarkable feature is the streaking of the PbS reflections that will be explained by stacking disorder in detail in chapter 5.

The large number of reflections in all the EDPs prove the broad variety of spacial frequencies transferred during imaging that contribute to the electron diffraction. For such a complex crystal structure this behaviour is expected.

Chapter 4

Experimental

4.1 Crystal growth and sample preparation

The single crystals were grown using the chemical vapor transport (CVT) method that will be explained in the next section. One of the biggest challenges of using high-resolution transmission electron microscopy is the preparation of samples that are both very thin and also without any major damage from the ion beam used for thinning that destroys or alters the crystal structure. In the context of aberration-corrected TEM instruments, *thin* means about 10 nm or less in the region of interest. Additionally, amorphous material on top of the sample from the thinning process blurrs on the one hand the contrast of HRTEM images, but is on the other side necessary to line-up the C_s corrector of the microscope.

The techniques that were applied and improved for the samples examined in this study will also be discussed in this chapter.

4.1.1 Chemical vapor transport

The misfit layered compound crystals used in this thesis were fabricated by the surface science group of Prof. Dr. Kipp from the Institute of Experimental and Applied Physics of the Christian-Albrechts University Kiel [76] during a collaboration supported by the German Research Foundation [18].

The system investigated in this thesis is fabricated by the standard technique to grow transition metal dichalcogenide crystals - the chemical vapor transport method as shown in figure 4.1.

The pure compounds with a stoichiometric initial weight are introduced into a quartz vial with iodine I_2 as a transport agent. After evacuation the vial becomes sealed and is inserted into a so called four-zone furnace. The basic principle of such an oven comprises of a temperature gradient of about 100 - 150 °C between the high temperaure nourishing zone and the low temperature growth area at absolute temperatures ranging typically from 700°C - 800°C and 900°C - 1000°C. Under these conditions the crystal growth takes approximately 4 - 6 weeks.

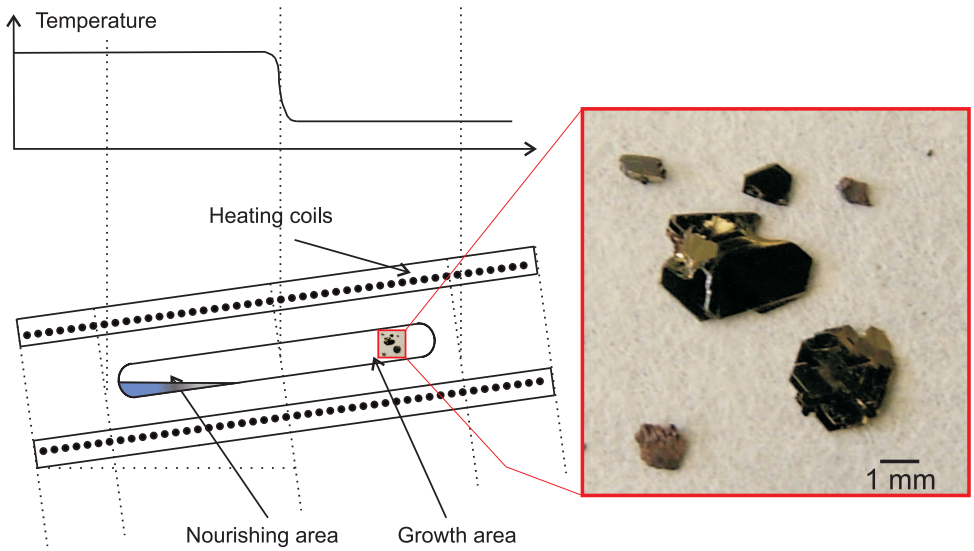

Figure 4.1: *Schematic drawing of a four-zone furnace that is used for the crystal growth by chemical vapour transport. The initial weight of pure constituents is on the high temperature side (left) of the vial (see also temperature diagram, schematically), the growth area where the final crystals form in the low temperature regime on the right. Gaseous iodine is used as transport agent. The inset shows a typical misfit compound crystal after the growth is finished.*

The resulting crystals have typically the size of 5 mm × 5 mm × 0.1 mm or smaller. A photograph of such a misfit crystal is shown in the inset of the figure 4.1. The flat crystals have often sharp edges but are sometimes also round shaped. They look glossy and have an optically clean and reflecting surface.

Even though it has to be stated that the nature of the reactions during the growth are only rudimentarily understood, the general chemical formula for producing TMDCs by CVT is

$$TI_4 + 2X \rightleftharpoons TX_2 + 2I_2, \tag{4.1}$$

where T is the transition metal and X the chalcogen. Similarly, this is expanded for misfit layered compounds by [77] with the following reaction scheme:

$$TI_4 + (3+x)X + (1+x)MI_2 \rightleftharpoons (MX)_{1+x}TX_2 + (3+x)I_2, \tag{4.2}$$

with M = Pb in the case of $(PbS)_{1.14}NbS_2$ and x = 1.14.

Additionally it is interesting to notice that according to Brandt and co-workers [76] who have grown the crystals used in this work, it was not possible to grow misfit compounds consisting of semiconductor TMDC compounds. Although the successful growth of $HfPbS_2$ is reported in [78], this systems has a completely different crystallographic structure than the misfit layered compounds.

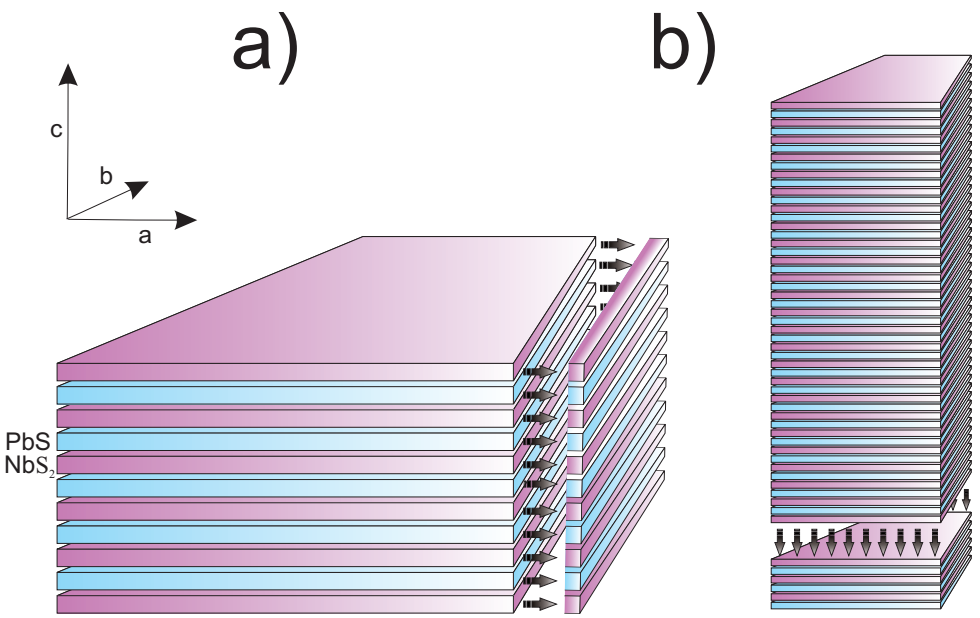

Figure 4.2: *Illustration of the different sample preparation approaches for layered materials like TMDC misfit compounds: For cross section samples (a) one cuts and thins perpendicular to the layers while for plan-view specimen (b) the thin film is prepared by cutting the crystal parallel to the sandwich layer interfaces along the van-der-Waals gap. This can be achieved by different cleavage techniques.*

4.1.2 Preparation of ultra-thin samples for HRTEM

The preparation of samples for high-resolution transmission electron microscopy from the misfit layered compound crystals can be generally parted into two totally different techniques, i.e. the plan-view and the cross-section preparation. While for normal 3-dimensional bulk specimen the fabrication for plan-view and cross-section samples differs not much, the quasi 2-dimensional nature of the TMDC misfit compounds with its stacked geometry of sandwiches separated by van-der-Waals gaps along the (001)-axis forces the preparator to apply different techniques for cross section and plan view preparation. The initial situation is sketched in figure 4.2: For cross-section preparation one has to achieve parallel cuts towards the **c** direction perpendicular to (or in a certain angle against, if desired) the layers, but for plan-view samples the crystal has to be thinned parallel to the layered structure itself. Two approaches are described in the following sections.

Preparation of cross-section HRTEM specimens

The cross-section preparation follows some well known techniques often used for TEM specimen fabrication combined with some remarkable specifics that arise from the physical nature of the TMDC misfit compounds. After opening a vial from the crystal furnace one first has to wait for some days until the iodine that was used as transport agent

during the growth process is evaporated, in order to avoid outgassing in the vacuum of the microscope column.

The crystals can differ in shape and size, dependent on the growth parameters. For TEM samples one usually wants the crystal to be flat, with a clean surface and not smaller than approximately 2 mm × 2 mm so that it can still be handled with a forceps.

Figure 4.3 illustrates the main steps of cross-section sample preparation.

The $(PbS)_{1.14}NbS_2$ crystals show a beneficial feature at its surfaces that is visible even by the eye: Small parallel lines similar to scratches can be observed which point along the crystallographic direction with the commensurate interfaces. This is a helpful guide to cut the crystal in such a way, that the interface which one is interested in can be observed in the microscope under feasible tilt angles. Therefore the crystal is then glued between silicon wafers and glass so that the surface on one side is still visible (figure 4.3 (a)).

After that a wire saw is used to cut the sample into slabs of approximately 1 mm thickness (b), followed by ultrasonic drilling (c) to cut a disc with a standard diameter for TEM specimen holders. Mechanical thinning is then done with rotating specimen disc grinders using abrasive paper with decreasing granularity to polish the surface.Then a dimple grinder (d) is used to thin the specimen selectively in its center down to $\sim 30\ \mu m$.

During the subsequent ion etching (e) accelerated Argon ions emitted from one or two guns are used to thin the specimen further until a hole appears. At the edges of the hole the specimen should finally be both, thin enough for high-resolution electron microscopes and as "clean"as possible. Amorphous layers on the surfaces of the thin TEM specimens are the result of ion beam damage during Ar ion milling and the thickness of these layers should be minimized for a good signal-to-noise ratio in HRTEM images of atomic columns, as the ones presented in chapter 5. To achieve this, one can tune several critical parameters that are the ion energy, the gun current and the thinning angle.

For the sample prepared during this thesis different ion polishing machines were used. The preparation lab in Kiel hosts the GATAN PIPS Model 691 (operation voltage 1 - 6 kV, source current 1.0 mA, milling angle 0° - 10°) and the BALTEC RES 100 (operation voltage 1 - 10 kV, source current 0.5 - 3.5 mA, milling angle 0° - 18°). Additionally during the experiments in Jülich at the Ernst Ruska-Centre the TECHNOORG LINDA Gentle Mill (operation voltage 0.1 - 2 kV, source current 7 - 90 μA, milling angle 0° - 45°) was used for post-thinning. A HRTEM sample that has undergone all these processes successfully is photographed under a light microscope in figure 4.4.

Problems that may arise during HRTEM sample preparation are that the TMDC misfit compounds are very sensitive when mechanic forces are applied and often don't survive the grinding and dimpling process. Even after ion polishing the samples can comprise a lot of amorphous material that sometimes cannot be removed by further thinning under different conditions.

One also has to take into account that due to the sandwich structure the ion polishing can destroy or at least disturb or modulate the layers to a certain degree. This is the main reason why ion etching can not be applied in the case of plan view sample preparation.

For future work on this materials it could be reasonable to study the ion thinning on the samples in more detail as a function of the relevant parameters (ion energy, gun

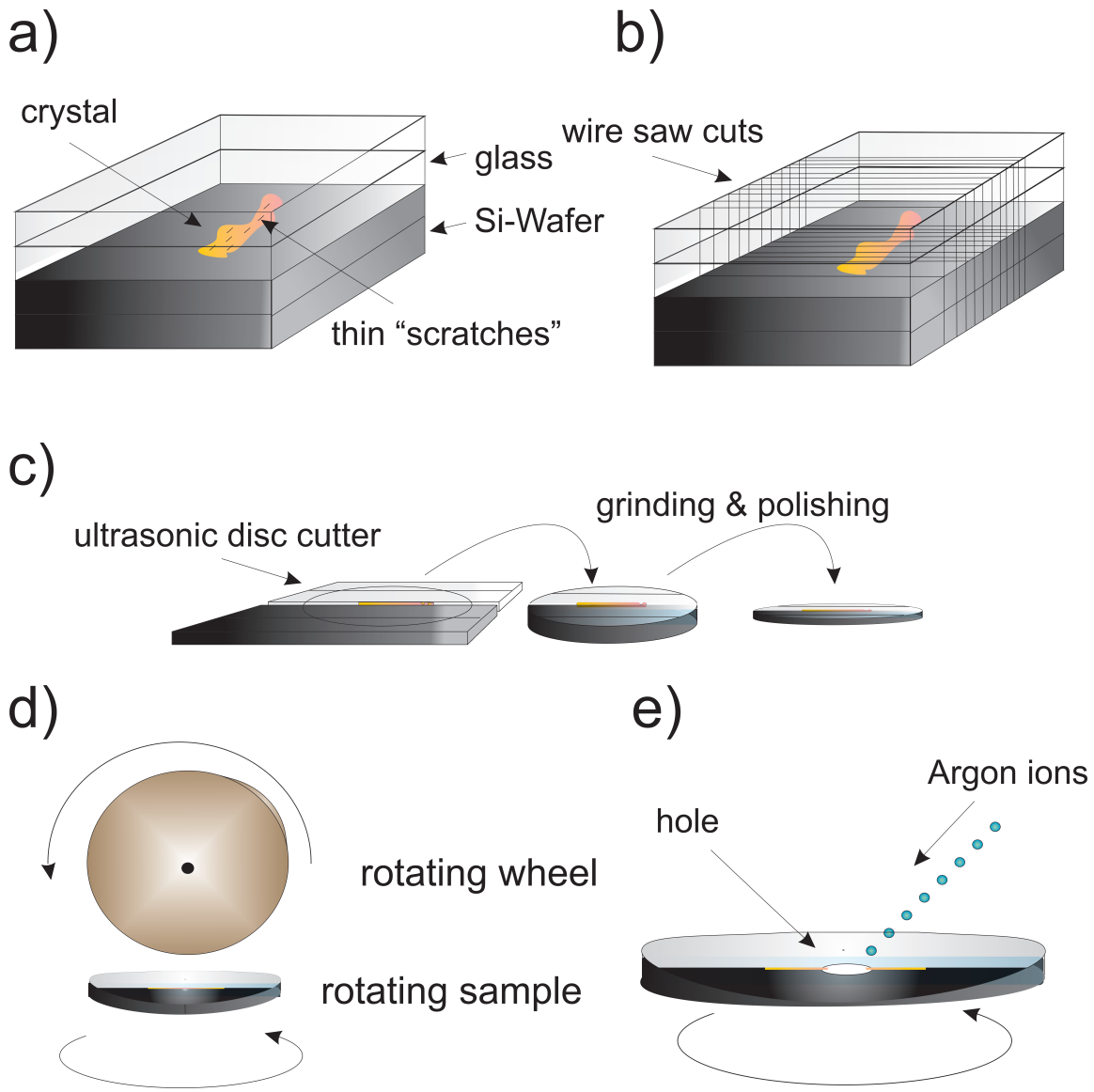

Figure 4.3: *Demonstration of the basic steps of preparing a cross section sample from a misfit layered compound crystal: (a) The crystal is glued between silicon wafers and glass in the preferred orientation and then (b) cut into slabs of about 1 mm thickness by a wire saw. With an ultrasonic disc cutter (c) the round shape with standardized diameter for the specimen holders of the microsope is achieved and the sample is further thinned by grinding and polishing on special rotating abrasive paper. Dimpling (d) is performed by mounting the sample to a rotating table and by a rotating wheel in contact with the surface. This specimen with less than 30 µm thickness is used for the final step of Ar ion etching (e) which is applied until a hole with electron-transparent edge regions is formed.*

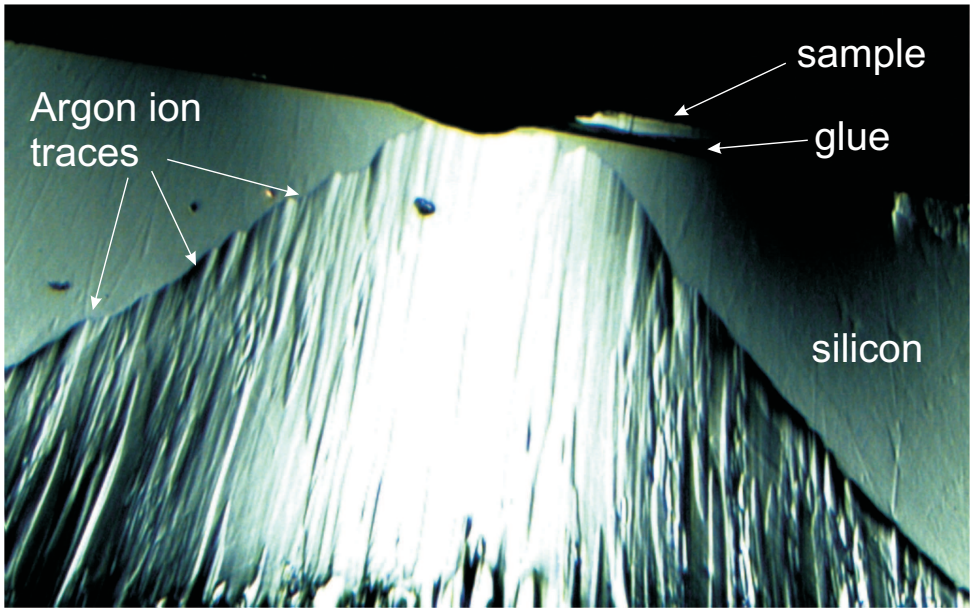

Figure 4.4: $(PbS)_{1.14}NbS_2$ *sample after succesful cross section preparation for high-resolution transmission electron microscopy.*

current, thinning angle) in detail to optimize this impotant step.

Nevertheless successful HRTEM sample preparation was achieved during this work as the aberration-corrected HRTEM images (e.g. figure 5.8) in chapter 5 demonstrate.

Preparation of plan-view HRTEM specimens

The sandwich crystals of the TMDC misfit compounds prohibit plan-view sample preparation as described above due to it's quasi 2-dimensional geometry. Fortunately another method exists to reach the goal of clean and thin samples in plan view which uses the layered structure as an advantage as shown in figure 4.5.

First the crystal is glued to a wafer and then an adhesive tape is attached to the upper surface. Now the tape is removed carefully (figure 4.5 (a)) and the compound becomes cleaved just along a van-der-Waals gap. This technique is adopted from surface science laboratories where similar methods are used in order to produce defect free surfaces under ultra-high vacuum conditions. The in-plane stability of the misfit layered compounds due to its quasi 2-dimensional nature supports this approach.

The preparator then carefully cuts off very thin facets from the brink with a razor blade under a light microscope and puts the small pieces onto appropriate mesh grids of copper (figure 4.5 (b)). At the edges of the small facets one finds regions under the electron microscope where the sample is thin enough for investigations.

This method is faster than the average cross section preparation procedure, in fact one can easily prepare a dozen samples within one day. While this technique avoids

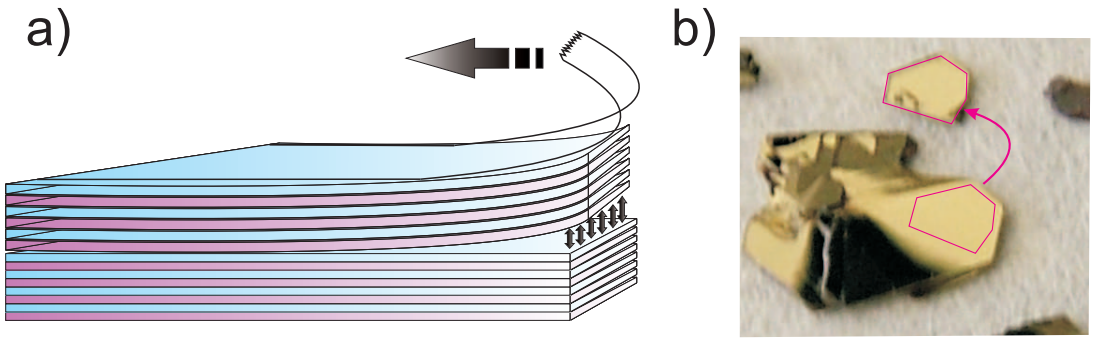

Figure 4.5: *Plan-view preparation of TMDC misfit compound samples for high-resolution electron microscopy: (a) The sample is cleaved along the van-der-Waals gaps by gluing an adhesive tape to the crystal and pulling it up. (b) Subsequently, small facets on the edges of the clean surface can be lifted with a razor blade and brought into an appropriate copper grid.*

damage from ion beams and mechanical thinning, there are also disadvantages: First, not all samples that appear to be thin under the light microscope can be used for HRTEM because they are still far too thick for inspecting them in the HRTEM. That can be compensated only by producing a lot of samples. Secondly by the cutting with the razor blade the edges of the sample tend to bow upwards, which aggravates the correct adjustment of the incident beam direction in the electron microscope. Finally with this method amorphous material is avoided, because the crystal structure is not destroyed by an ion etching step. On the other hand a narrow amorphous edge is required to line-up the C_s-corrector (compare chapter 4.3).

It is possible to put an amorphous sample together with the misfit into the grid for the corrector adjustment. This is not a very good solution because after re-adjusting for the different sample height the corrector settings will not be adequate any more. Focussing the beam and "burning"the sample to get amorphous horns is still the best way to circumvent this problem but of course not entirely satisfactory.

4.2 Conventional HRTEM & STEM

Conventional HRTEM and STEM was performed with the recently installed Tecnai F 30 S-Twin microscope in the Nanolab Kiel. At the time of the experiments not all microcope parameters were carefully characterized so there are some uncertainties in that. Imaging had to be done with the GIF camera, as a CCD camera in front of the GIF was not yet available.

Nominal parameters for the microscope operated under 300 kV are:

- defocus spread $\delta(Z) = 5.3$ nm,
- spherical aberration coefficient $C_s = 1.2$ mm,

- Scherzer defocus Z = -59 nm.

The semiconvergence angle for typical illumination conditions is $\alpha = 0.3$ mrad.

Recording focal series with the conventional Tecnai F 30 microscope was also performed for this thesis. The series are recorded in equidistant focal steps around Scherzer or Lichte defocus. Although there is no quantitative knowledge about other aberrations apart from the value of the C_s, computational focal series reconstruction on images taken with the Tecnai are performed.

The STEM images were among the first ones ever taken with this instrument after installation. STEM HAADF imaging has been performed in order to investigate its potential in imaging the columns of heavy atoms in the misfit compound. Parameter settings used for the image acquisition are condensor aperture 100 μm, spot size 9 and gun lens 6. Further improvements in resolution are achievable by optimizing the system parameters.

4.3 Aberration-corrected HRTEM

Aberration-corrected high-resolution transmission electron microscopy (HRTEM) was applied to resolve the atomic structure of the misfit layered compound $(PbS)_{1.14}NbS_2$. The measurements were done at the Ernst Ruska-Centre in the research center Jülich using a FEI TITAN 80-300 kV HRTEM equipped with an imaging aberration corrector element. While it is possible to go to lower values, the operational voltage was always set to 300 kV during the experiments. A Gatan 2k slow scan charged coupled device camera (CCD) system was used. Specifications for the instrument operated under optimum conditions are determined to:

- defocus spread $\delta(Z) = 2.93$ nm,
- semiconvergence angle $\alpha = 0.2$ mrad,
- information limit $1/g_{max} = 0.8$ $\mathring{A}$,
- residual delocalisation $R = 0.47$ $\mathring{A}$,
- optimum spherical aberration $C_{s,opt} = -12.72$ μm,
- optimum focus $Z_{opt} = 5.78$ nm,
- optimum focal increment $d = 2.44$ nm,
- chromatic aberration coefficient $C_C = 1.28$ nm.

The accompanying image simulations where performed with the JEMS software package provided by Stadelmann and co-workers [20] using the multislice algorithm already described in chapter 2.1.2.

As explained in detail in section 2.1.7., in the ideal case a focal series of about 10 or more images with equidistant focal steps is recorded to reconstruct the exit plane wavefunction. For an aberration corrector equipped instrument residual aberrations determined right before the image aquisition can be corrected and phase and amplitude can be generated. From that, structure information like lattice parameters can be gained by evaluating intensity peak distances. For that purpose it is important to know the CCD camera discretization very precisely for the magnification that is used. For the images recorded during this work that are used in the present and following sections, usually a magnification of 790k or 1000k was used. Table 4.1 lists the discretization values for some magnifications of the Titan microscope operated under 300 kV [79]. The determination of atom column distances is of course also limited by these errors.

Imaging mode	mean sampling (nm/pixel)	relative error (%)
SA 490k	0.021793	0.339
SA 620k	0.017124	0.365
MH 790k	0.012826	0.287
MH 1000k	0.010243	0.227
MH 1200k	0.008239	0.252

Table 4.1: *Calibration results for the CCD image discretization of imaging modes within the aberration corrected FEI Titan microscope operated at 300 kV [79].*

When recording a focal series within an aberration-corrected microscope, the defocus values are chosen in such a way, that the NCSI contrast producing defocus is located somewhere in the middle of a series of images . When the sample is very sensitive to beam damage it can however be favourable to adjust the defocus in such a way that the NCSI contrast is among the first few images of the series. The experimental procedure usually starts with the alignment of the aberration corrector. For that purpose it is common to search for a position on the sample that is very thin and consists in the best case exclusively of amorphous material, which is often the case at the edges of the specimen. Now a so-called tilt series is recorded, where the angle of the incident beam is tilted isotropically around its center and the power spectrum for each angle is recorded to calculate the phase plate [80] and determine the quantities of the lower order aberrations, in particular defocus, 2-, 3-, and 4-fold astigmatism, axial coma, spherical aberration, star aberration and three lobe aberration. Those should be corrected sufficiently according to table 4.2 [81] to match the $\pi/4$ limit (as explained in chapter 2.1.7) for the information limit $g_{max} = 12.5\ \mathrm{nm}^{-1}$ of the microscope.

An examplary tilt series from an amorphous edge of a $(PbS)_{1.14}NbS_2$ sample is shown in figure 4.6 together with the phase plates for the aberrations which give the quantity of each aberration coefficient. The concentric placement of the diffractograms in 4.6 (a) represents schematically the angles by which the appropriate spectrum is taken. This

Coefficient	ATLAS notation	Aberration synonym	Quantity
Z, C_1	c_{20}	defocus	0.8 nm
A_1	c_{22}	2-fold astigmatism	0.8 nm
b_2	c_{31}	axial coma	17 nm
A_2	c_{33}	3-fold astigmatism	50 nm
C_3, C_s	c_{40}	spherical aberration	-12.72 $\mu m \pm 2.7 \mu m$
S_3	c_{42}	star aberration	0.67 μm
A_3	c_{44}	4-fold astigmatism	2.7 μm
B_4	c_{51}	axial coma 5th order	27 μm
D_4	c_{53}	three lobe aberration	27 μm
A_4	c_{55}	5-fold astigmatism	136 μm
C_5	c_{60}	spherical aberration 6th order	6.6 mm
S_5	c_{62}	star aberration 6th order	-
S_5	c_{64}	rosette aberration	-
A_5	c_{66}	6-fold astigmatism	6.6 mm

Table 4.2: *Allowed magnitudes of aberration coefficients ($\pi/4$ limit for $g_{max} = 12.5\ nm^{-1}$ at 300 kV) [81]. The coefficient notations differ for the ATLAS software and are listed here for the respective aberrations.*

is called *Zemlin tableau*. The phase plate denoted "all"in (c) is the effective one that is formed from the distributions of all lower order aberrations. Those phase plates from each individual aberrations are denoted by c_{xx}, with the ATLAS notation from table 4.2. The tableaus are recorded and evaluated with the ATLAS software developed at the Ernst Ruska Centre Jülich [81].

During the experiment a tilt series is first recorded to correct the aberrations according to the $\pi/4$ limit, then the focal series is recorded and then again a tilt series is acquired. If the aberrations estimated from both tilt series before and after the experiment differ only slightly, the experimentator can in good approximation assume that those quantities where stable enough in time to treat the aberrations as constant values during focal series acquisition. The values gained from the evaluation of the Zemlin tableau can later be used for computational correction of the aberrations [82]. However, it should be noted that especially the 2-fold astigmatism is indeed not stable even over short time periods [83].

4.4 Electron diffraction

For lattice parameter and structure determinations one uses the electron diffraction mode within a TEM and can then compare these data to x-ray diffraction experiments and judge about the structure properties of the sample. The lattice parameters from the x-ray data

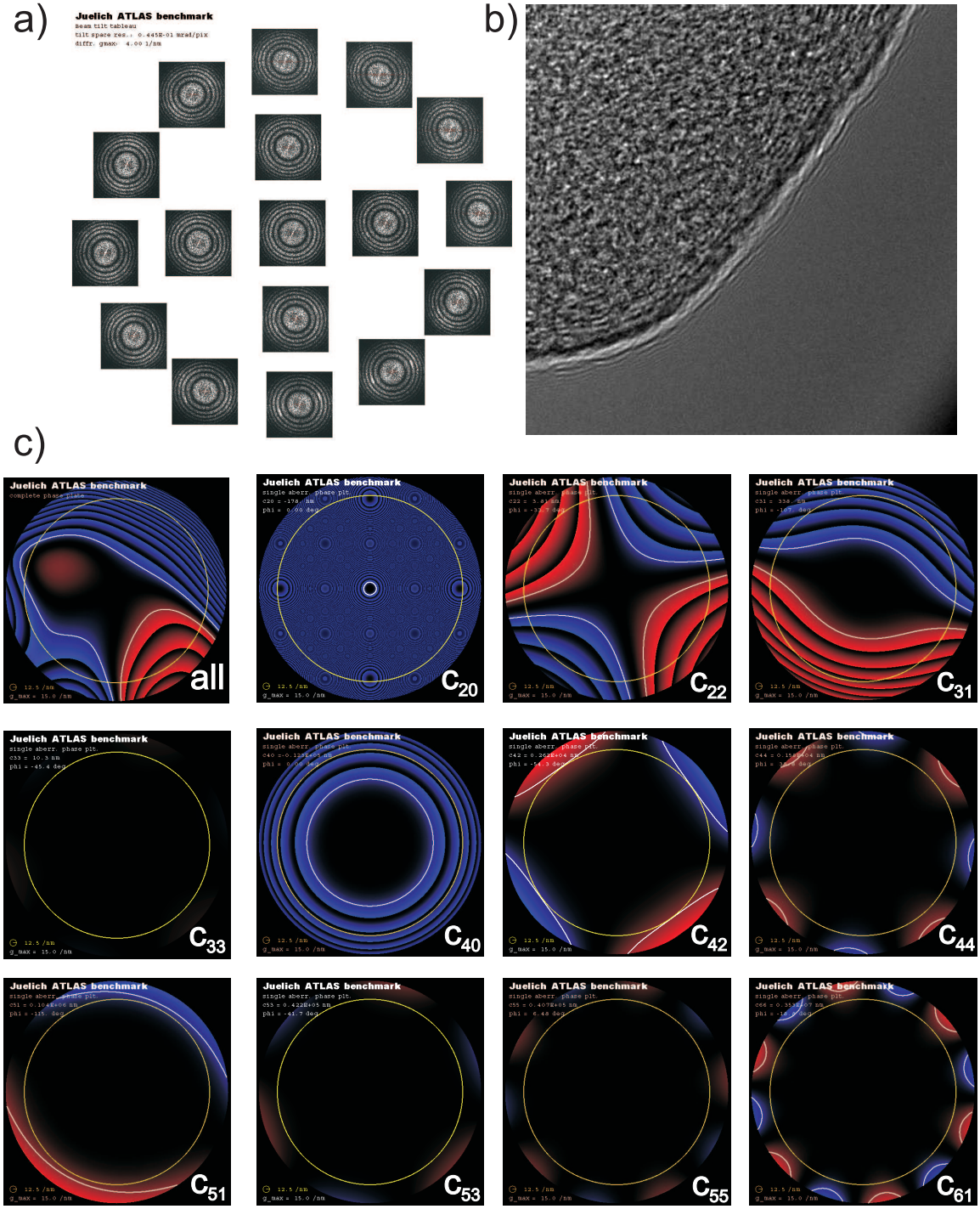

Figure 4.6: *Tilt series from a $(PbS)_{1.14}NbS_2$ sample at an amorphous edge (b). The Zemlin tableau (a) shows the diffractograms recorded under tilted incident beam angles that are used to calculate the quantities and phase plates of the lower order aberrations (c_{xx}, ATLAS notation) in (c). The tableaus are recorded and evaluated with the ATLAS software developed at the Ernst Ruska Centre Jülich [81].*

for the pure [7] and the misfit [13] compounds were already listed in table 3.1. The errors of those values are according to the authors in the range of 0.1 - 0.2 pm, i.e. about 0.02 %. This accuracy cannot be reached by any other experimental technique. For electron diffraction within a TEM, the discretization of the CCD camera (i.e. the sampling rate in nm per pixel) is usually estimated with the help of polycrystalline samples in the diffraction mode. If this is done very precisely, the error can be reduced to a residual inherent bias of about 2 % ($\approx$ 12 pm for the misfit compound lattice parameters), which is still two orders of magnitude higher than the error inherent in the x-ray scattering data. Using convergent beam electron diffraction, an accuracy of 0.01 % is possible, but due to the high density of reflections in the electron diffraction pattern of misfit compounds this is not applicable here.

Usually, if one has not checked the calibration for every camera length and parameter settings of the microscope used during the experiment (e.g. by inserting a standard together with the sample in a grid), an error of up to 5 % has to be taken into account [79]. However, that is sufficient enough for many practical purposes as e.g. for accurately determining lattice parameters and the crystal structure of the sample.

4.5 Comparison of conventional and aberration-corrected HRTEM imaging

The advantages of aberration-corrected HRTEM and the NCSI imaging mode, that suppresses the image delocalization strongly and shows at the same time favourable contrast transfer (figure 2.5) was already discussed in detail in section 2.1.6. The goal of this work was to achieve NCSI contrast images that directly show the atom columns at the incommensurate interfaces of the misfit layered compound $(PbS)_{1.14}NbS_2$.

When the parameters of the microscope during the imaging process are well known, it is possible to also simulate these conditions with the multislice approach discussed in section 2.1.2 and compare the image contrasts. When the intensity distribution from both the experimental and the simulated images fit together, it is in good agreement with the theory justifiable to identify the intensity peaks with the projected crystal potential and thus the atom columns.

Without aberration correctors this is not possible, as figure 4.7 points out: The image delocalization $R(g)$ for Scherzer (red curve) and Lichte (light red curve) defocus of a conventional Tecnai F30 instrument is compared with the one under NCSI conditions (blue line) in an aberration-corrected Titan. $R(g)$ produces large quantities for any spatial frequency range of g where the contrast transfer function (as shown in figure 2.5) oscillates strongly. For conventional Scherzer defocus the delocalization is relatively small for spatial frequencies lower than the point resolution that is given by the first root of the corresponding CTF but increases dramatically for higher values of g. The Lichte defocus minimizes the total delocalization but shows huge values of $R(g)$ for lower frequencies. For both imaging conditions, contrast delocalization within the order of some nm occurs over large parts of the spatial frequency range.

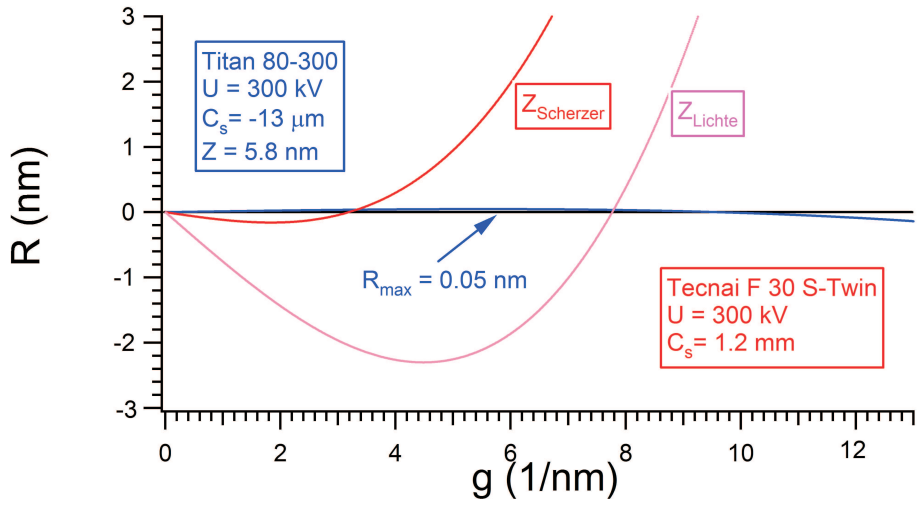

Figure 4.7: *Image contrast delocalization behaviour $R(g)$ for Scherzer (red curve) and Lichte (light red curve) defocus of a conventional Tecnai F30 instrument compared with the one under NCSI conditions (blue line) in an aberration-corrected HRTEM. While both Scherzer and Lichte conditions produce contrast delocalization of about some nm for large ranges of the spacial frequency g, the delocalization for NCSI conditions remains under the value of* $0.5\mathring{A}$ *up to the information limit and is therefore highly preferable for desired resolutions that are in the order of typical atom column distances within a crystal like the* $(PbS)_{1.14}NbS_2$.

In contrary to that, in an aberration-corrected HRTEM under NCSI conditions the delocalization is suppressed clearly under 0.05 nm for all spatial frequencies up to the information limit. This allows the assumption that atom columns of even complex systems like the misfit layered compounds can be directly imaged if samples are sufficiently thin.

This behaviour can be directly demonstrated as figure 4.8 illustrates [84]: Here a single supercell (as shown schematically in the inset) of the $(PbS)_{1.14}NbS_2$ system is artificially embedded in vacuum and the HRTEM image contrast is simulated with multislice algorithms for different sets of microscope parameters. (a) shows the effects of contrast delocalization for a conventional HRTEM under Scherzer defocus (Tecnai F 30) and (b) the corresponding NCSI contrast by an aberration-corrected instrument (Titan). It becomes obvious, that the delocalization effects that transfer intensity far into the vacuum (a) are also present inside the unit cell and make a direct interpretation of the intensity impossible if compared to the real structure. In contrast, for the case of the NSCI condition image the delocalization effects are only slightly visible at the edges of the supercell and the intensity can be easily identified with the projected potential and thus the atom columns of the compound.

Indeed, by varying imaging parameters like defocus or the crystal thickness, for a conventional HRTEM and very complex systems like the misfit layered compounds it is

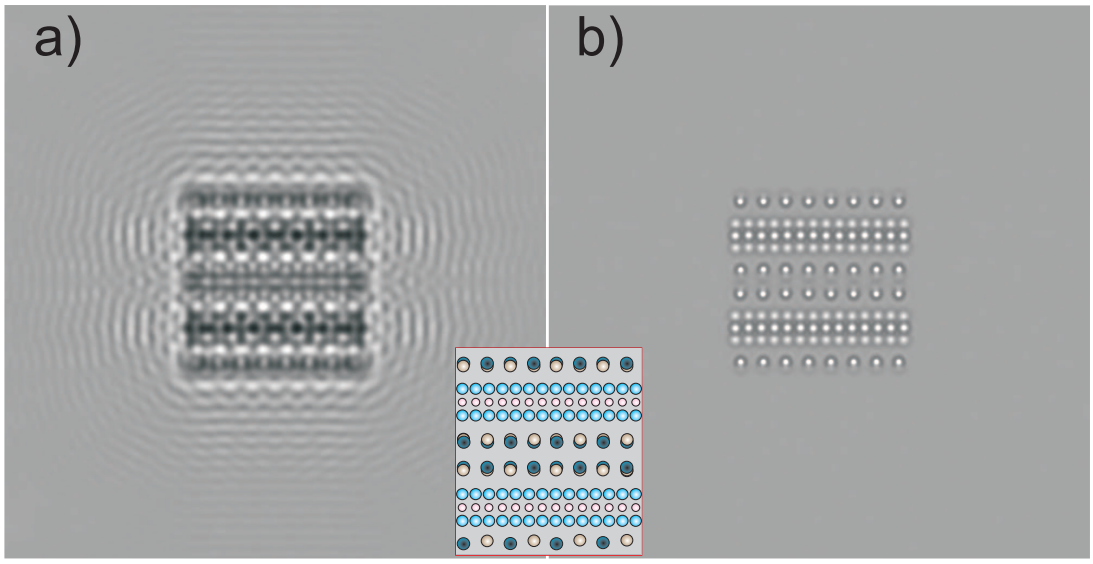

Figure 4.8: *Multislice simulations to demonstrate the effect of delocalization on imaging for a conventional (a) Tecnai F 30 and an aberration-corrected Titan HRTEM (b): A single unit cell of* $(PbS)_{1.14}NbS_2$ *(schematically shown in the inset) is embedded in vacuum. (a) For Scherzer conditions (U = 300 kV,* C_s *= 1.2 mm, Z = -59 nm) complicated contrast does not allow to direcly link the intensity peaks to the atomic structure. The delocalization "swaps"intensity far into the vacuum, which of course also dominates the contrast within the unit cell. For NCSI conditions (U = 300 kV,* C_s *= - 13 µm, Z = 5.8 nm) a direct interpretation of the image intensity with respect to the projected potential and thus the atom columns is possible.*

not possible to achieve image intensities that allow a direct interpretation of the underlying crystal structure. For very simple crystals like Silicon in e.g. <110> projection this can be possible [85], but for such complex structures like the misfit layered compounds the image delocalization and complicated contrast transfer in a conventional HRTEM are clearly inferior to the properties under NCSI conditions in an aberration-corrected HRTEM as the simulations presented in figure 4.8 demonstrate.

After image acquisition, the experimental data are compared with the image intensities simulated for the appropriate microscope parameters. When the experimental and simulated contrasts are comparable for the simulation parameters used during image acquisition (i.e. accelerating voltage, spherical aberration, defocus, defocus spread, semi-convergence angle, sample thickness), the recorded intensities are in fact the direct representations of the atom columns and thus the lattice structure can be studied locally in real space.

Chapter 5

The structure of $(PbS)_{1.14}NbS_2$: Experimental data and image simulations

This chapter presents first the geometric structure of the crystal system estimated from electron diffraction patterns compared with x-ray diffraction experiments. Afterwards the results from the STEM and aberration-corrected HRTEM plan-view imaging are presented, followed by a comparison of conventional and aberration-corrected HRTEM imaging and focal series reconstruction. Direct real space results obtained from the aberration-corrected HRTEM images showing several local inhomogeneities will be presented afterwards. Those micrographs demonstrate the powerful NCSI technique, that allows to directly measure lattice parameters and related atomic structure features.

5.1 Lattice parameters and commensurability: Electron diffraction study

Obviously it is important to characterize the lattice structure of a crystal system prior to any further examinations in the TEM, especially if one deals with such complex structures like the misfit layered compounds. The CVT growth process for those compounds as explained in chapter 4 is until now not very well understood. Concerning this, it should be clear that an uncertainty about the stoichiometry and even the whole lattice structure of the crystals will always remain after growth. While the macroscopic quality of the samples can be judged under a light microscope or even by eye to find out whether the crystals can be used to prepare TEM cross-section or plan-view samples, it is further necessary to determine the lattice parameters to be sure that the system is indeed the one which it is expected to be. For example, in the case of the misfit layered compounds the crystallization can take place in the related but not identical 1T, 2H or 3R structures. By very precisely prompting the initial weight into the vile before the growth one minimizes such unwanted results, but still a residual uncertainty about the final structure remains.

5.1.1 Lattice projection along the [001] axis of $(PbS)_{1.14}NbS_2$

Figure 5.1 (a) shows the projected crystal structure of a single slab of the $(PbS)_{1.14}NbS_2$ compound viewed along the [001] direction determined from the x-ray derived lattice parameters given in the table (b), that also lists the values from the pure compounds. In this direction the slight modulation effects that change the lattice parameters are rather small.

The nearly fourfold symmetry of the PbS sublattice is indicated by the red rectangles in the bottom left corner of (a), the sixfold symmetry of the NbS_2 is highlighted by the hexagon. Along the **b** direction the lattice parameter is the same for both sublattices which defines the size of the grey painted supercell in that direction. Along the incommensurate **a** direction the supercell is constructed by approximating the ratio to $7 \cdot a_{NbS_2} = 4 \cdot a_{PbS}$ as will be described in more detail in the previous sections.

From the electron diffraction pattern in (c) the lattice constants can be calculated by measuring the spot distances. The table 5.1 lists the x-ray derived lattice constants from [13] and the ones determined from the electron diffraction patterns in the [100], [010] and [001] zone axes for the samples used in this thesis. From these values two conclusions can be made: First, we can be confident that our sample structure corresponds to that described in the literature and thus we have the same crystal structure. Second, the mean values of the electron diffraction determined lattice parameters are very close to the x-ray values, which means that the calibration might be far better then the assumed error of 5 %.

lattice constant	x-ray	electron diffraction
a_{PbS} (Å)	5.834 ± 0.002	5.79 ± 0.29
a_{NbS_2} (Å)	3.313 ± 0.001	3.32 ± 0.17
b_{PbS} (Å)	5.801 ± 0.001	5.74 ± 0.29
b_{NbS_2} (Å)	5.801 ± 0.001	5.74 ± 0.29
c_{PbS} (Å)	11.902 ± 0.003	12.14 ± 0.6
c_{NbS_2} (Å)	23.807 ± 0.001	24.23 ± 1.2

Table 5.1: *Lattice constants of the $PbS_{1.14}NbS_2$ misfit derived from x-ray data [13] and electron diffraction patterns.*

The [001] diffraction pattern in figure 5.1 (c) is partly indexed for clarification and red lines are inserted as a guide to the eye to highlight the NbS_2 and PbS originating reflections. The commensurate direction **b** is easy to identify, as the (020) reflection is in the same distance from the center of the pattern for both subsystems. In contrary to that, along the **a** direction this is clearly not the case. The indexing is done in a way that treats the misfit compound as being build up by two independent subsystems, and therefore the reflections have indices denoting the lattice they correspond to.

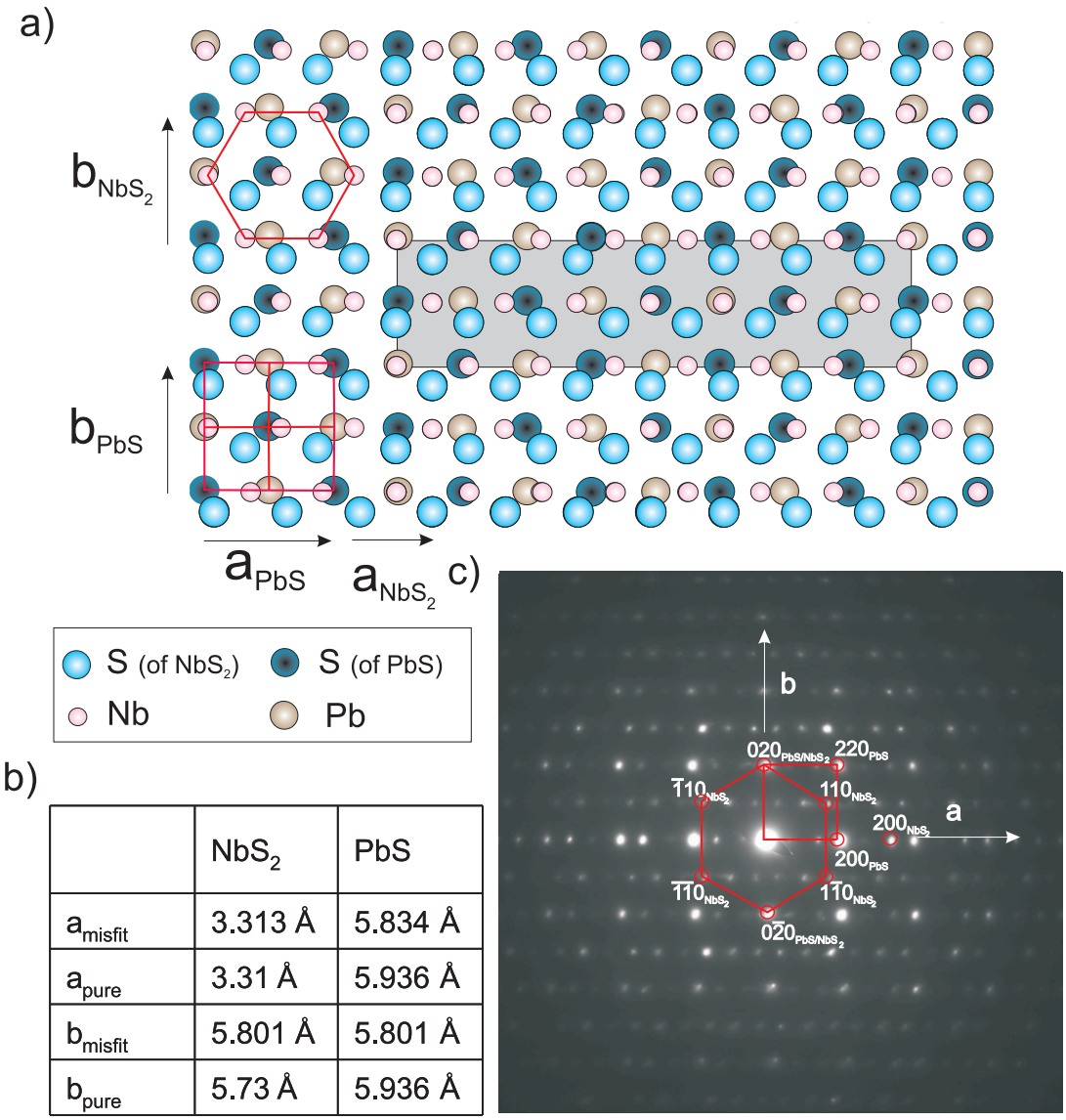

b)

	NbS_2	PbS
a_{misfit}	3.313 Å	5.834 Å
a_{pure}	3.31 Å	5.936 Å
b_{misfit}	5.801 Å	5.801 Å
b_{pure}	5.73 Å	5.936 Å

Figure 5.1: *(a) Projected top view (along [001] axis) scheme of the atomic configuration of the misfit layered compound $(PbS)_{1.14}NbS_2$ derived from the x-ray data of table (b). Parts of the sublattices of the PbS and NbS_2 are highlighted by the red rectangle and hexagon respectively. The artificially constructed supercell is indicated by the grey box, where the otherwise irrational ratio of a_{PbS} and a_{NbS_2} is approximated to 7/4. In* **a** *and* **b** *direction the misfit lattice is only slightly modulated with respect to that of the pure compound. The parameters are listed for comparison in the table (b). The corresponding zone axis electron diffraction pattern (c) is indexed around the central spot of the directly transmitted beam. The four- and sixfold symmetry of the spots from the sublattices are highlighted in red.*

Three types of reflections occur in these electron diffraction patterns: First, reflections originating from both subsystems like the directly transmitted beam and the (020) reflection. Second, reflections that are exclusively from either the NbS_2 or the PbS and third, satellite reflections from multiple scattering events where different reciprocal lattice vectors **g** from both subsystems are involved.

Another method of indexing consistently is the four-integer notation (h_1klh_2) used by [14]. Here, h_1 refers to a_{PbS} and h_2 to a_{NbS_2}. For example the $(020)_{PbS/NbS_2}$ reflection then becomes (0200), the $(200)_{PbS}$ becomes (2000) and so on. The complete structure can then be described in a supercell with indices (HKL), where $H = mh_1 + nh_2$, $K = k$ and $L = l$ and $a_{PbS}/a_{NbS_2} = m/n$. Obtaining a particular H can be achieved by an infinite number of combinations of h_1 and h_2. Considering such a combination (h_1, h_2), both subsystems contribute to the appropriate reflection, e.g. to the (0kl) reflections. As a result, one can see that any satellite reflections from a subsystem contribute to the basic reflections of the other subsystem. This effect can be neglected as long as only the basic structures should be determined, but has to be taken into account if this structure is modulated. For an irrational a_{PbS}/a_{NbS_2} as in an incommensurate system like $(PbS)_{1.14}NbS_2$, different combinations (h_1, h_2) that lead to the same H will originate from satellite reflections with slighly different positions and the intensity is given by the sum of different intensities. For such a case it is impossible to describe the structure in a three dimensional supercell.

5.1.2 Lattice projection along the [100] axis of $(PbS)_{1.14}NbS_2$

Figure 5.2 (a) shows the projected sideview of a single slab along the [100] direction determined from the x-ray diffraction data in table (b). In this projection both commensurate directions **b** and **c** can be studied.

Along the **b** direction both subsystems are modulated in such a way that b_{NbS_2} equals b_{PbS}. The electron diffraction pattern 5.2 (c) shows this commensurability, as the row of reflections for both subsystems have exactly the same distance from the central spots. The row of reflections can then be indexed as (0kl) with $k = 0, 2, \overline{2}, 4, \overline{4}...$ and the appropriate l values as outlined in the diffraction pattern.

To achieve the commensurability, b_{NbS_2} is elongated about 7 pm and at the same time b_{PbS} is compressed by 13 pm according to the x-ray diffraction experiments (compare the values for the pure compounds and the misfit in table 5.2 (b)). As a result of that, the PbS subsystem structure is additionally modulated as shown in the projected view (a): The unit cell is kind of "sheared"so that the sulphur atoms lurk towards the center of the projected unit cell while at the same time the much heavier lead atoms protrude from their original positions so that the Pb-Pb atom distance is effectively less decreased by the compression.

The PbS double layers are intercalated into each van-der-Waals gap of the NbS_2, but as a result of the 2H structure of the NbS_2 the lattice vector $\mathbf{c}_{NbS_2}$ is exacly 2 times larger then $\mathbf{c}_{PbS}$. The doubling of the **c** vectors of both subsystems as table 5.2 (b) suggests is therefore only derived by the intercalation and does not alter the atomic distances *within*

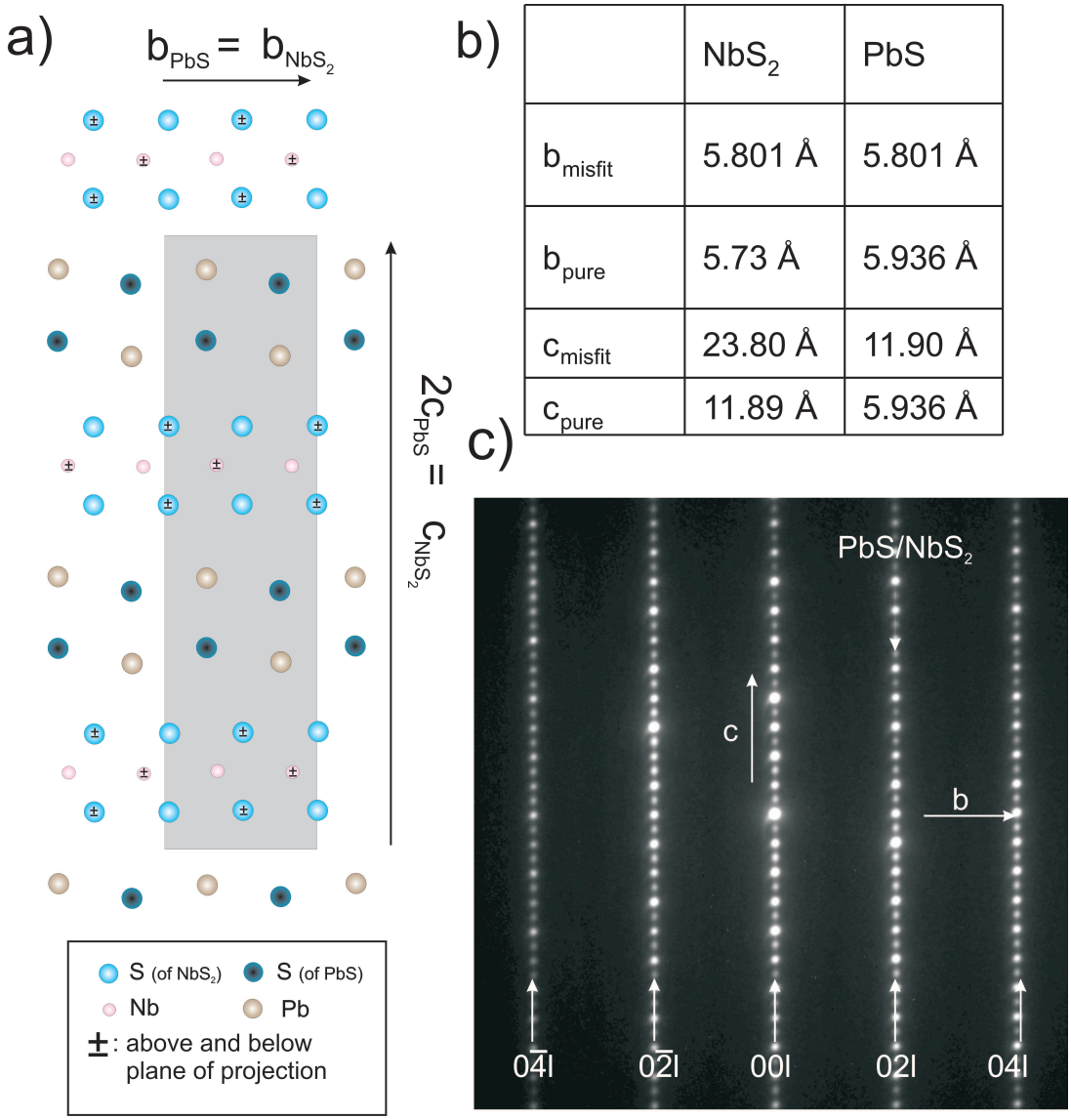

	NbS_2	PbS
b_{misfit}	5.801 Å	5.801 Å
b_{pure}	5.73 Å	5.936 Å
c_{misfit}	23.80 Å	11.90 Å
c_{pure}	11.89 Å	5.936 Å

Figure 5.2: *(a) Projected sideview scheme of a single slab (atoms above and below plane of projection are indicated with ±) along the incommensurate axis of the atomic configuration of the misfit layered compound $(PbS)_{1.14}NbS_2$ derived from the x-ray data of table (b). The lattice constants are commensurate in both* **b** *and* **c** *direction with $b_{NbS_2} = b_{PbS}$ and $2 \cdot c_{PbS} = c_{NbS_2}$. The commensurability in* **b** *direction is achieved by compression and elongation of the unitcells of the subsystems as the x-ray diffraction values of the pure and misfit compounds in table (b) point out. The corresponding zone axis electron diffraction pattern (c) shows the commensurability, as the distance of the row of reflections in* **b** *direction from the central spots are obviously the same for NbS_2 and PbS.*

the respective unit cells.

The origin of the weak spots in the electron diffraction pattern in figure 5.2 (b) is not clear. While the projection of the 2H NbS_2 lattice in this direction yields a periodicity that is equal to the one of PbS, the bright spots show a distance in reciprocal space that is in correspondance with that. The weak spots in between show a periodicity belonging to a distance of 2.38 nm which is exactly the value of the **c** lattice vector of the 2H NbS_2. This is an effect that further investigation should clarify.

5.1.3 Lattice projection along the [010] axis of $(PbS)_{1.14}NbS_2$

The crystallographic direction that was studied in detail in this work is the one along the [010] axis where the interfaces of the two subsystems are incommensurate. Due to the stacked nature of the misfit layered compounds, in fact *every* interface along that direction is incommensurate and that gives rise to certain inhomogeneities that will be presented and discussed. It should be noted, that such a high density of incommensurate interfaces can exclusively be found within the misfit layered materials, which makes them so outstanding.

Figure 5.3 (a) shows the projected crystal structure of a single slab in the [010] direction. Along the **c** axis, the behaviour already described in the previous section appears: From the position of the PbS subsystem in the van-der-Waals gaps of the NbS_2, the lattice vector $\mathbf{c}_{PbS}$ is defined in such a way, that it is exactly 1/2 of the value of $\mathbf{c}_{NbS_2}$ due to the 2H structure of the NbS_2.

The interface between the two subsystems perpendicular to **c** is the incommensurate one, where the lattice constant ratio of $\mathbf{a}_{PbS}$ and $\mathbf{a}_{NbS_2}$ is irrational. Nominally, the incommensurability is given by the values from the table in figure 5.3 (b):

$$\frac{a_{PbS}}{a_{NbS_2}} = \frac{5.834\mathring{A}}{3.313\mathring{A}} \approx 1.7609. \tag{5.1}$$

For image intensity simulations and other computational purposes an incommensurate interface can not be described analytically, because the resulting unit cell would be of infinite size in that direction. For such purposes it is usual to approximate a commensurability that has on the one hand a value as close as possible to the incommensurate one and on the other hand does not make the resulting unit cell too large for the practical use. In the case of $(PbS)_{1.14}NbS_2$ this is achieved by defining

$$\frac{a_{PbS}}{a_{NbS_2}} = \frac{7}{4} = 1.75. \tag{5.2}$$

This is visualized by the grey box, that yields the new unit cell that was already referred to as *supercell* in the previous sections.

The modulations within the PbS structure, i.e. the protrusion of the Pb atoms from the compression of the unit cell as described in section 5.1.2 is also visual in the projection along the incommensurate axis as 5.3 (a) depicts.

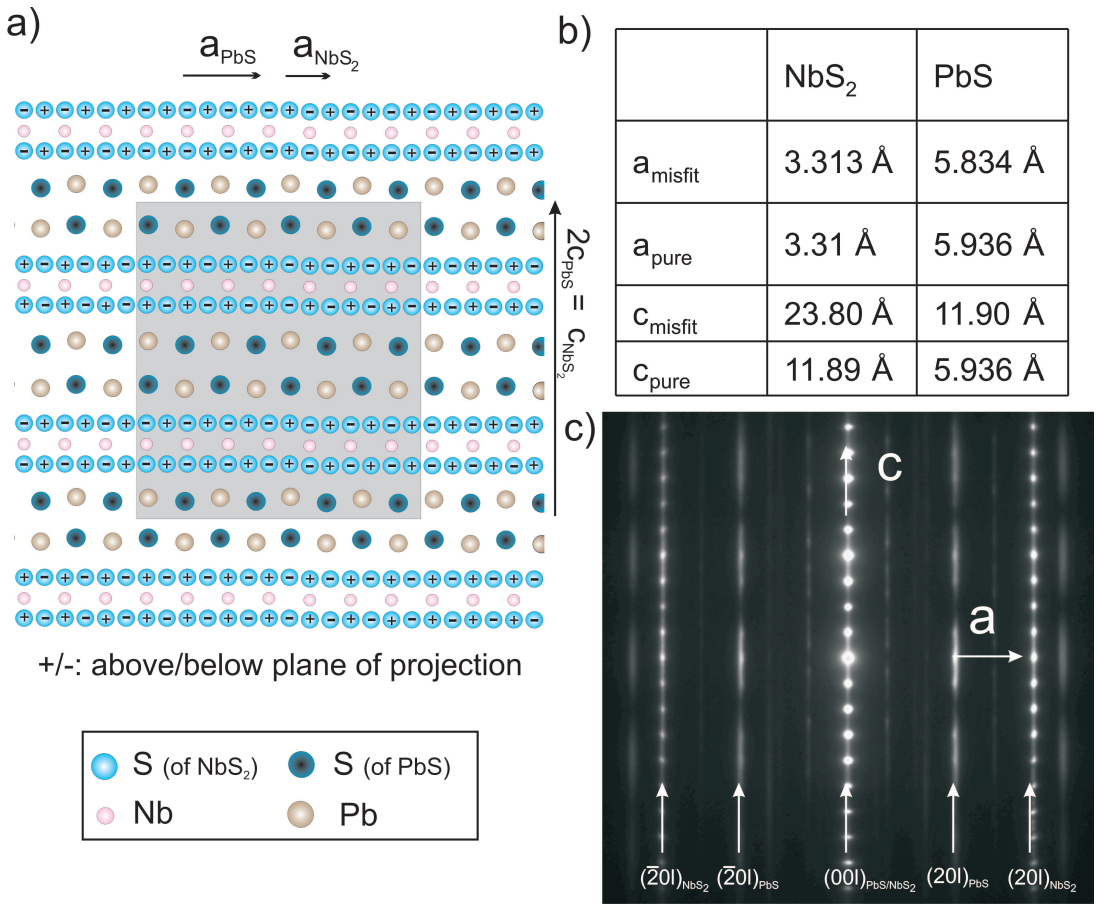

	NbS_2	PbS
a_{misfit}	3.313 Å	5.834 Å
a_{pure}	3.31 Å	5.936 Å
c_{misfit}	23.80 Å	11.90 Å
c_{pure}	11.89 Å	5.936 Å

Figure 5.3: *(a) Projected sideview scheme along the commensurate axis of the misfit layered compound $(PbS)_{1.14}NbS_2$ derived from the x-ray data of table (b). Only a single slab is shown, with + or - denoting the atom to be situated above or below the plane of projection. The lattice constants are commensurate in* **c** *direction with* $\mathbf{c}_{NbS_2} = 2\mathbf{c}_{PbS}$. *The incommensurability in* **a** *direction arises from the irrational ratio of* a_{PbS} *and* a_{NbS_2} *as can be seen from the x-ray diffraction data for both the pure compounds and the misfit in the table (b). The structure must be approximated for e.g. image intensity simulations to be commensurate, and thus a supercell as indicated by the grey box is constructed where the ratio of* a_{NbS_2} *and* a_{PbS} *is set artifically to 7/4. The corresponding zone axis electron diffraction pattern (c) shows the incommensurability, as the distance of the row of reflections in* **a** *direction from the central spots differ clearly for* NbS_2 *and PbS. Each row can be indexed as* $(h0l)_{PbS/NbS_2}$, *with* $h = 0, 2, \bar{2}...$ *and the appropriate l value for the* **c** *direction. The reason for the streaking of the reflections will be discussed in section 5.7.*

The electron diffraction pattern showed in figure 5.3 (c) directly reveals the incommensurability when the distances of the respective $(20l)_{PbS}$ and $(20l)_{NbS_2}$ row of reflections are determined. Additional features can be seen in the electron diffraction pattern that are not present in the electron diffraction pattern taken along the [100] direction (fig. 5.2 (c)): First, the reflections are not sharp points as in the commensurate direction but streaked along **c**. This phenomenon appears exclusively in this crystallographic direction and will be discussed and explained in detail in a following section, where it will be proved that stacking disorder is the origin of this lattice inhomogeneity.

Second, additional rows of weak reflections parallel to the main $(h0l)_{PbS/NbS_2}$ (with $h = 0, 2, \overline{2}...$) ones can be identified that arise from multiple scattering events with lattice vectors **g** from both subsystems involved. The multiple scattering causes also the satellite reflections from the [001] diffraction pattern shown in figure 5.1 (c).

It can also be seen that the intensity of the PbS reflections oscillates with a period of $\sim 8 \cdot g_c$. This is due to reciprocal lattice vectors that belong to diffraction planes within the PbS subsystem connecting the single slabs in a diagonal way. In Fourier space this yields such intensity modulations along a reflection line in **c** direction if the stacking is disordered due to the convolution with the undistorted diffraction pattern. For h = 0 this results only in intensity modulations of the basic reflections, as the EDP also confirms, because the projected lateral structure for h = 0 does not "see"any disorder in the stacking.

5.2 Conventional Z-contrast imaging

The HAADF STEM was performed with the recently installed Tecnai F 30 microscope in the Nanolab Kiel. Although the parameters of the microscope were not characterized at the time of the experiments, Z-contrast imaging was performed as a first test to find out whether it is possible to resolve the lattice structure of the misfit layered compound $(PbS)_{1.14}NbS_2$ using this technique. The nominal resolution for a properly aligned microscope of that type should be about 0.17 nm in the STEM mode.

Figure 5.4 shows two of the first ever taken Z-contrast images with the microscope after installation. Imaging was done along the commensurate direction of the $(PbS)_{1.14}NbS_2$ lattice. Although at this early stage the characterization of the microscope parameters were far from perfect (e.g. electronic instabilities during the scanning of the probe cause the lateral displacements of individual pixel rows), it was possible to image the layered structure of the compound, as the bright image intensities that belong to atom columns with high atomic number Z demonstrate.

As the insets show, the fourfold symmetry of the PbS subsystem is locally visible, although the contrasts are strongly blurred. From the NbS_2 subsystem which has much shorter interatomic distances than the PbS part, only the Nb is resolved as bright lines between the PbS part shoe in the enlarged picture in figure 5.4. This is not surprising, as the atomic number Z of the sulphur is far smaller than the one of Nb.

However, as there was no more time for a characterisation of the microcope parameters in HAADF STEM mode, no further investigations with this technique were performed.

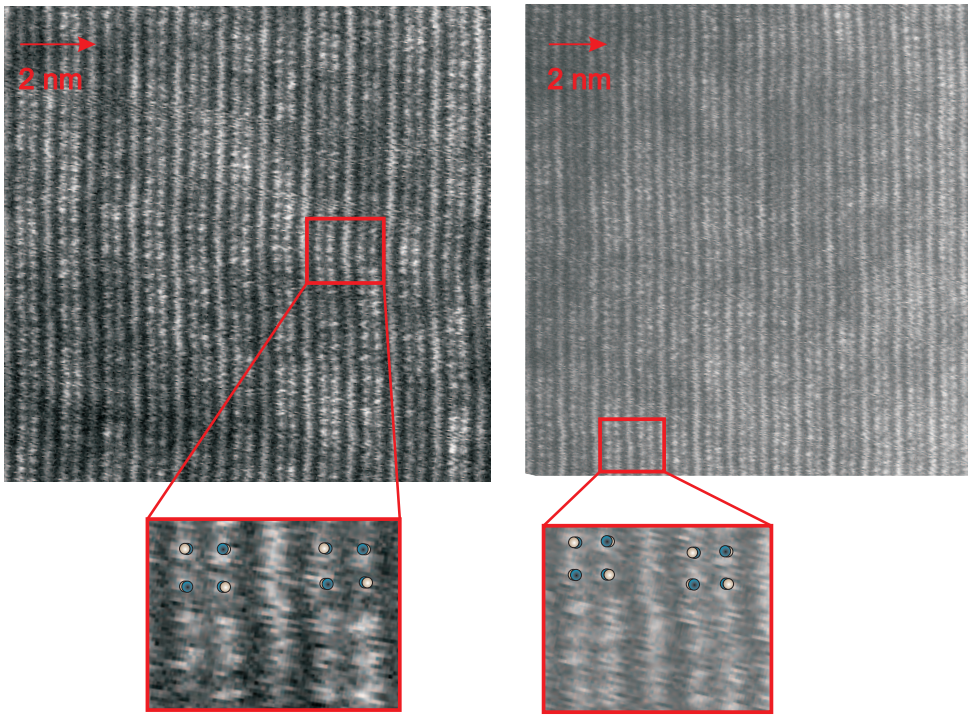

Figure 5.4: *Two of the first ever taken HAADF STEM Z-contrast images with the recently installed Tecnai F 30 microscope in Kiel. The images were recorded along the commensurate direction of the misfit layered compound* $(PbS)_{1.14}NbS_2$. *Although there was no time for characterisation of the microscope parameters in this imaging mode, the layered structure is clearly visible. As the insets shows, the fourfold symmetry of the PbS subsystem and the Nb in between can be identified, although the atom column contrasts are strongly blurred. The weak scattering S columns close to the Nb are not resolved. Parameters used are spot size 9, gun lens 6, condensor aperture 100 µm and camera length 80 mm (left) and 100 mm (right).*

This will be a task for the future application of this mode.

5.3 Plan-view imaging

The plan-view imaging along the [001] axis of $(PbS)_{1.14}NbS_2$ requires samples prepared by the cleavage process described in section 4.1.2. This method produces clean surfaces over large areas but can introduce abrupt changes in the sample thickness, because each created step consists of one or more subsystem layers. This is schematically shown in figure 5.5 (a).

Those abrupt thickness steps alter the contrast features in the experimental HRTEM image. The thickness is supposed to change from the thin edge on the left to thicker regions on the right of the plan-view NCSI contrast image of the misfit layered compound

$(PbS)_{1.14}NbS_2$ in figure 5.5 (b) . The contrast changes are clearly visible as the enlarged parts of the picture below the image illustrate and the multislice simulations below the enlarged images confirm this thickness dependence of the experimentally obtained contrast.

For thin regions a pseudo-square configuration of intensity peaks dominates the contrast that can be intuitively associated with the PbS subsystem. The multislice simulation for NCSI contrast conditions at a thickness of 4.8 nm confirms that this fourfold arrangement is due to the PbS part of the misfit compound crystal.

The enlarged image part in the middle shows the rows of bright intensity peaks shifted towards each other producing a pseudo-hexagonal symmetry. Whether this is due to the NbS_2 subsystem can not be verified from the simulation. Although it reproduces the peak shift towards each other for a thickness of 11.9 nm, the hexagonal configuration associated with the NbS_2 can not be perfectly reproduced.

According to [14] influences of the diffraction condition produce the pronounced hexagonal pattern. If the low order reflections due to NbS_2 are the most intense ones in the electron diffraction pattern the corresponding image will prominently exhibit the hexagonal pattern. If on the other hand the low order reflections due to PbS are the most intense ones the pattern will be predominantly square-shaped. As the sample thickness determines the relative intensities of the reflections in the electron diffraction pattern, it also determines whether the square or the hexagonal configuration dominates the image intensity.

For even larger sample thicknesses the intensity patterns become much more complicated. The enlarged image part on the right is poorly reproduced by the multislice simulation at a sample thickness of 14.3 nm where the weak phase object approximation is obviously not anymore applicable.

One significant feature within the plan-view images are pronounced modulations of the intensity of the bright peaks along the incommensurate direction that appear over large areas of the images. Figure 5.6 show such modulations in an NCSI contrast image of $(PbS)_{1.14}NbS_2$ along the [001] direction, some of them are examplarily highlighted with circles around the intensity peaks.

These modulations, which were also found by other authors [14] on similar misfit layered compounds, consist of three or four bright intensity peaks (red circles) that alternate with four or three diffuse peaks (blue circles) that are clearly less bright. The sum of all peaks in such a pattern is always 7 and that defines a periodic pattern length. In adjacent rows along the incommensurate axis these intensity patterns are in anti-phase: each row of peaks is shifted by the half period along the incommensurate axis.

These periodic pattern are directly linked to the incommensurability of the misfit layered compound $(PbS)_{1.14}NbS_2$. The periodicity of the modulations is $2/\Delta g_1$ where $\Delta\mathbf{g_1}$ is the difference vector from the basic reflections $(200)_{NbS_2}$ and $(400)_{PbS}$ as illustrated in the electron diffraction pattern inset in figure 5.6. The difference vectors $\Delta\mathbf{g_1}$, $\Delta\mathbf{g_2}$ and $\Delta\mathbf{g_3}$ that connect the basic reflections in the EDP and generate the satellite reflection positions determine the periodicity of the intensity modulations.

The "wavefront"of the intensity modulation that corresponds to $\Delta\mathbf{g_1}$ is along the $\mathbf{b}$

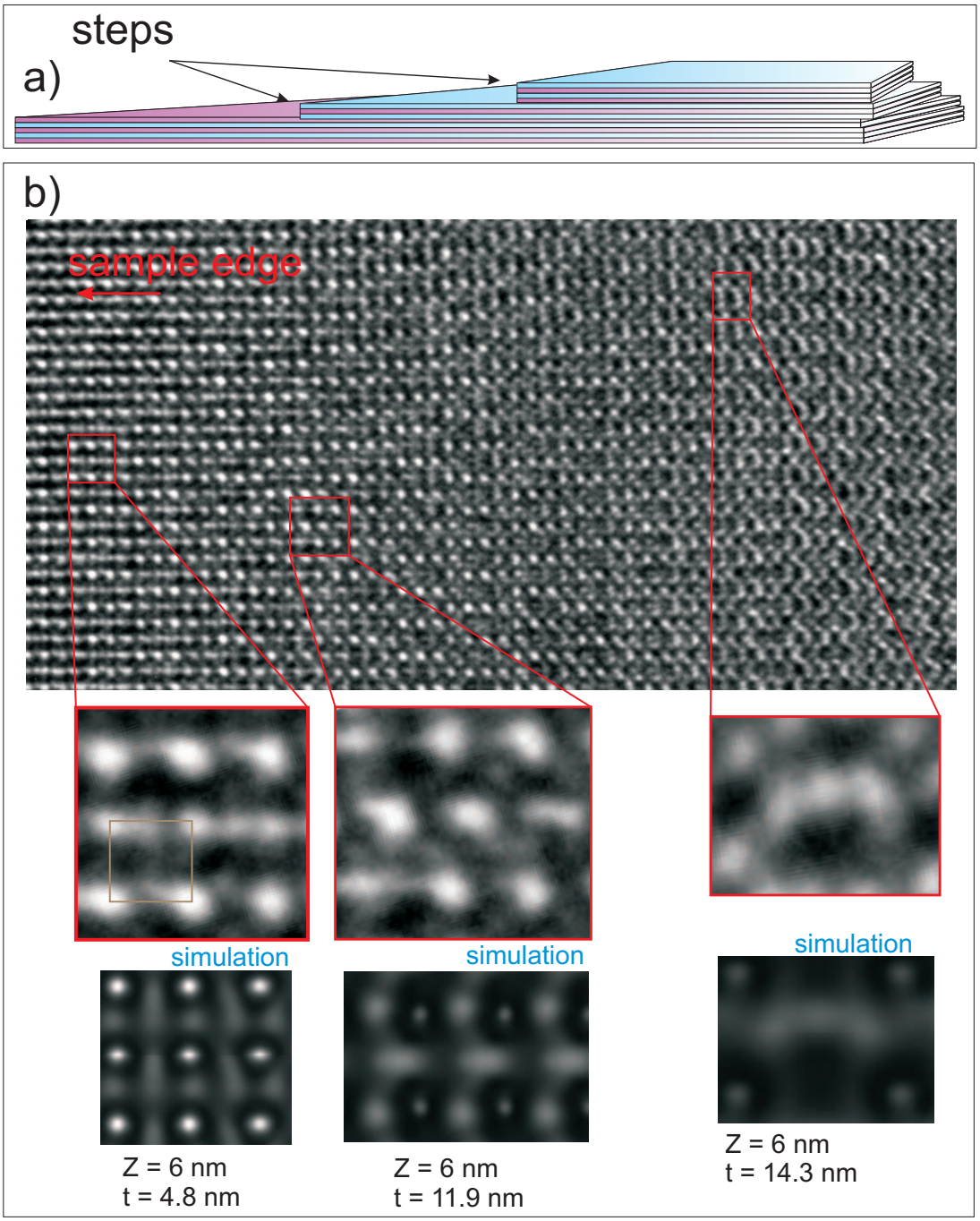

Figure 5.5: *Plan-view imaging along the [001] direction of the misfit layered compound* $(PbS)_{1.14}NbS_2$. *(a) Abrupt thickness changes alter the image contrast as steps are created during the cleavage preparation technique. This radical change in HRTEM image contrast is demonstrated by the experimental NCSI contrast image (b), where the sample thickness increases from left to right. The appropriate multislice simulations for NCSI conditions confirm this behaviour as the enlarged parts of the image show when compared to the simulations below.*

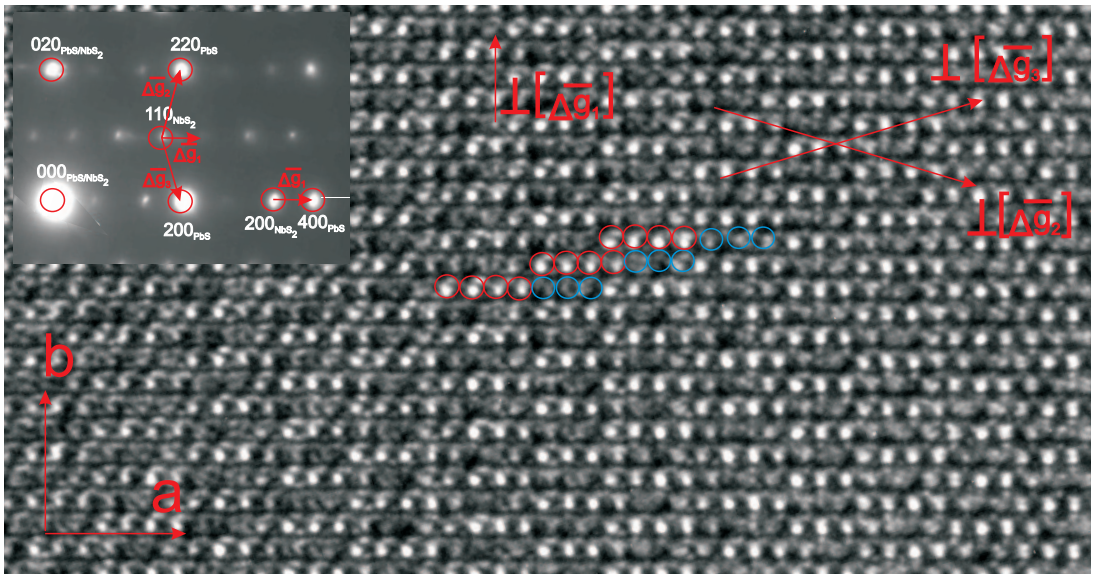

Figure 5.6: *Periodic intensity modulations in a NCSI contrast image taken along the [001] direction of the misfit layered compound* $(PbS)_{1.14}NbS_2$*. The "wavefronts"of the intensity modulations correspond to the reciprocal lattice vectors* $\Delta\mathbf{g_1}$*,* $\Delta\mathbf{g_2}$ *and* $\Delta\mathbf{g_3}$ *that connect basic reflections in the electron diffraction pattern as the inset on the upper left shows.*

direction, while the two corresponding to $\Delta\mathbf{g_2}$ and $\Delta\mathbf{g_3}$ that point in directions perpendicular to $\Delta\mathbf{g_2}$ and $\Delta\mathbf{g_3}$ in the EDP are illustrated with red arrows in the NCSI image. The latter two are more pronounced because $\Delta\mathbf{g_2}$ and $\Delta\mathbf{g_3}$ connect basic reflections with higher intensities.

These intensity modulations could not be found in the multislice simulations for any parameters of focus and thickness. This is not surprising, because they are a direct consequence of the incommensurability that cannot be included in a supercell used as an input for the simulations.

5.4 Conventional and aberration-corrected HRTEM imaging

The comparison between experiment and simulation for conventional (a) and aberration-corrected HRTEM (b) is shown in figure 5.7, where the $(PbS)_{1.14}NbS_2$ structure is imaged along the commensurate axis: The experimental image on the left recorded with a conventional FEI Tecnai F30 S-Twin HRTEM microscope confirms the contrast features predicted by the simulation done with the same quantities for accelerating voltage, spherical aberration, defocus, defocus spread, semiconvergence angle, and sample thickness, although they clearly show no easy accordance with the real structure as depicted by the inset. It is not possible for any combinations of defocus and thickness values to achieve

contrast where the intensity maxima directly represent the atom columns of the crystal.

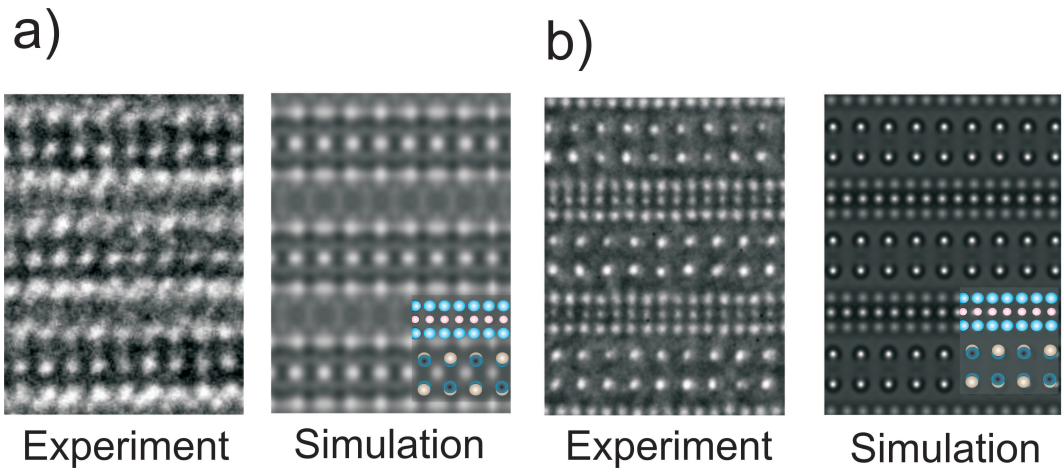

Figure 5.7: *(a) Conventional HRTEM image and simulation along the commensurate interface direction of $(PbS)_{1.14}NbS_2$ taken with the Tecnai F30 S-Twin instrument (a) and the aberration-corrected Titan T 80-300 kV (b). The sample thickness is 3.5 nm in both cases, the projected crystal structure is shown in the insets. (a) There is no simple relationship between image contrast and the atomic structure due to the limiting effect of image delocalization. Simulation parameters: E = 300 keV, C_s = 1.2 mm, Z = -30 nm, $\Delta(Z)$ = 5.3 nm, α = 0.3 mrad. (b) The image contrast and projected crystal structure of both experiment and simulation can directly be associated with each other. Simulation parameters: E = 300 keV, C_s = -12.7 μ m, Z = +5.8 nm, $\delta(Z)$ = 2.9 nm, α = 0.2 mrad.*

Figure 5.7 (b) shows an experimental image recorded with the aberration corrector equipped FEI Titan 80-300 kV (left) and the appropriate multislice simulation (right). The inset of the projected atomic configuration shows that the resulting image intensity peaks correspond directly to the atom columns of the lattice structure. The experimental image reproduces this contrast, like the bright intensity maxima that represesent the atomic columns, very well. These observations are the basic motivation of using the method of NCSI contrast imaging on the interfaces of the misfit crystal.

It should be indicated that one contrast detail of the NbS_2 part of the misfit differs in the experimental NCSI image 5.7 (b) from the simulation. The Nb columns show brighter contrast than the S columns in the multislice simulation while in the experimental image the contrast is brighter for the S columns. This is much likely due to the Debye-Waller factors used within the multislice algorithm [86] that are derived with x-ray experiments for the pure elements. It is possible to determine much more precise Debye-Waller factors with the help of density functional theory codes for individual unit cells and use these precise data to do image intensity analysis on the atom columns in the micrographs. Unfortunately for a supercell with 148 atoms like the one of $(PbS)_{1.14}NbS_2$ with its van-der-Waals bindings it was not possible to compute correct Debye-Waller factors within a realistic frame of runtime and data storage.

5.5 NCSI contrast imaging

In principle, if the sample if sufficiently thin it is possible to gain localized lattice information from any position of the specimen. Practically, this is of course strictly limited by the thickness (that should be less than 5 nm) and the quality (beam damage from the ion milling; amorphous material) of the samples. A good example for a case where the specimen is on the one hand thin enough and on the other does not have too much amorphous material on top of it is shown in figure 5.8: Over an area of about 20 nm × 20 nm the atom columns are clearly resolved. This NCSI contrast image is taken along the commensurate zone axis of $(PbS)_{1.14}NbS_2$ as the coordinate system depicts. The atom column configuration at a large number of incommensurate interfaces can be perfectly studied in this projection.

The image demonstrates that the weak scattering S columns are individually resolved even in close distance to the much stronger scattering Pb and Nb columns. The local position of atom columns and thus lattice parameters can be determined from the image which demonstrates the advantage of the NCSI contrast imaging technique over the spatially averaging x-ray diffraction experiments.

Note that in this projection along the commensurate axis it is not possible to distinguish between the lead and sulphur columns that basically lie on top of each other and spatially differ only by the slight protrusion discussed in the previous sections. Because of that it is necessary to take into account that the respective intensity "blobs"contain intensity contributions of both the lead and the sulphur columns. Even though the peak maximum will be dominated by the much heavier scattering Pb atoms as can be seen from the simulations (e.g. in figures 4.8 and 5.7), a slight shift towards the S columns will always appear. Figure 5.9 illustrates this effect schematically. An approach to resolve the S and Pb columns independently will be presented in chapter 5.10. In the following the term *lead/sulphur* columns will be used to give consideration to that effect.

5.6 Focal series and reconstruction of the exit-plane wave function

Recording focal series with a conventional instrument, the Tecnai F 30 S-Twin, was done. From the image contrasts in figure 5.7 it is clear, that direct real space structure information from single images can not be gained for complex systems like the misfit layered compounds. Nevertheless computational focal series reconstruction on images taken with the Tecnai were performed.

Figure 5.10 shows a series of 12 images taken with equidistant focal steps of 4.4 nm from -18.8 nm to -66.9 nm along the commensurate interface direction of $(PbS)_{1.14}NbS_2$. The Scherzer defocus for this instrument (with a C_s of 1.2 mm and a defocus spread of 5.3 nm) is at Z = - 59 nm, the thickness of the sample is estimated to 3.5 nm in the imaged region.

All single images in the series show complicated contrast behaviour. The layers can

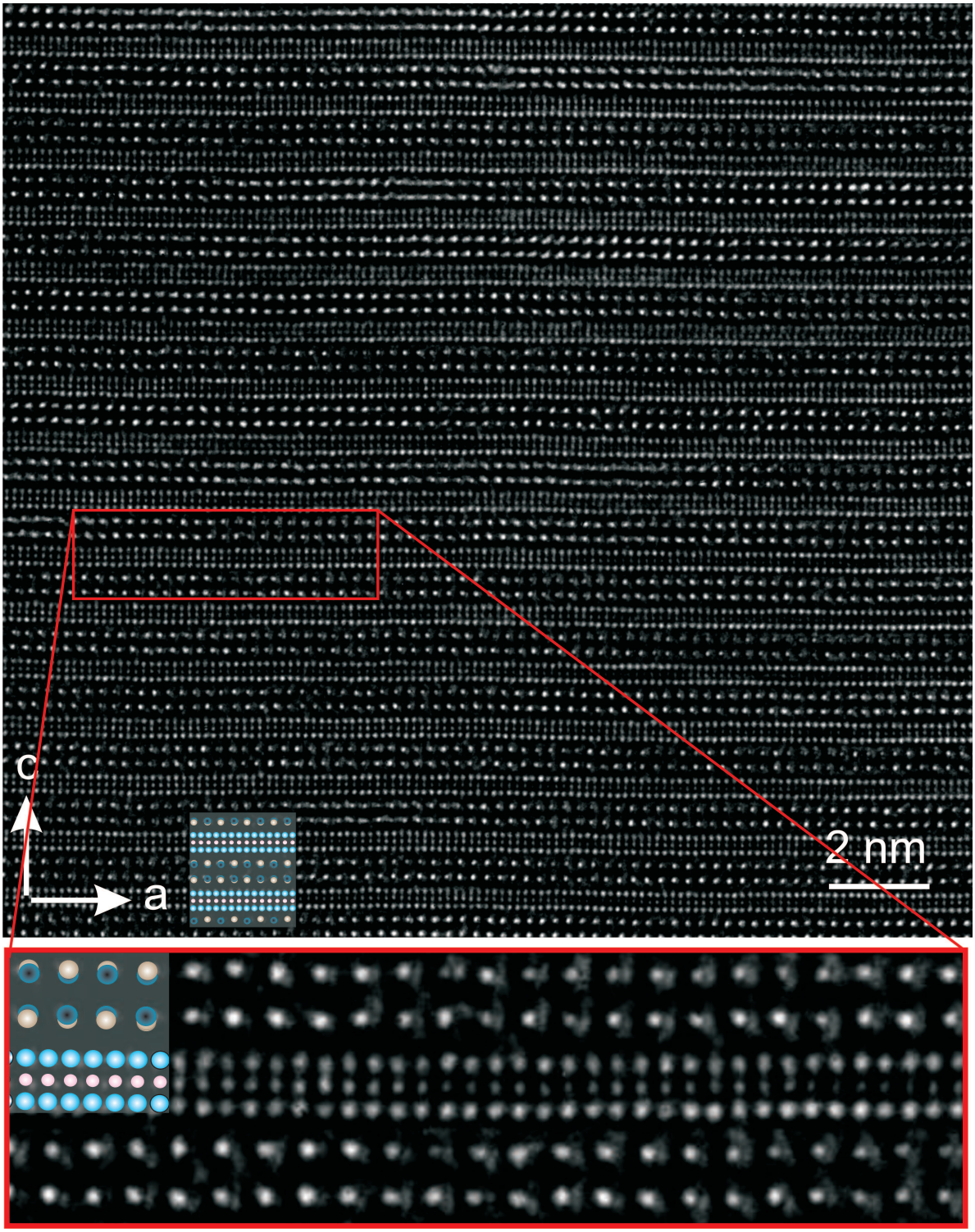

Figure 5.8: *NCSI contrast image (C_s = -13 µm, Z = 5.8 nm) over a sample area of about 20 nm × 20 nm taken along the commensurate zone axis of $(PbS)_{1.14}NbS_2$. This projection shows the atom columns in the* **a** - **c** *plane where the interfaces between the PbS and the NbS_2 are incommensurate. The inset shows the structure schematically. As can be seen by comparison, the intensity maxima depict the atom column positions. The image demonstrates also that it is possible to resolve the weak scattering S columns individually even in close distance to much stronger scattering columns.*

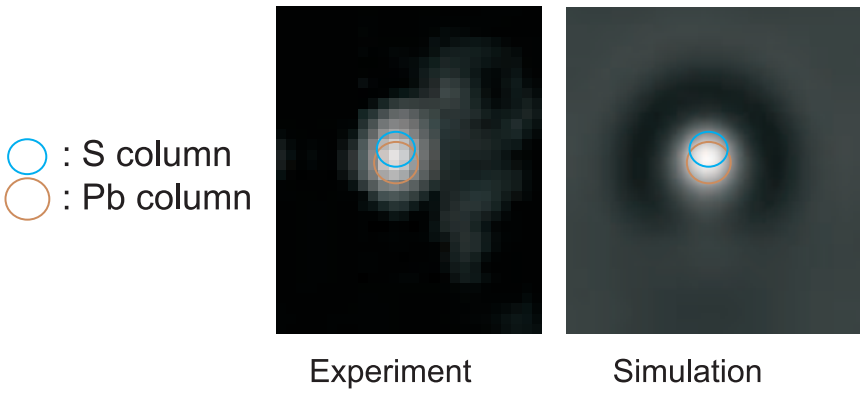

Figure 5.9: *Experimental NCSI contrast image and appropriate multislice simulation illustrating the effect of a slight peak shift (7 pm) of the Pb intensity maximum in the projection along the incommensurate axis of* $(PbS)_{1.14}NbS_2$ *due to the Pb protrusion from the center within the PbS unit cell. The final intensity is the integrated intensity of both the Pb and S columns. Due to that effect the individual Pb and S column positions can not be determined accurately in this projection.*

be identified, but intensity maxima that denote atom columns can hardly be found. Only for defocus values of -27.3 nm and -31.7 nm, fourfold contrast features associated with the PbS become visible. The NbS_2 subsystem cannot be identified from the contrast in any of the images.

The reconstructed phase of the exit-plane wave function reveals details about the atom column structure that could not be gained from any of the focal series images: Although the NbS_2 sublayers are not resolved, one can clearly identify the PbS atom columns as the inset shows which is a good demonstration of the benefits of focal-series reconstruction.

Figure 5.11 shows a focal series recorded with an aberration-corrected HRTEM around the NCSI contrast at $Z = 5.8$ nm for a C_s of approximately -13 μm. This series shows again the $(PbS)_{1.14}NbS_2$ sample along the commensurate interface direction for 9 different defocus values. The insets show the multislice simulations with the appropriate parameters for each defocus value and the projected crystal structure for comparison.

By studying the contrast features of experiment and simulation one can find a very good overall agreement, proving that the alignment of the defocus as well as of the other aberrations was done properly during the experiment. The strongest contrast is predicted to be for the defocus of 6 nm very close to the NCSI contrast which is confirmed by both experiment and simulation. Here, the configuration of the atom columns at the interfaces can be examined very well. In fact, images like the one shown in figure 5.8 and others that will be presented in the following sections are recorded under these conditions to study the geometric properties of the misfit crystal.

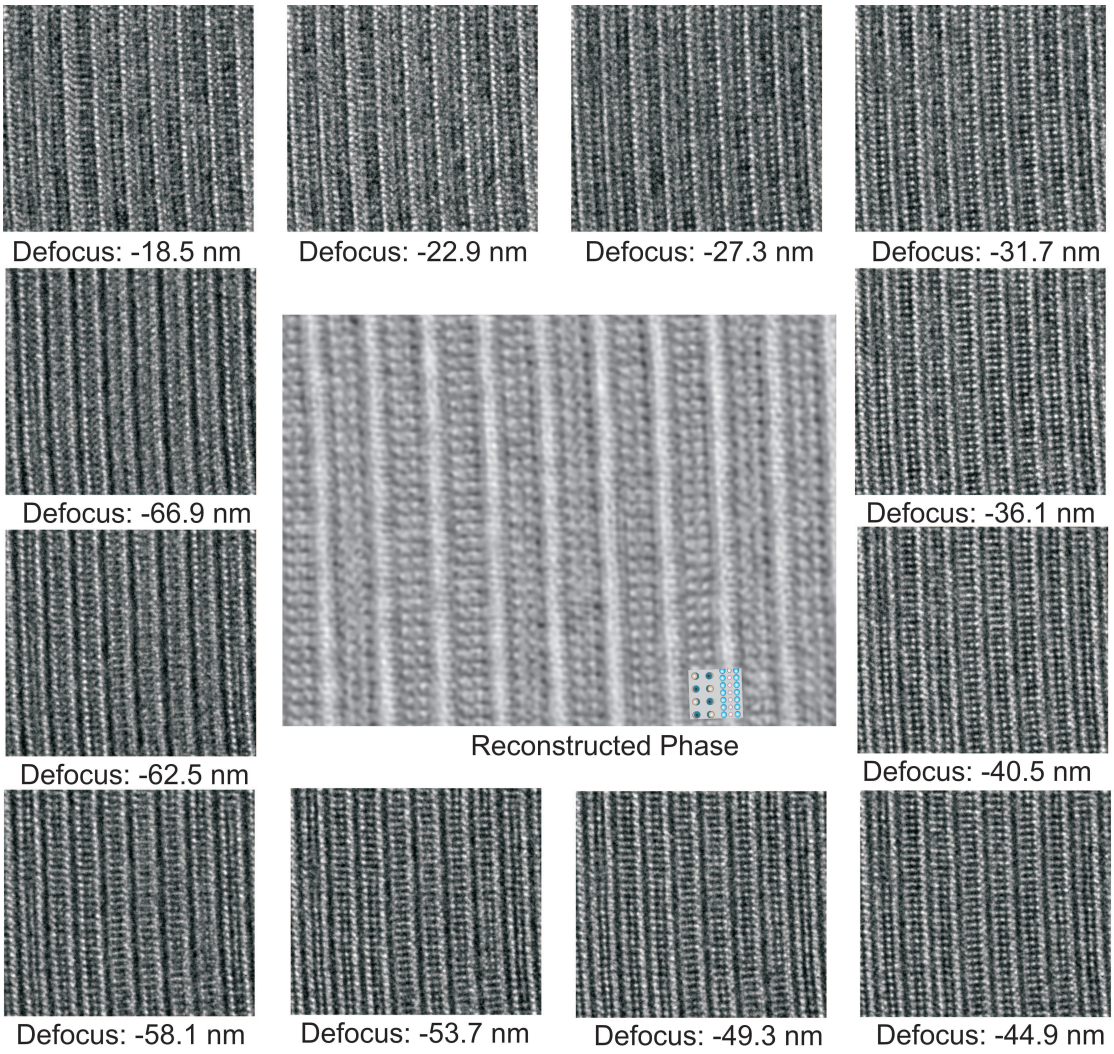

Figure 5.10: *Focal series of 12 images taken with equidistant focal steps of 4.4 nm from -18.8 nm to -66.9 nm along the commensurate interface direction of* $(PbS)_{1.14}NbS_2$ *with a conventional HRTEM (E = 300 kV,* C_s *= 1.2 mm,* $\delta(Z)$ *= 5.3 nm,* α *= 0.3 mrad, sample thickness t = 3.5 nm). Although the single images of the series show no simple relationship to the atom column structure, the PbS subsystem can be clearly identified in the reconstructed phase image of the exit plane wave function (see inset).*

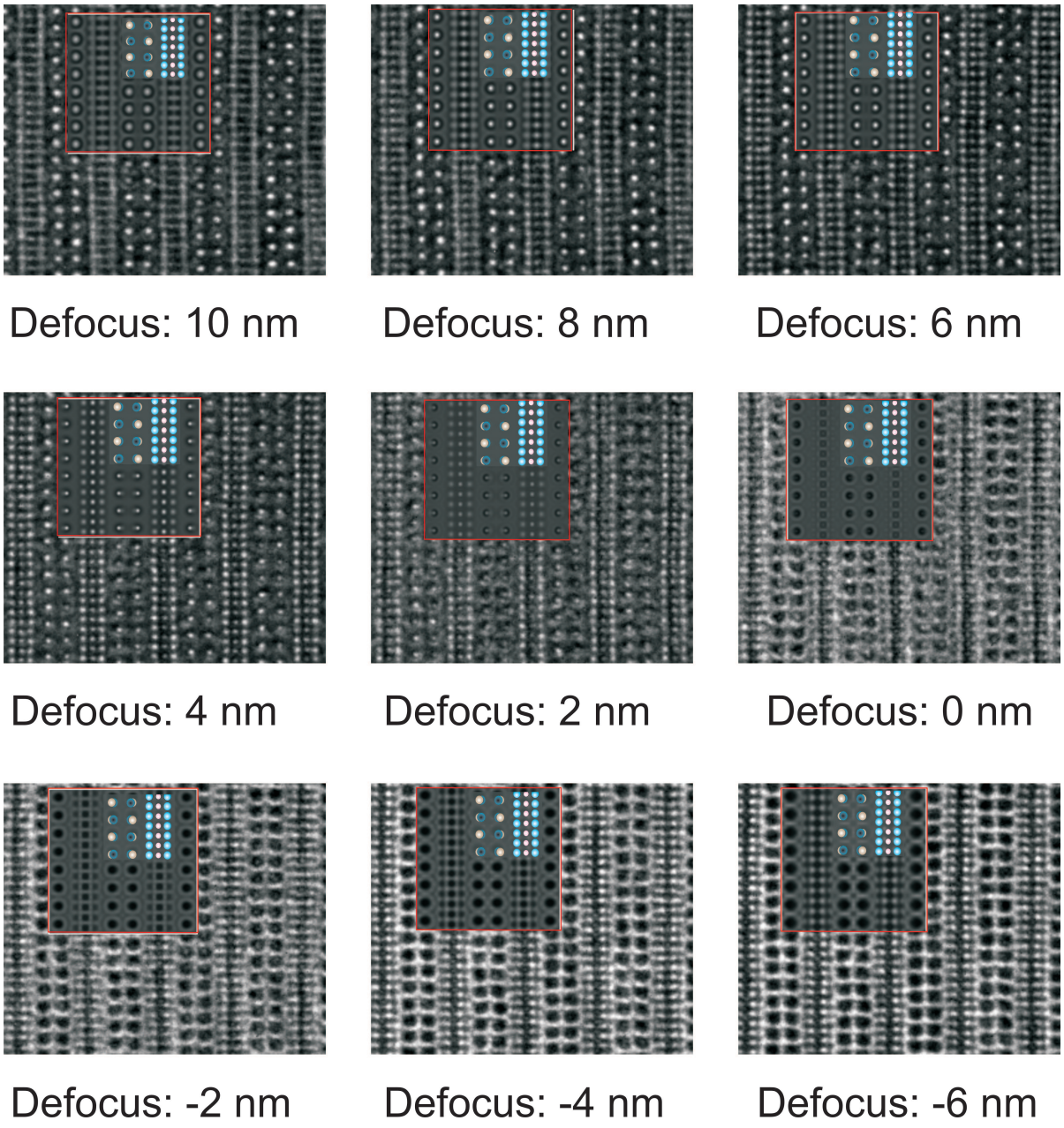

Figure 5.11: *Focal series of 9 images taken with equidistant focal steps of 2 nm from Z = +10 nm to Z = -6 nm along the commensurate interface direction of* $(PbS)_{1.14}NbS_2$ *with an aberration-corrected HRTEM (E = 300 kV,* C_s *= -13 µm,* $\delta(Z)$ *= 2.9 nm,* α *= 0.2 mrad, sample thickness t = 3.2 nm). The insets show the appropriate multislice simulations and the projected atom columns. NCSI contrast is produced for a defocus of 5.8 nm. Overall, the contrast features predicted by the simulations are in very good agreement with the experimental results.*

As can be seen in both simulation and experimental image at $Z = 8$ nm in figure 5.11, the contrast at the positions of the projected potential becomes weaker compared to the NCSI contrast image at $Z = 6$ nm, but the intensity features still give the positions of the atom columns. At $Z = 10$ nm this is not the case anymore, as the NbS_2 subsystem contrast is somehow blurred and instead of three separate intensity peaks (sulphur - niobium - sulphur columns) a complicated streaked pattern appears.

Towards smaller defocus values it can be observed in both simulation and experimental image that the contrast from the lead/sulphur columns changes and the intensity peaks become dark circles. The contrast should reach its minimum around 0 nm defocus which is very well reproduced by experiment and simulation. At lower defoci the contrast for several spatial frequencies becomes inverted due to a zero passing of the CTF which can be good seen as the lead/sulphur columns produce dark blobs for -2, -4 and -6 nm instead of intensity peaks. For defoci of 0 nm and below it can also be seen that the NbS_2 is not anymore represented by three individual intensity peaks.

The focal series reconstruction technique can be used to calculate the exit-plane wave function and its amplitude and phase. Here a serious problem for the misfit layered materials appears that was already mentioned in the chapter 4: during the cross section preparation the ion beam deposits amorphous material onto the sample that was removed from the crystal structure itself. Although a small amorphous edge is desirable to align the aberration corrector, too thick layers of unordered atoms on the top and bottom of the sample disturb not only the contrast in the single images but become together with other instabilities like sample drift a serious problem within the exit wave reconstruction.

Figure 5.12 demonstrates this effect by showing the reconstructed phase image and the NCSI contrast image taken from the same series. Especially the NbS_2 subsystem does not show intensity features that can be directly linked to the projected potential. The insets shows the simulated phase of the exit wave function. The contrasts are even sharper than in both the experimental and simulated NCSI contrast images. The contrast in the reconstructed phase of the exit wave function obtained from the experimental defocus series is remarkably weaker than the simulated one.

Many approaches with different ion etching machines and parameter variations like etching angle and energy were tried out during this thesis. Still the amount of amorphous material on top and bottom of the samples should be reduced in further works.

The effect of amorphous material on the accuracy of determining atom column positions from restored exit waves was found to be the most important factor (compared with other influences as e.g. noise or the restoration method within the reconstruction itself) that limits the reliability of atomic column position estimations [87]. The authors describe their method in detail in [88] [89]. The method was applied on simulations of $SrTiO_3$ with and without amorphous layers and demonstrated that the error in accuracy in the determinations is in the order of about 5 picometers [90]. For very light columns like oxygen these influences increases even more and the error will be up to ≈ 20 picometers. However, for investigations on the atomic configuration of the incommensurate interfaces of the misfit system the NCSI contrast images were used anyway. The knowledge of the whole exit-wave function is not urgently necessary for that purposes.

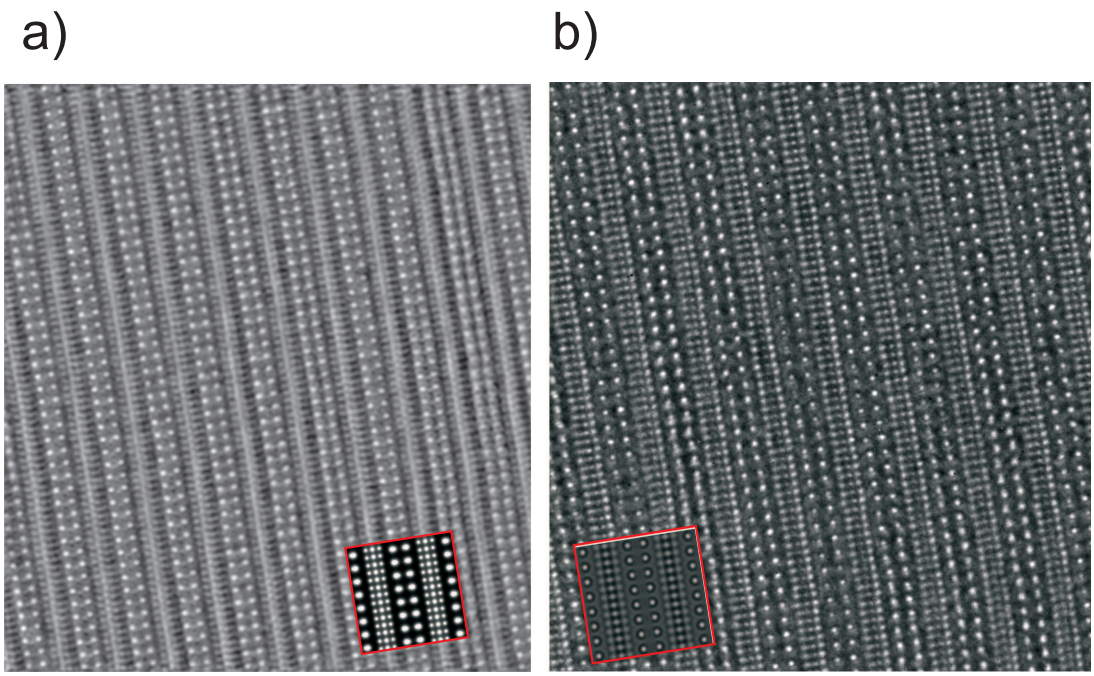

Figure 5.12: *(a) Phase image from the exit-wave reconstruction of a focal series along the commensurate interface direction of $(PbS)_{1.14}NbS_2$ and an NCSI contrast image from the same series. The insets show the simulated image contrasts for the phase of the exit-wave function and the NCSI image. In the reconstructed phase the contrast features are less pronounced than in the simulation, especially for the NbS_2 subsystem. This is most likely due to amorphous material [90].*

5.7 Stacking disorder

The NCSI imaging within an aberration-corrected HRTEM is used for a closer dissection of structural features in the misfit layered compound $(PbS)_{1.14}NbS_2$ beyond the simple determination of lattice parameters. Images taken along the commensurate axis show the atom columns at the incommensurate interfaces, like previously shown in figure 5.8. Several inhomogeneities appear along this axis that will be discussed in detail in this and the following sections. See also the already published literature concerning these phenomena [15] [16]. The inhomogeniety illustrated and explained in this section is the stacking disorder of the PbS along the **c** axis.

As already pointed out in section 5.1.3, the reflections in the electron diffration pattern along the commensurate axis are not sharp points as in the appropriate diffraction pattern along the incommensurate direction but streaked along the **c** direction. While the NbS_2 reflections are almost (but not entirely) sharp spots, the PbS reflections show a pronounced streaking.

When the PbS sublayers are not aligned on top of each other, additional frequencies of the unit cell stacking order in **c** direction occur that introdude additional reflections in

the diffraction pattern as figure 5.13 illustrates.

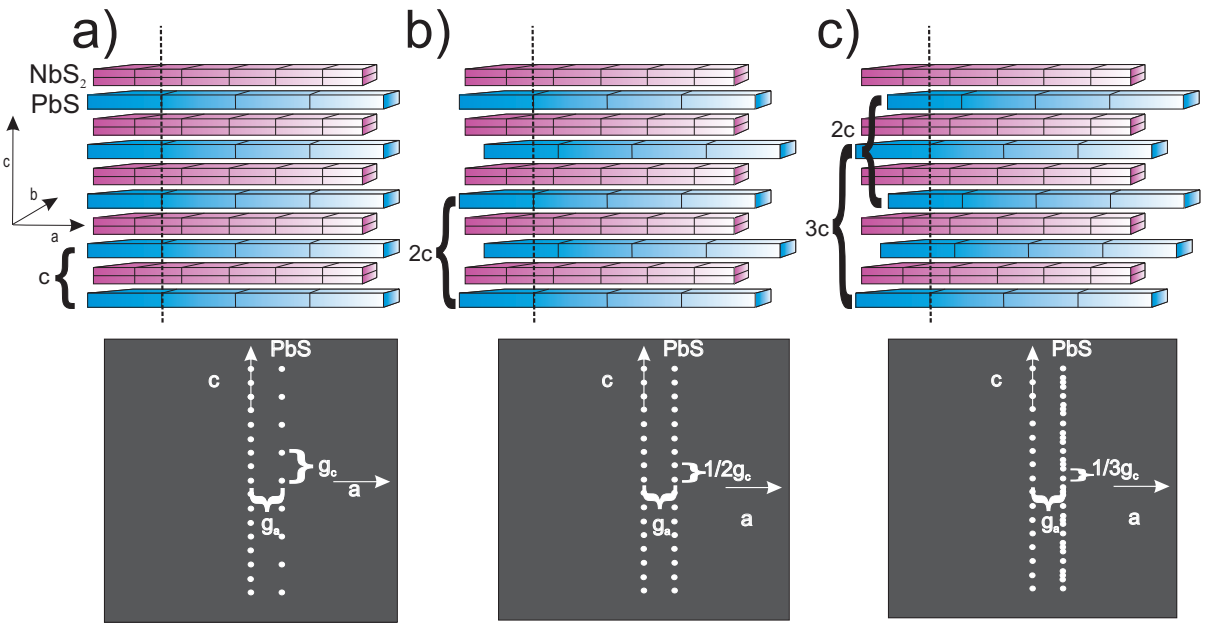

Figure 5.13: *Schematic explanation of a streaking of reflections within an electron diffraction pattern of a stacked misfit compound: Each periodicity within an unit cell produces an appropriate distance between the spots in reciprocal space (a). Adding another periodicity by scrolling some of the PbS sublayers inside the van-der-Waals gaps produces additional reflections (b)+(c). If the stacking is very heavily unordered, many additional reflections occur and the former spots appear as streaked rods.*

Assuming a perfectly aligned crystal as in 5.13 (a), one would expect to find a row of PbS reflections in distance $\mathbf{g}_{a,PbS}$ parallel to the central row of spots like the schematic electron diffraction pattern below demonstrates. Along the **c** direction the peak distance is defined by the lattice vector $\mathbf{g}_{c,PbS}$, that corresponds to the lattice constant **c** of the PbS subsystem. Due to the quasi-two dimensional layered structure of the misfit compound, equidistant reflections with a spacing of $\mathbf{g}_{c,PbS}$ in between will occur. Note, that the central row of reflections has only the half periodicity, because it consists of reflections from both the PbS and the NbS_2, that has a lattice constant $\mathbf{c}_{NbS_2}$ double as large as c_{PbS} and thus the appropriate **g** vector in reciprocal space is only half as long.

Figure 5.13 (b) shows what happens if the stacking is distorted by introducing artificially another lattice period of $2 \cdot \mathbf{c}_{PbS}$. This can be simply achieved when some layers of the PbS subsystem are moved in parallel direction against each other. The electron diffraction pattern will then show additional reflections with distances of $\frac{1}{2}\mathbf{g}_{c,PbS}$.

When adding a third periodicity (c) with $3 \cdot \mathbf{c}_{PbS}$ spots are added to the diffraction pattern in the same manner with distances of $\frac{1}{3}\mathbf{g}_{c,PbS}$ and so on. Therefore it is clear, that a disordered stacking of the PbS inside of the van-der-Waals layers will produce diffraction patterns like the one shown in figure 5.14 (a), where a strong streaking of the

PbS reflections is visible. In principle, any additional periods $n \cdot \mathbf{c}_{PbS}$ with an integer n are possible. However, as the intensity distribution along the **c** axis depicts, those with very large real space periodicities (and thus small **g** vectors) are clearly preferred. This means that each PbS subsystem is randomly shifted in the **a** direction within the van-der-Waals gaps.

It is important to state that the lateral displacement does not effect the row of reflections for l = 0 and that the stacking disorder happens not in the commensurate **b** direction. The oscillations of the PbS reflection intensity is already discussed in section 5.1.3.

This assumption is proved to be true, as the real space NCSI image in figure 5.14 (b) shows: While the majority of the NbS_2 sublayers are aligned on top of each other very well (although not perfectly, confirming the weak intensity streaks between the spots in (a)) as the blue line that follows the atom columns in **c** direction demonstrates, the stacking of the PbS is totally disordered as the red line highlights. It crosses the Pb/S atom columns in each individual layer and illustrates the distance in **a** direction to the nearest Pb/S column of the adjacent higher or lower slab by a 90° kink in the sketched red line.

The diffractogram 5.14 in (c) is taken from an area of about 20 nm × 20 nm and confirms the stacking disorder to be much more dramatic for the PbS than for the NbS_2. As one can see from the blue line in (a), also a minority of the NbS_2 sandwiches are not directly aligned with each unit cell on top of the other, which leads to the slight streaking of the reflections in the diffractogram.

5.8 Tetragonal distortion

The changes of the lattice parameters of the NbS_2 and PbS sublattices within the misfit compound were already discussed in the sections 5.1.1 - 5.1.3. Here, the results from the examinations on the PbS sublattice are presented where another inhomogeneity was discovered.

As explained, the former rock-salt cubic PbS is deformed in several ways when build into the misfit, as the x-ray data from table 5.2 denote. The unit cell is compressed into both the **a** and **b** direction and as a consequence the Pb atoms protrude out of their original positions to keep the interatomic Pb-Pb distance as large as possible.

The increase by factor of nearly 2 of the lattice constant in **c** direction is achieved by the insertion of the PbS slabs into the van-der-Waals gaps of the NbS_2. In that way the distance to the next PbS double layer is increased because of the NbS_2 sandwich that lies in between two PbS slabs and so the lattice constant **c** is effectively doubled. Obviously it is not possible to judge from this **c** value alone, whether the distance in **c** direction between the Pb/S columns within one layer is altered. For clarifications I will refer to this inner-layer distance of the columns now as *c-spacing* and to the appropriate distance in **a** direction as *a-spacing*, which is exactly $1/2 \cdot \mathbf{a}_{PbS}$. These notations are illustrated in figure 5.15 (a).

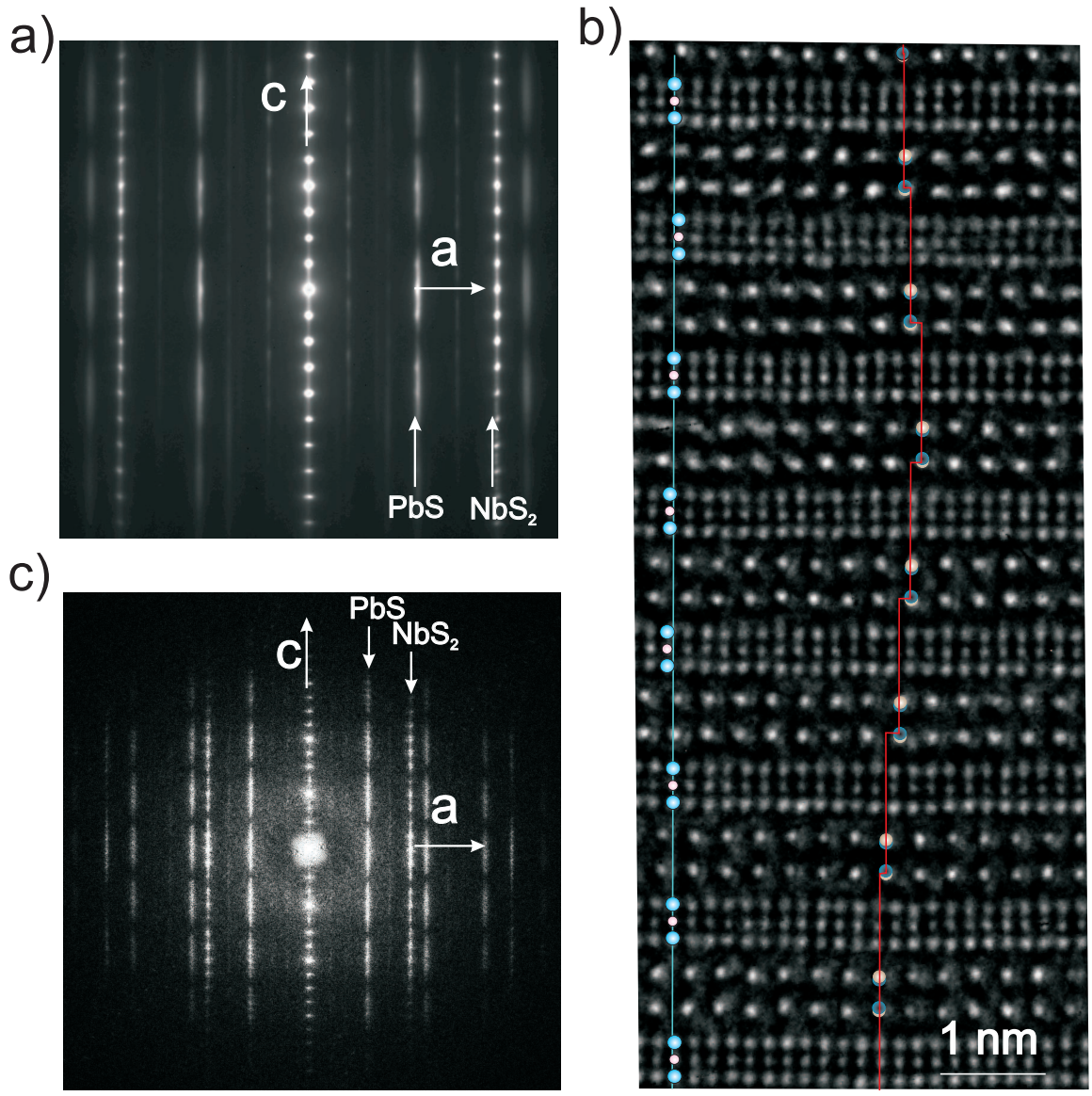

Figure 5.14: *Stacking disorder within the misfit compound* $(PbS)_{1.14}NbS_2$. *The electron diffraction pattern (a) shows a strong streaking of the PbS reflections. According to the model described in figure 5.13, this can be explained by stacking disorder of the PbS subsystem within the van-der-Waals gaps of the* NbS_2. *This is directly found in the NCSI image (b): The red line indicates the disordered stacking of the PbS, while the* NbS_2 *slabs are much better oriented on top of each other (blue line). The diffractogram (c) confirms this behaviour.*

lattice constant	pure	misfit
a_{PbS} $(\AA)$	5.936	5.834
b_{PbS} $(\AA)$	5.936	5.801
c_{PbS} $(\AA)$	5.936	11.902

Table 5.2: *Lattice constants of the PbS subsystem in the pure rock-salt cubic structure and when built into the misfit layered compound $(PbS)_{1.14}NbS_2$. The values are derived from x-ray diffraction data [13].*

For the undistorted cubic PbS it is clear that the a- and c-spacings are the same as $1/2 \cdot \mathbf{a}_{PbS} = 1/2 \cdot \mathbf{c}_{PbS}$ hold true. That is not the case within the misfit compound $(PbS)_{1.14}NbS_2$ as will be demonstrated. The projected atom column spacings from the x-ray diffraction data [13] are listed in figure 5.15 (b). These distances refer to the projected column distances of each atom type, which must not be confused with the real distance between individual atoms. In **a** direction the projected distance is the half value from the $\mathbf{a}_{PbS}$ lattice parameter from table 5.2.

The protrusion of the Pb atoms in **c** direction is reflected by the different distances for the projected columns of Pb and S respectively: While the S-S column distance is only 0.224 nm the Pb-Pb columns are seperated by 0.331 nm, i.e. the Pb columns protrusion from the S columns is 0.0535 nm.

From the multislice simulation in figure 5.15 (a) the distances between the peaks that consist of both the Pb and S column are evaluated. The a-spacing is exactly the same as from the x-ray diffraction data, which confirms that the Pb and S columns are not modulated towards the **a** direction. The projected c-spacing of the simulated Pb/S peak is as expected much larger than the S-S distance but shorter than the value for Pb-Pb because it contains the intensity of the sulphur column and the lead column. The Pb has the much higher Z number it is a much stronger scattering atom type and thus the peak is only slightly shifted away from the real Pb column position by the S column that contributes also to the final peak intensity. From the value of $c^{proj}_{Pb/S} = 0.316$ nm it can be concluded that this shift within the image intensity will be ~ 7 pm.

The determinations of the Pb/S a- and c-spacings from the experimental NCSI contrast and the simulated multislice images were done by peak maximum fitting from the micrographs as demonstrated in figure 5.15 (c): A rectangle covering the peaks is taken and the intensity is integrated parallel to the direction in that the spacing should be determined. This integrated intensity comprises then both the intensity from the S and the Pb column which add up to the experimental peak in the HRTEM image. This integrated intensity is then plotted as a graph as the inset in 5.15 (c) shows.

This is performed for a number of about 100 peak pairs for both lattice directions in the experimental NCSI contrast images as can be seen from the waterfall plot 5.15

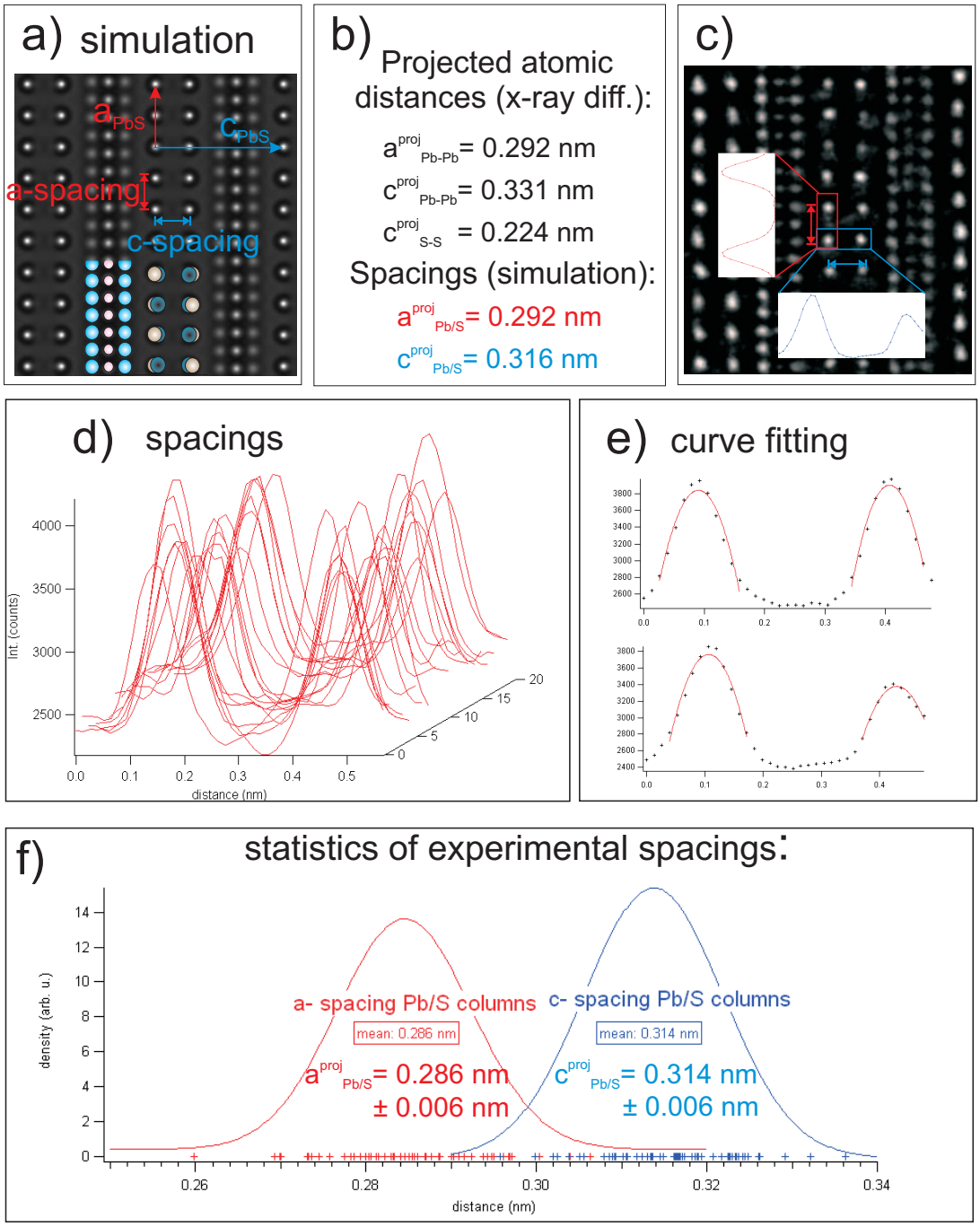

Figure 5.15: *Determination of the a- and c-spacing within the PbS layers in the misfit compound* $(PbS)_{1.14}NbS_2$ *from experimental and simulated NCSI contrast images: The spacings are illustrated in the simulated NCSI image (a), the quantities derived from that listed in (b) together with the x-ray data [13]. The experimental NCSI images (c) are analysed by integration of the intensity within a rectangle around the peaks. Then the peak maxima (d) are plotted by polynomial curve fitting (e) and finally the statistical quantities are gained by Gauss fitting the distribution of the distances between the Pb/S intensity peaks in a and c direction (f).*

(d). Here the intensity is plotted as a function of the real distance, estimated from the discretization quantities from table 4.1. The real peak maxima are then obtained with subpixel accuracy by plotting around the maxima with a quadratic function as can be seen from 5.15 (e). The black markers show the original intensity values for the appropriate pixels of the CCD camera in the NCSI image. The red curve is fitted with a sampling of $\sim 50\times$ smoother then the original, e.g. a peak that consists of 10 pixel in the image is approximated by 500 subpixel points. The two maxima position can then be gained from the fit and the distance is calculated.

The graph (f) in figure 5.15 shows the results from all individual peak distance evaluations together: On the x-axis all experimentally estimated a- (red) and c-spacings (blue) are denoted with markers in the respective color. The Gauss curves are calculated to plot the density of all these markers, i.e. the statisticly averaged quantity of the spacings. The value for the c-spacing of 0.314 nm is in very good agreement with the simulated one, while the averaged a-spacing of 0.286 nm is about 6 pm below the quantities from both the image simulations and the x-ray diffraction. The error within this method will be discussed in the following.

The error of the CCD camera discretization is of 0.287 % for the acquired NSCI image, i.e. for the value of 0.012826 nm per pixel. After the integration the peaks are plotted and a quadratic fit with subpixel accuracy is applied as described above. The fitting data for such a peak are examplary shown together with the coefficients of the quadratic function and their standard deviations in figure 5.16 (a). From this fit function the peak maximum is estimated and from the standard deviations of the coefficients the total error for the peak maximum is derived with Gauss law of error propagation to ~ 0.35 %, and thus for the peak distance to ~ 0.5 %.

These values are used to estimate an averaged spacing by fitting a Gauss function onto the experimentally obtained atomic column distances for the plot in figure 5.15 (f). The standard deviations for the coefficients are estimated and the width for the 95 % confidence band is calculated to 11.5 pm so the total error of the spacings is 6 pm as can be seen from the data in figure 5.16 (b).

This error is still one order larger than the error from the x-ray diffraction experiments but the spacings are estimated locally from the NCSI images of the interfaces and are not averaged over large areas.

5.9 Long-period undulations

Another striking feature in the lattice structure of the misfit compound $(PbS)_{1.14}NbS_2$ are wave-like undulations of the lattice along the incommensurate axis [84]. Those inhomogeneities can be found on parts of the samples and show characteristic properties:

- They are present directly next to areas where no such phenomenon exist.
- They show up very frequently within the different samples but not in every one.
- They cover areas of hundreds of nanometres on the sample.

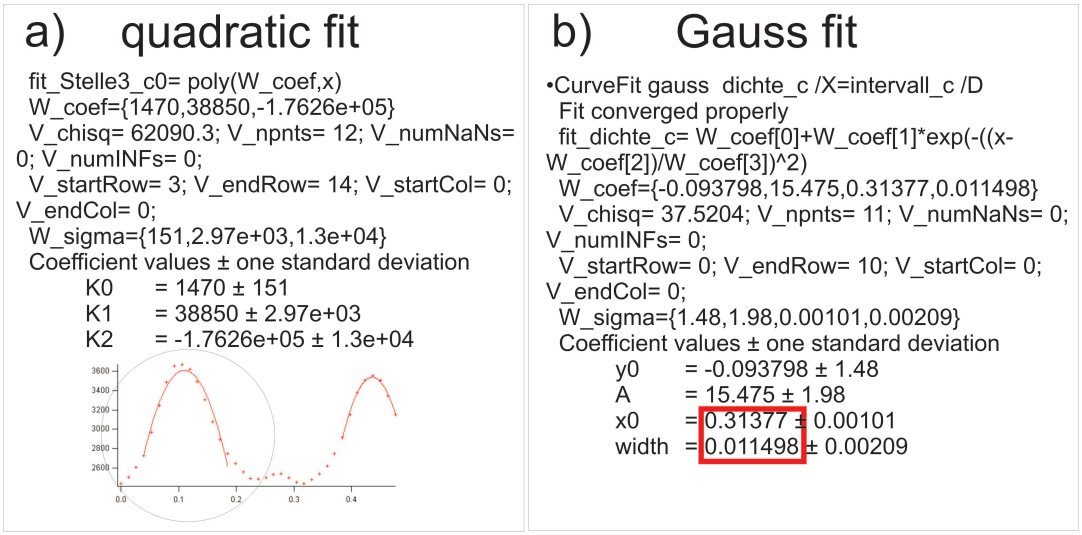

Figure 5.16: *(a) Example of fit parameters for subpixel accuracy quadratic fitting of a Pb/S column peak from an NCSI contrast image of* $(PbS)_{1.14}NbS_2$*. (b) Gauss fit applied to the c-spacing quantities. The mean value and 95 % confidence band width are highlighted in red.*

- They are exclusively present along the incommensurate axis.
- The undulations are highly uniformly with a constant periodicity.
- The rotation of the layers has a fixed angular range.
- The periodicity is a full order of magnitude larger than any lattice parameters of the supercell and from that the name *long-period undulations* is derived.

Figure 5.17 shows the HRTEM analysis of those highly periodic layer undulations in more detail: The electron diffraction pattern in figure (a) directly reveals this phenomenon by an angular broadening of the reflections of both the PbS and the NbS_2. The undulations span an angular range of $\sim 13°$ as is determined directly from the electron diffraction.

The undulation period of ~ 26 nm is determined from low magnification high-resolution images as the one in 5.17 (b). The bending of the layers and thus the wave-like shape is clearly visible here, although the atomic columns are not resolved.

This is the case for the NCSI contrast image in figure 5.17 (c), where the atom columns at the incommensurate interfaces within the undulations are visible. The diffractogram (in the inset) evaluated from the HRTEM image in (c) confirms the undulations.

The driving forces behind this undulation forming should be of energetic nature, but it is hard to find evidence for that from the atom column structure. At least it is possible in this section to present two competing qualitative models for the deformations that must take place within the lattice structure of the unit cells while the undulations are formed.

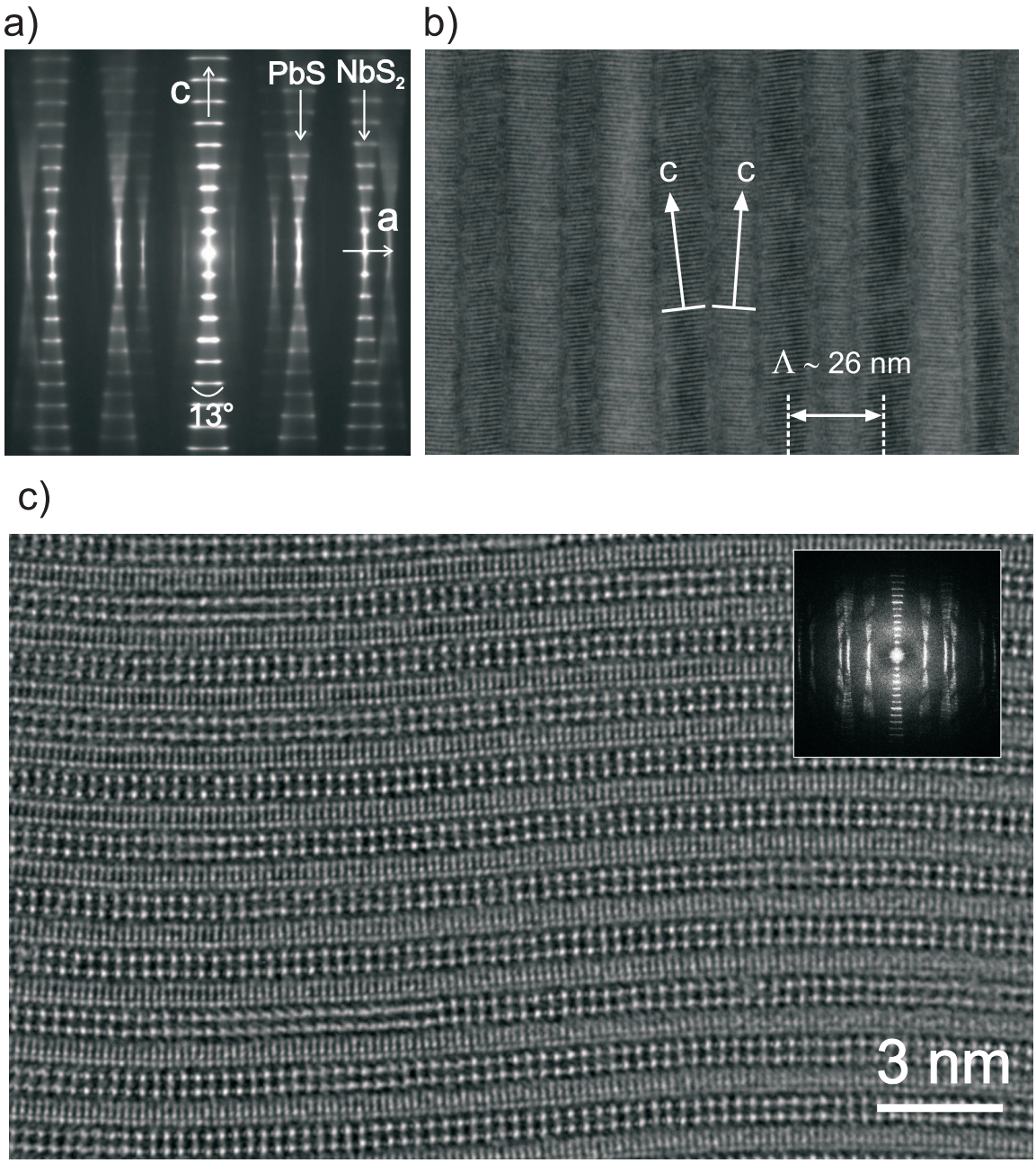

Figure 5.17: *Long-period undulations in* $(PbS)_{1.14}NbS_2$. *(a) Electron diffraction pattern along the commensurate direction showing an angular broadening of reflections due to a rotation of lattice planes in undulated layers. (b) Low-magnification HRTEM image taken at a thicker sample area revealing high uniformity of the undulations with a periodicity of* $\sim$ *26 nm. (c) NCSI contrast image of undulated layers taken with an aberration-corrected instrument at a rather thin sample area. The inset shows the diffractogram evaluated from that HRTEM-image.*

For the evaluations of the atom columns NCSI contrast images were used that show large areas of the undulations at the incommensurate interfaces. The pixel intensities of the images are then read out and loaded into a matrix as in figure 5.18 (a). It is then possible to draw contour plots and use a scale that assigns colors to intensity values to visualize the image intensities. Then an intensity threshold can be defined to separate the peaks from the background. This is demonstrated in figure 5.18 (b). Here the choosen threshold is sufficient enough to identify all intensity peaks (red) that are related to the atomic columns of the PbS subsystem. The atom column positions can then be determined from these peaks as schematically shown by the atoms drawn into the contour plot (c).

The rotation of the lattice planes can basically happen by two different kinds of modulations of the atomic configuration as illustrated by figure 5.19: (a) shows the undulation originating from a bending of the whole structure where the unit cell is arranged as on a ring with the fictional connection lines between the Pb/S columns in **c** direction point to the center of the ring and are not parallel anymore. That results into larger distance between the atom columns at the outer interface of the rotation while at the inner ring the columns close ranks.

Another possible modification of the structure is shown in figure 5.19 (b). Here all atom columns are arranged parallel to the **c** direction and are sheared towards each other.

As can be seen from the illustrations, a characteristic parameter is whether the connections in **c** direction between the atom columns are parallel or strife together. The atom column positions determined from the contour plots were then used and connecting lines between the atom columns are drawn as shown in figure 5.19 (c) + (d). Because the undulation has a frequency of 26 nm only a small section of the whole area is shown.

Nevertheless, it can be seen that the vast majority of connecting lines within the undulation is parallel and thus the unit cells are sheared towards each other in **c** direction, so the model 5.19 (b) describes the modulations of the atomic column positions satisfactorily.

5.10 Imaging along the [110]$_{PbS}$ axis: Individually resolving the Pb and S columns

It is not possible to estimate the distance between the Pb and S columns of the PbS subsystem in **c** direction from the NCSI contrast images in one of the three main zone axes that were already discussed.

From the x-ray diffraction data [13] it was determined that this distance should be around 53.5 pm as figure 5.20 illustrates. The schematic drawing on the left side shows the projected atomic columns along the commensurate direction and the distance values. As the experimental NCSI contrast image on the right shows, the Pb and S columns both contribute intensity to the same peak and the distance between the individual columns can not be estimated from that.

To resolve the individual columns it is necessary to image the lattice structure along a different zone axis where the projected Pb and S columns are not situated so close together. This zone axis is the [110]$_{PbS}$. The indexing indicates that this zone axis exists

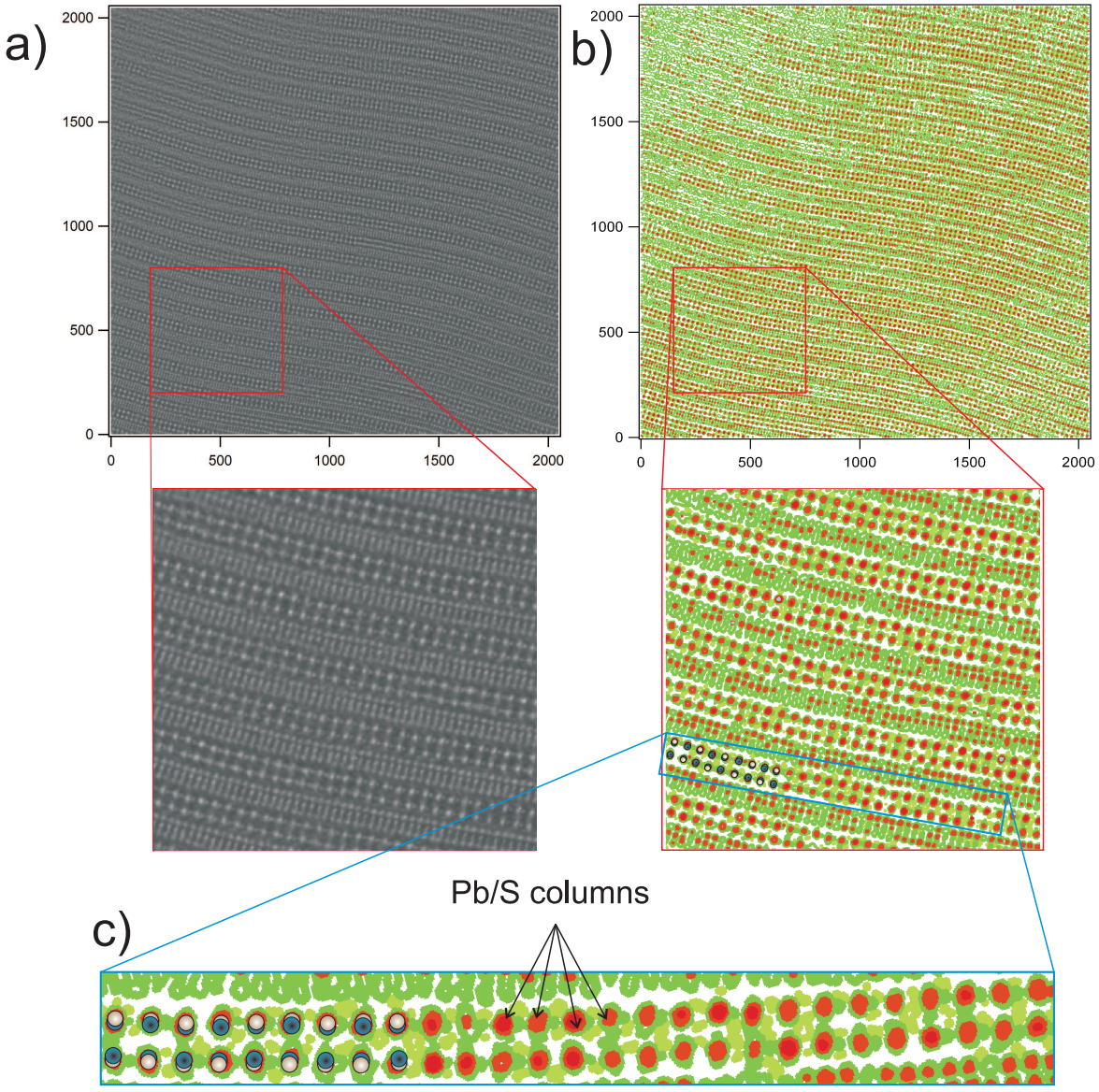

Figure 5.18: *Determination of the atom column positions at the incommensurate interfaces in the undulated areas of* $(PbS)_{1.14}NbS_2$. *An NCSI contrast image (a) is displayed as a contour plot (b) by visualising pixel intensity values as colors (here red is defined as intensity (counts)* $\geq$ *1500). The intensity peaks that belong to the atom columns of the PbS subsystem are then directly visible in the contour plot (c).*

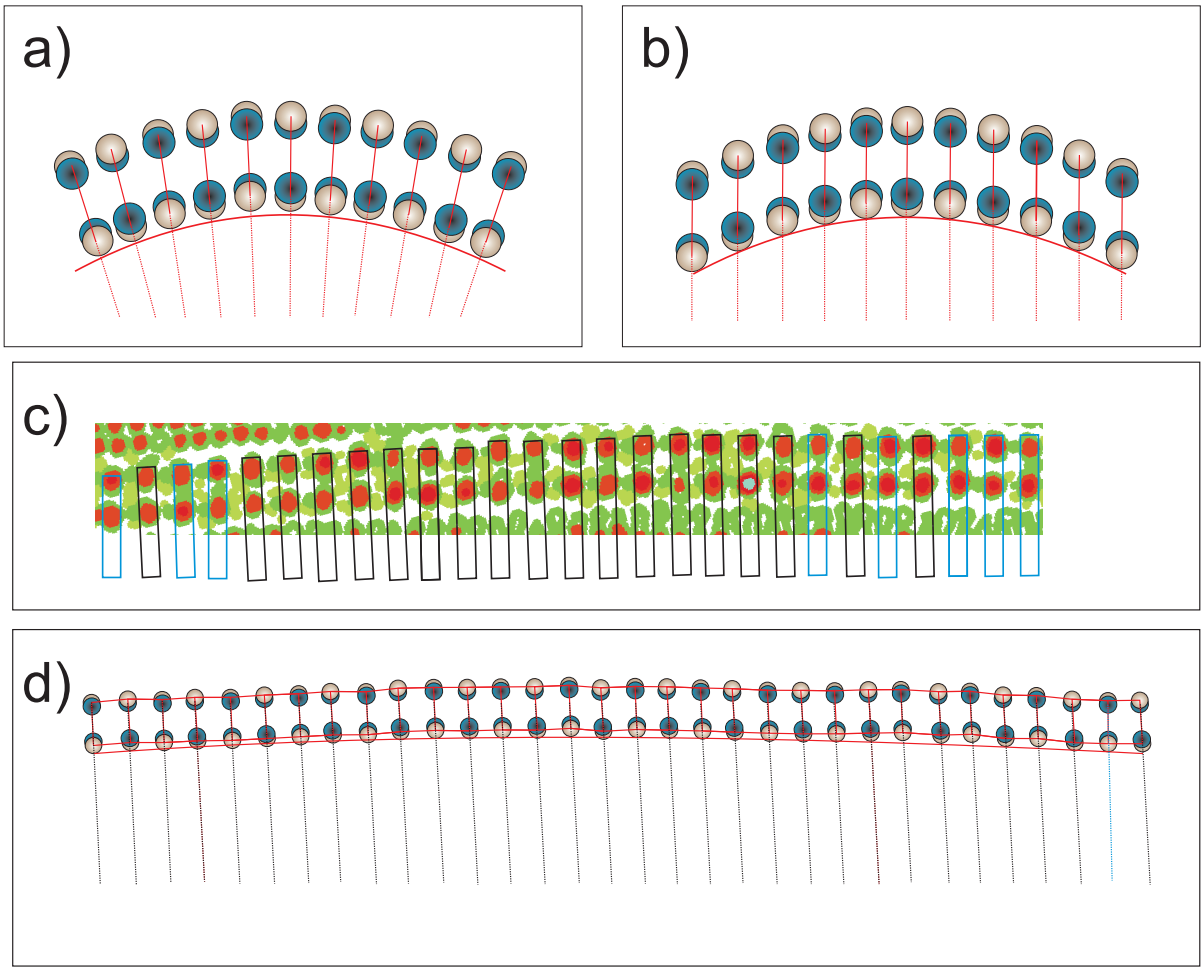

Figure 5.19: *Qualitative models describing the modification of the atom column positions in the unit cells of the PbS subsystem at the incommensurate interface within undulated areas of the misfit* $(PbS)_{1.14}NbS_2$*: (a) The rotation forces the atom columns to be arranged as on the surface of a ring. (b) The unit cell is sheared in* **c** *direction and the arrangement of the atom columns is still parallel. (c) + (d): The evaluation of atom column positions determined from experimental NCSI contrast images shows that nearly all atom columns are arranged as the model (b) predicts. Parallel arranged pairs of atom columns are connected with black boxes and lines, others with blue. It can be seen that the vast majority of atom column pairs is parallel arranged.*

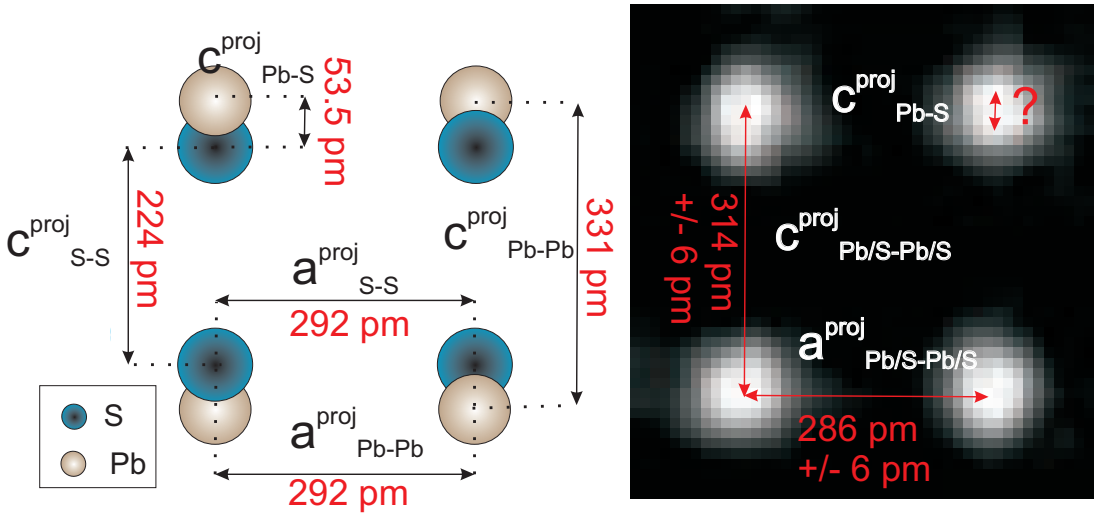

Figure 5.20: *Projected atom columns of the PbS subsystem within the misfit layered compound $(PbS)_{1.14}NbS_2$. The schematic drawing on the left side includes also the x-ray diffraction [13] derived distances. As can be seen from the enlarged part of an experimental HRTEM image on the right aquired under NCSI contrast imaging conditions, the distance between the Pb and S columns in* **c** *direction that should be 53.5 pm cannot be determined because the intensity from the individual S and Pb columns result in a single peak.*

only for the PbS subsystem, for the NbS_2 part this is no symmetry direction.

As Figure 5.21 shows schematically, this axis can be found by simply tilting the sample around 45°: The Pb and S columns that are in the projection along the commmensurate axis very close to each other (left) are separated after tilting of 45° (right image) and the protrusion of the Pb from the S columns can be estimated.

Unfortunately it is not possible to tilt the samples over angles as large as 45° within the microscope, so the samples have to be prepared in a way that the $[110]_{PbS}$ zone axis is near to the sample normal. This is achieved by cutting the initial crystals with an angle of 45° towards the incommensurate zone axis after they are glued between silicon and glass.

Before the experiment, multislice simulations along this zone axis were performed to study the contrast features that might appear in the experimental NCSI contrast images. Figure 5.22 shows a part of the simulated matrix with the thickness along y and the defocus along the x axis for a set of microscope parameters that will produce NCSI contrast at a defocus of 5.8 nm for the appropriate C_s value of $\sim$ -13 μm.

As the highlighted enlarged parts of the matrix demonstrate, it is possible to find pairs of defocus and thickness close to each other that result in very different image contrast: While for a thickness of 16.5 nm and a defocus of 9 nm the Pb atom columns are clearly much stronger in intensity than the S columns, at lower thicknesses and a defocus value only 2-3 nm closer to the NCSI contrast condition the S columns produce stronger contrast

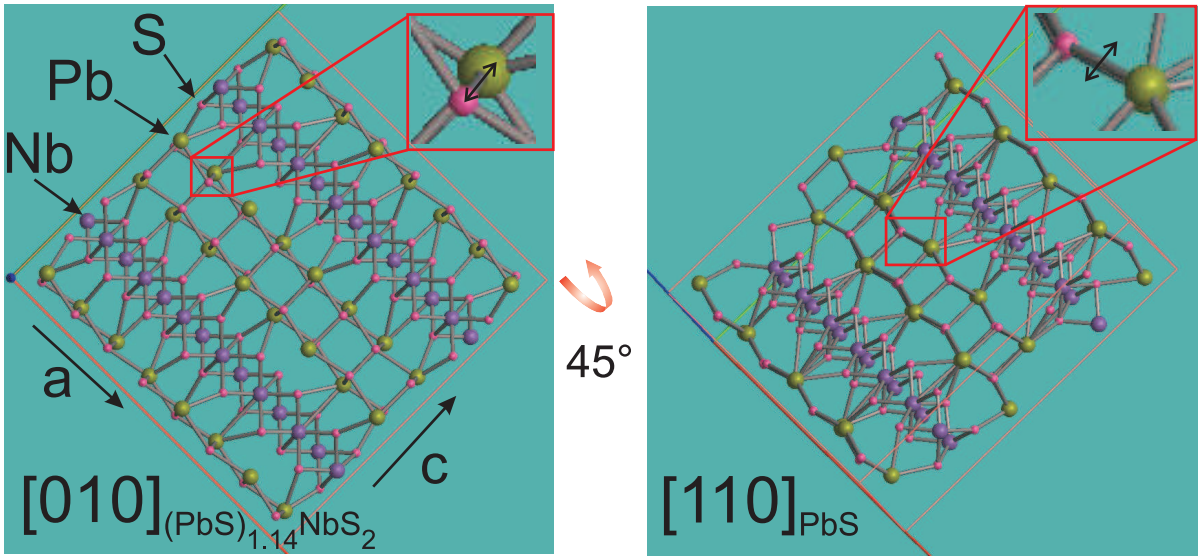

Figure 5.21: *Schematic drawings of the 45° tilting of a $(PbS)_{1.14}NbS_2$ supercell from the zone axis along the commensurate direction (left) to the $[110]_{PbS}$ axis (right) where the Pb and S columns of the PbS subsystem are clearly separated and the distances between them in the* **c** *direction can be estimated as the inset depicts.*

than the ones of the Pb. In addition, intensity artefacts occur as the green circle highlights that can easily be mistreated as atom column contrast.

An experimental NCSI contrast image from $(PbS)_{1.14}NbS_2$ in the $[110]_{PbS}$ zone axis is shown in figure 5.23. The contrasts in the right column ($Z = 6$ nm) of the simulations in figure 5.22 are compared with the experimental image in the inset. From that it can be judged that the thickness of the sample in the imaged region was about 6-9 nm. The Pb and S columns can be easily identified in the experimental image. The NbS_2 subsystem contributes only three rows of blurred contrast to the image intensity as expected because of the lack of a zone axis in the observed direction.

The overall quality of the NCSI images in this zone axis is clearly worse than for e.g. the images along the commensurate axis. This is most likely due to the more complicated sample preparation process and the strong presence of amorphous material on the samples after preparation that could not significantly be improved until now.

Nevertheless such NCSI images were used to estimate the distance between the Pb and S columns in **c** direction on a local scale, even though the precision might not be as good as e.g. for the evaluation of the tetragonal distortion and the error in the determination of the distance is expected to be higher.

For the distance determination a line perpendicular to the **c** direction was defined as shown in figure 5.24 (a). Then intensity profiles were taken from this line towards the individual peaks parallel to each other as shown in 5.24 (b). Those were plotted and fitted with quadratic functions and subpixel accuracy (figure 5.24 (c) + (d)). The distance from

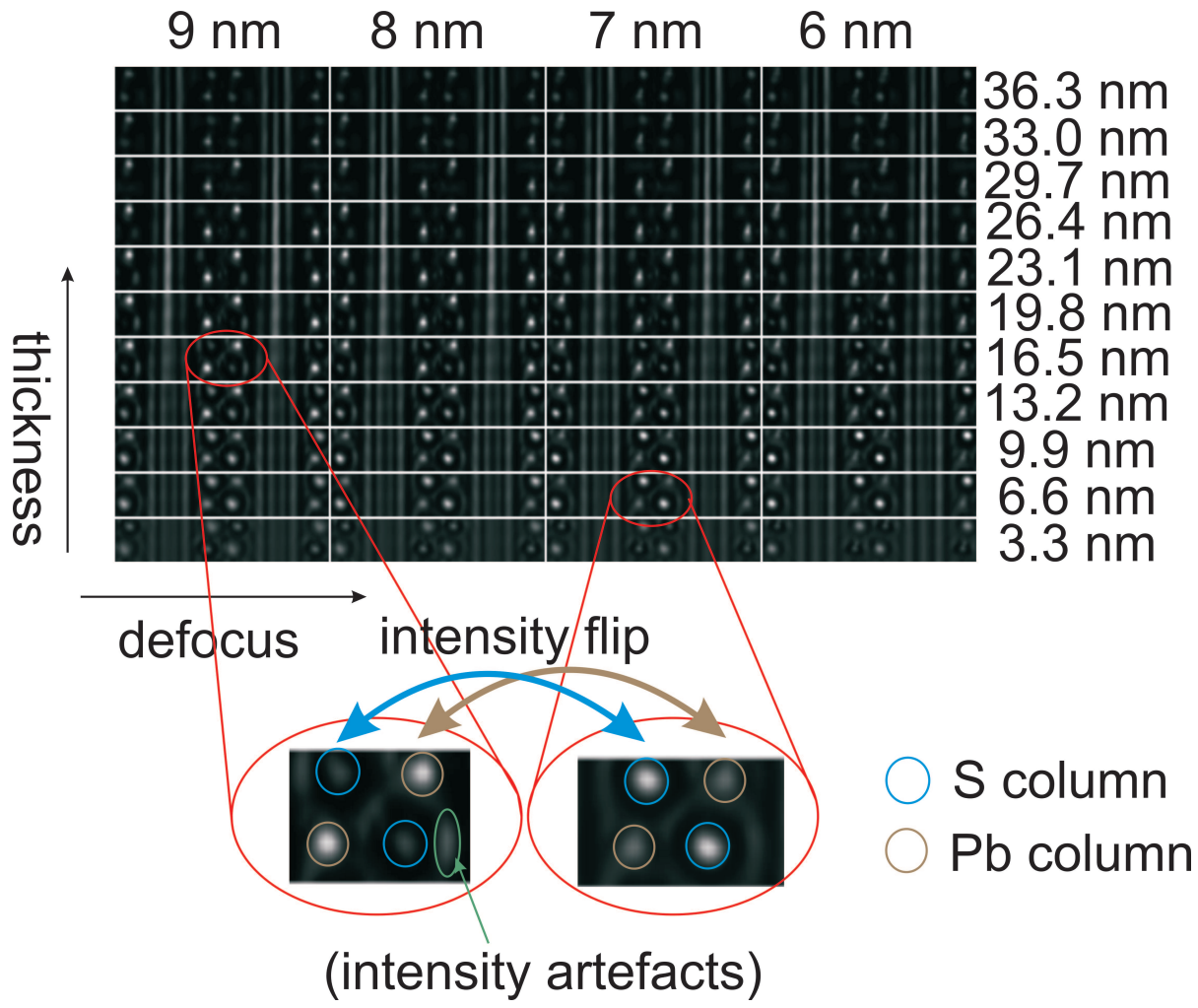

Figure 5.22: *Multislice simulation matrix for different values of defocus and sample thickness of the HRTEM image contrast of* $(PbS)_{1.14}NbS_2$ *in the* $[110]_{PbS}$ *zone axis. Simulation parameters are* $E = 300$ *kV,* $C_s = -13$ μ*m,* $\delta(Z) = 2.9$ *nm,* $\alpha = 0.2$ *mrad. The red circles highlight two sets of defocus and thickness values that produce clearly different intensities for the Pb and S columns respectively. For* $t = 16.5$ *nm and a defocus of 9 nm the Pb columns are much stronger in contrast than the S columns, while for 6.6 nm thickness and* $Z = 7$ *nm it is vice versa. As an example, an intensity artefact that does not indicate the position of an atomic column is highlighted by the green circle in the enlarged inset.*

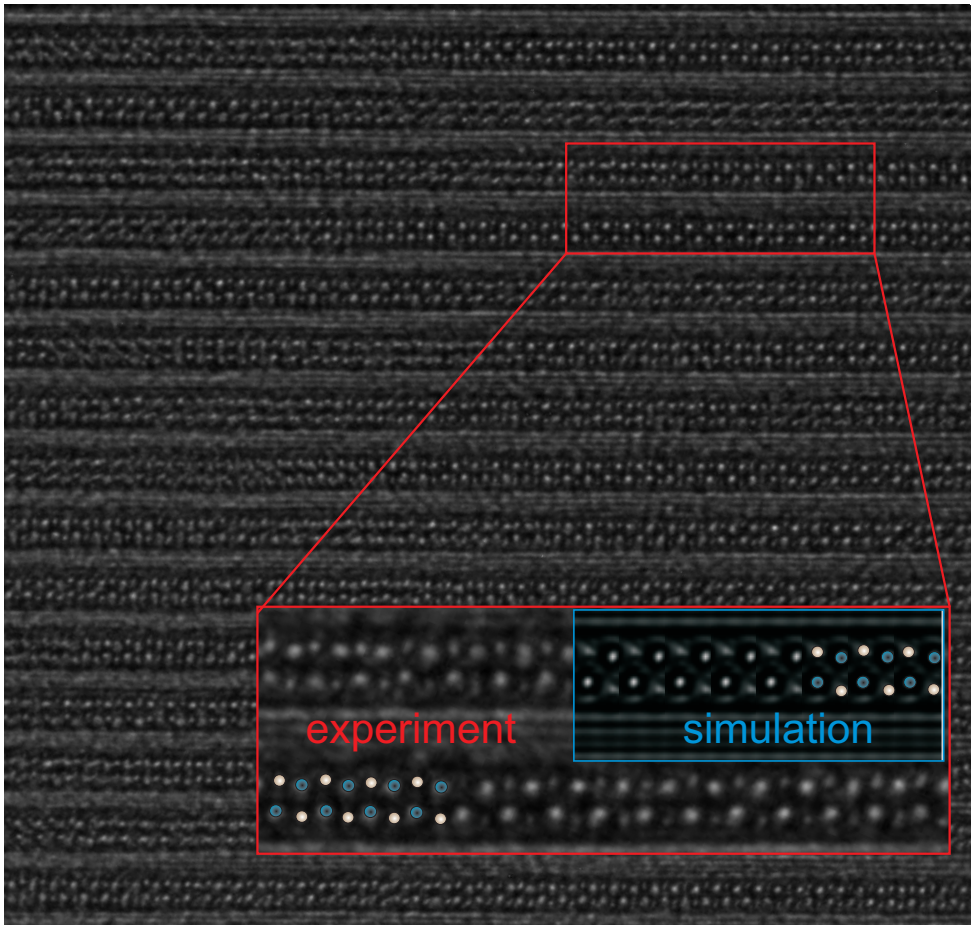

Figure 5.23: *NCSI contrast image of the misfit layered compound* $(PbS)_{1.14}NbS_2$ *along the* $[110]_{PbS}$ *zone axis. The Pb and S columns of the PbS subsystem are individually resolved as the enlarged inset clearly demonstrates by comparison with the multislice simulation.*

the line to the peak maximum is taken as the relative distance and by comparing those for more than 100 columns of Pb and S an average relative distance for both types of atomic columns can be calculated.

Due to the broad peaks the error for each fitted relative column distance is about 21 %. After that a Gauss curve is fitted to the relative distances of both columns as shown in figure 5.24 (e). The average distance for the S columns is 72 pm and the error (95% confidence interval) 38 %, i.e. 27 pm. For the Pb columns the relative distance is 110 pm ± 93 pm (85 %).

The absolute distance between the Pb and S columns in **c** direction is then 38 pm ± 35 pm. The error is large as expected from the quality of the single NCSI contrast images but the result is in agreement with the x-ray value of 53.5 pm.

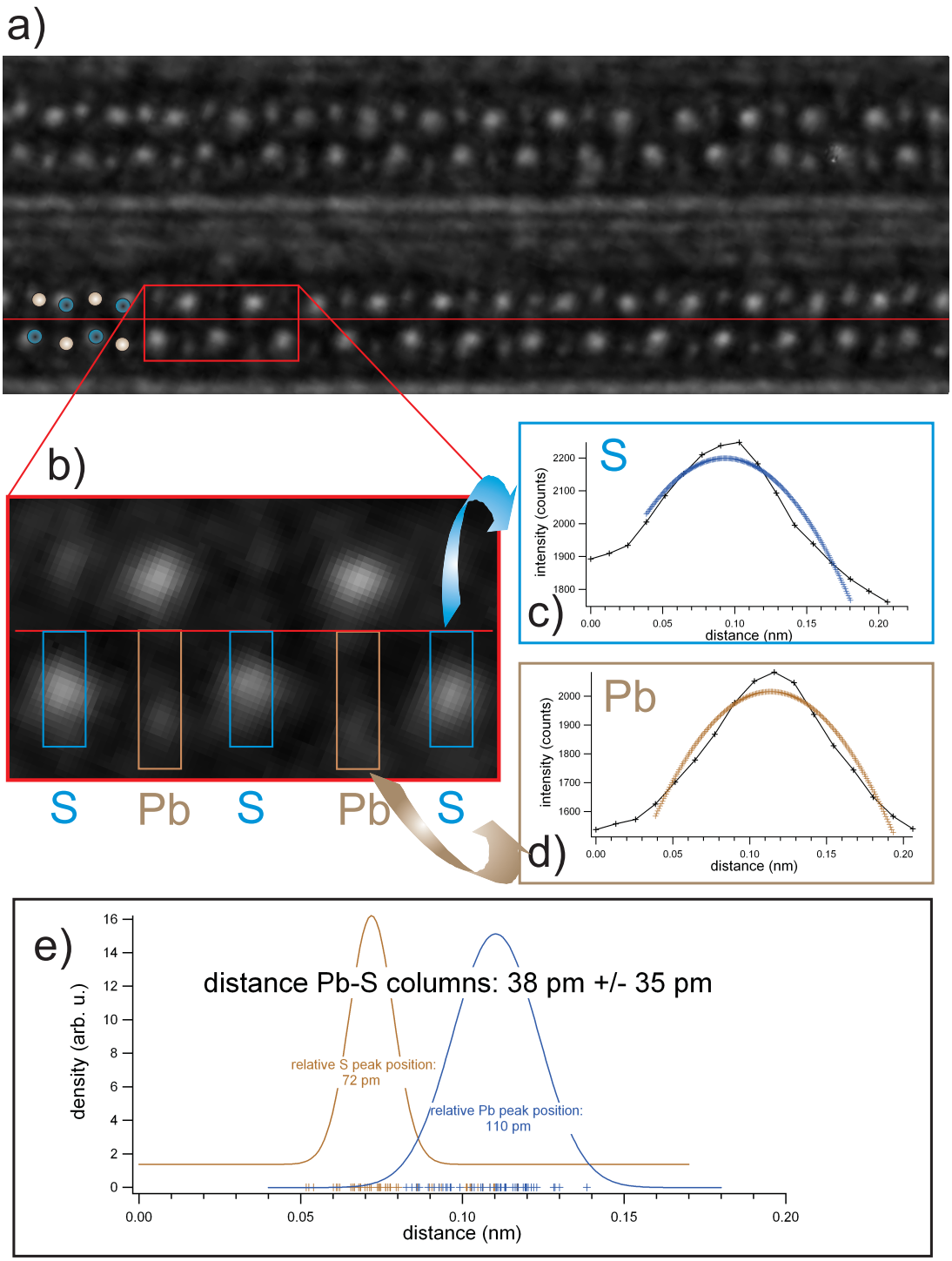

Figure 5.24: *Determination of the distance between the Pb and S columns in* **c** *direction of the misfit layered compound* $(PbS)_{1.14}NbS_2$ *with the help of HRTEM NCSI contrast images taken along the* $[110]_{PbS}$ *zone axis: A line perpendicular to the* **c** *direction is defined (a) and profiles along the peaks are drawn (b). The maxima are fitted with subpixel accuracy ((c) + (d)) for more than 100 peaks. The averaged relative distances are then estimated (f) to calculate the total distance between the Pb and S columns.*

Chapter 6

Discussion

6.1 Methodological aspects of the HRTEM experiments

Electron diffraction

The electron diffraction results (chapter 5.1, table 5.1) show that the sample structure corresponds well on the average to the structure of misfit compound crystals of nominally same composition as obtained from lattice parameter measurements using x-ray diffraction [13]. Although x-ray diffraction as a technique averaging over large sample volumes is in general much more precise, the lattice parameters determined from the reflection distances in the EDPs fit to the x-ray data with an error of less than 2%.

The electron diffraction pattern give hints on inhomogeneities within the crystal lattice like the streaking of the reflections along the commensurate axis (fig. 5.3) that is explained by stacking disorder and will be discussed in chapter 6.2.

Conventional and aberration-corrected HRTEM imaging

By comparing conventional experimental images along the commensurate direction of the misfit layered compound $(PbS)_{1.14}NbS_2$ recorded with a Tecnai F30 S-Twin HRTEM instrument with multislice simulations (fig. 4.7 (a)), the contrast features predicted by the simulations can be experimentally confirmed. They clearly show no easy accordance with the real structure as depicted by the inset that demonstrates, that atomic column positions are not represented by intensity maxima. It is not possible for any combinations of defocus and thickness values to achieve contrast where the intensity maxima directly represent the atom columns of the crystal. The origin for that is the huge image delocalization.

Figure 5.7 (b) shows an experimental aberration-corrected HRTEM image along the same zone axis recorded with the Titan 80-300 kV (left) and the appropriate multislice simulation (right). The inset of the projected atomic configuration shows that the resulting image intensity peaks correspond directly to the atom columns of the lattice structure. The experimental image reproduces this contrast due to the strongly surpressed delocalization, like the bright intensity maxima that represent the atomic columns, very well.

These observations are the basic motivation of using the method of NCSI contrast imaging for the investigation of the interfaces of the misfit layered compound crystal.

NCSI contrast imaging

By using the NCSI technique it is demonstrated that the obtained experimental images reveal the projected crystal potential and thus the atom columns along the interfaces directly in real space (fig. 5.8). As opposed to electron diffraction pattern or x-ray diffraction experiments one can gain information about lattice constants, structure modulations or inhomogeneities on a local scale. X-ray diffraction techniques are really powerful in terms of accuracy, but lack any local information because they average over very large areas in contrast to HRTEM images.

The image in figure 5.8 that shows an area of about 20 nm × 20 nm along the commensurate direction of $(PbS)_{1.14}NbS_2$ demonstrates that the weakly scattering S columns are individually resolved even in close distance to the more strongly scattering Pb and Nb columns. The local position of atom columns and thus lattice parameters can be determined with high precision from such images which demonstrates the advantage of the NCSI contrast imaging technique over the spatially averaging x-ray diffraction experiments.

Focal series and reconstruction of the exit-plane wave function

The focal series recorded with a conventional HRTEM (Tecnai F 30) along the commensurate direction of $(PbS)_{1.14}NbS_2$ (fig. 5.10) shows complicated contrast behaviour in every single image. The layers can be resolved, but the NbS_2 subsystem cannot be identified from the contrast in any of the images. The reconstructed phase of the exit-plane wave function reveals more details about the atom column configuration. Although the NbS_2 sublayers are not resolved, one can clearly identify the PbS atom columns.

By studying the contrast features of experiment and simulation for a focal series recorded with an aberration-corrected HRTEM (fig. 5.11), one can find a very good overall agreement between experiment and simulation. The strongest contrast under such conditions, is predicted for the defocus of 6 nm very close to the NCSI contrast condition which is confirmed by both experiment and simulation. The configuration of the atom columns at the interfaces can be examined very well.

In conclusion, the benefits of tuning the spherical aberration to negative values for NCSI contrast producing conditions are convincingly demonstrated by such a defocal series of our complex crystal system (figure 5.11). The simulations predict the experimental image contrasts very well.

The effect of amorphous material (on the top and bottom of the sample) on the accuracy of determining atom column positions from restored exit waves was by [87] found to be the most important factor (compared with other influences as e.g. noise or the restoration method within the reconstruction itself) that limits the reliability of atomic column position estimations. Figure 5.12 demonstrates this effect by comparing

the reconstructed phase image of the exit-plane wave function and the NCSI contrast image from within the series.

Plan-view imaging

The plan-view images show huge differences in the experimental contrast (fig. 5.5). This could be explained by abrupt changes in the sample thickness due to the preparation method. The contrast behaviour is confirmed by multislice simulations. In the images periodic intensity modulations occur (fig. 5.6) that have their origin in the incommensurabillity of the misfit compound.

The atomic columns could not be resolved even with NCSI contrast imaging in the plain-view projection direction as was expected: Figure 5.1 (a) illustrates that the atomic column distances are often far below 0.8 Ångstrom, which is the information limit of the Titan.

Conventional Z-contrast imaging

Although the fourfold symmetry of the PbS subsystem is visible in the images (fig. 5.4), the contrasts are strongly blurred in the HAADF STEM images. From the NbS_2 subsystem which has much shorter interatomic distances, only the Nb part is resolved as bright intensity lines. This was expected, as the S has a far smaller atomic number Z. The Z-contrast images were one of the first ever taken with this instrument whose parameters were not yet characterized. The images leave room for further improvements in resolution, as the nominal resolution of the microsope is about 0.17 nm.

6.2 Quantitative HRTEM results: The misfit layered compound $(PbS)_{1.14}NbS_2$

Stacking disorder

The result that stacking disorder exists in the $(PbS)_{1.14}NbS_2$ misfit system was assumed at first from the electron diffraction patterns that deliver information averaged over a larger volume of the sample. As the NCSI contrast image in figure 5.14 shows by resolving the atomic column configuration at the incommensurate interfaces it can be locally observed that this is indeed the case.

The fact that the PbS double layers are stacked in an unordered way inside of the van-der-Waals gaps of the NbS_2 in the incommensurate direction as if it is neither aligned to the NbS_2 lattice nor the next adjacent PbS slabs supports the picture of the transition metal dichalcogenide being the host crystal and the PbS as a whole the intercalated guest. This is in line with the predictions of intercalation of the whole subsystem from [8].

Tetragonal distortion

The tetragonal distortion, that describes the compression of the originally cubic rock-salt structure of the PbS to be stronger along the **a** than along the **c** axis can be directly measured with experimental NCSI contrast images (fig. 5.15). The protrusion of the Pb columns within the PbS can be determined from the imaging along the $[110]_{PbS}$ axis that separates the S and Pb columns.

The intensity maximum shift due to the overlapping of the Pb and S columns in the **c**-direction is very accurately reproduced by the experimental data (fig. 5.15)). The spacing in **a** direction lies within the error tolerance of 6 pm (fig. 5.15).

The comparison with the values obtained for this misfit layered compound system from x-ray diffraction experiments [13] shows that local measurements of atomic column distances agree well with the average values obtained from x-ray experiments.

Long-period undulations

The HRTEM analysis with NCSI contrast images of the new phenomenon of highly periodic layer undulations (fig. 5.17) along the incommensurate interface direction of $(PbS)_{1.14}NbS_2$ reveals both quantitative and qualitative informations. The undulations span an angular range of $\sim 13°$ and the undulation period of ~ 26 nm is determined.

While the exact reason for the period length is still uncertain, the vast majority of unit cells is sheared along the **c** direction (fig. 5.19) to form the undulations. Further investigations should concentrate on the origin of the undulations.

Imaging along the $[110]_{PbS}$ axis: Individually resolving the Pb and S columns

To resolve the individual Pb and S columns of the PbS subsystem it is necessary to image the lattice structure along a zone axis where the projected Pb and S columns are not situated directly beneath each other. NCSI contrast imaging was therefore performed along the $[110]_{PbS}$ zone axis (fig. 5.23) and the individual atom columns with a spacing of nominally 53 pm were indeed individually resolved.

The overall quality of the NCSI contrast images in this zone axis is not as good as the images along the commensurate axis, as the broad intensity peak maxima depict. Nevertheless, the absolute distance between the Pb and S columns in **c** direction is determined (fig 5.24) and in good agreement with the x-ray diffraction derived value. There it can be concluded it is worth trying to improve the preparation for this and other zone axes to gain even more precise structure informations.

On the accuracy of atom column determination and site occupany

The highest accuracy in atom column position determination from aberration-corrected HRTEM images so far is about 3-5 pm [5] for exit-plane reconstructions and NCSI images. Our statistical error for the determination of the tetragonal distortion is 6 pm and thus

very close to that. It becomes worse when too much amorphous material disturbs the NCSI imaging (35 pm for the determination of the Pb-S distance) [87].

Amorphous material affects also strongly the possibility of site occupancy determinations from peak intensities. Whether an exchange of metal atoms between the NbS_2 and the PbS subsystems as found by [91] has a measurable influence on the column intensity in NCSI contrast images is therefore not predictable without simulations including the effect of the amorphous layers. The simulations should also use the correct Debye-Waller factors for the system determined with DFT calculations to yield the correct image contrast [86]. This will be a task for the future.

Chapter 7

Summary and conclusions

Experimental HRTEM and multislice simulations were applied to study the lattice structure and the atomic configuration at the incommensurate interfaces of the misfit layered compound $(PbS)_{1.14}NbS_2$.

Ultra-thin samples were prepared for HRTEM using different preparation techniqes for plan-view and cross-section examinations.

Lattice parameters of the misfit compound were determined from electron diffraction along the crystallographic directions [001], [010] and [100] and compared with x-ray diffraction data to characterize the crystal structure (chapter 5.1).

The effect of image delocalization for both conventional (Tecnai F 30) and aberration-corrected (Titan T) HRTEM was demonstrated by comparison of experimental images and multislice simulations.

It could be demonstrated that NCSI contrast imaging is capable of resolving the Pb, S and Nb columns (by imaging along the zone axes [010] and $[110]_{PbS}$) along the interfaces within the misfit layered compound individually, although they are situated directly beneath each other and differ significantly in their scattering strength.

Exit-plane wave reconstruction was performed on focal series recorded with both the Tecnai and Titan microscopes. The reconstructed phases were not favorable in resolution when compared to the NCSI contrast images due to the effect of amorphous material [87].

Experimental NCSI contrast imaging with the aberration-corrected HRTEM was applied to resolve the atomic configuration at the incommensurate interfaces of the misfit compound. Several lattice modifications and inhomogeneities were described in detail and quantitativly characterized, in particular:

- stacking disorder of the PbS;
- tetragonal distortion within the PbS subsystem;
- long-period undulations of the whole misfit lattice;

The best statistical accuracy reached in atomic column distance determination was calculated to 6 pm (see chapter 5.8).

It was possible to resolve the individual Pb and S columns of the PbS subsystem in a zone axis with an angle of 45° towards the commensurate one.

The misfit layered compound $(PbS)_{1.14}NbS_2$ hosts several lattice structure modifications and inhomogeneities at the incommensurate interfaces. Phenomena like the stacking disorder or the long-period undulations were until now not described or quantitatively determined in the literature. The tetragonal distortion was measured directly with local atom column positions for the first time.

HAADF-STEM was applied for Z-contrast imaging. The layered structure along the commensurate axis and the PbS subsystem as well as the Nb could be resolved but there is still room for improvement.

In conclusion, the aberration-corrected HRTEM and in particular the NCSI contrast imaging technique along with multislice simulations is perfectly applicable to study the complex atomic structure along the incommensurate interfaces of the misfit layered compound $(PbS)_{1.14}NbS_2$. The statistical error of the local atom column position determination for quantitative lattice structure analysis was determined to 6 pm, which is comparable to the accuracy reported in the newest literature (3-5 pm) [5].

Bibliography

[1] O. Scherzer: *The Theoretical Resolution Limit of the Electron Microscope*, J. Appl. Phys. **20**(1), 20 (1948).

[2] H. Rose: *Outline of a spherically corrected semiaplanatic medium-voltage transmission electron microscope*, Optik **85**, 19 (1990).

[3] M. Haider, H. Rose, S. Uhlemann, E. Schwan, B. Kabius, K. Urban: *A spherical-aberration-corrected 200 kV transmission electron microscope*, Ultramicroscopy **75**, 53 (1998).

[4] M. Lentzen: *Contrast Transfer and Resolution Limits for Sub-Ångström High-Resolution Transmission Electron Microscopy*, Microscopy and Microanalysis **14**, 16-26, (2008).

[5] K. Urban: *Studying Atomic Structures by Aberration-Corrected Transmission Electron Microscopy*, Science **321**, 506-510, (2008).

[6] C. L. Jia, M. Lentzen and K. Urban: *Atomic-Resolution Imaging of Oxygen in Perovskite Ceramics*, Science **299**, 870 (2003).

[7] J.A. Wilson and A.D. Yoffe: *The transition metal dichalcogenides. Discussion and interpretation of the observed optical, electrical and structural properties*, Adv. Phys. **18**, 192 (1969).

[8] J. Rouxel: *Intercalated Layered Materials*, ed. F. A. Lévy, (1979).

[9] G. A. Wiegers and A. Meerschaut: *Misfit Layer Compounds* $(MS)_nTS_2$ *(M = Sn, Pb, Bi or rare earths; T = Nb, Ta, Ti, V, Cr;* $1.08 < n < 1.23$*) Structures and Physical Properties*, Mat. Sci. For. 100 - 101, 101 - 172 (1992).

[10] W. Sterzel and J. Horn: *Thiotitanat, Thiozirkonat und Thiohafnat des Bleis mit der Zusammensetzung* $PbMe^{IV}S_3$, Z. Anorg. Chem. **376**, 254 (1970).

[11] L. Schmidt: *Superconductivity in* $PbNbS_3$ *and* $PbTaS_3$, Physics Letters **31** (1970).

[12] L. Schmidt, S. L. McCarthy and J. P. Maita: *Superconductiong Behaviour of the System* $Pb(Nb_{1-x}Ta_x)S_3$, Solid State Commun. **8**, 1513f (1970).

[13] G. A. Wiegers, A. Meetsma, R. J. Haange, S. van Smaalen, J. L. de Boer: *The incommensurate misfit layer structure of* $(PbS)_{1.14}NbS_2$*, 'PbNbS*$_3$*' and* $(LaS)_{1.14}NbS_2$*, 'LaNbS*$_3$*': an X-ray diffraction study*, Acta Cryst. B textbf46, 324 (1990).

[14] S. Kuypers and J. Van Landuyt: *Electron Microscopy Study Of Incommensurate Intergrowth Structures "*MTS_3*"*, Materials Science Forum Vols. 100 & 101, pp 223 - 272 (1992).

[15] E. Spiecker, M. Garbrecht, C. Dieker, U. Dahmen, W. Jäger: *High resolution TEM and diffraction study of layer stacking and long-period undulations in the incommensurate misfit layer compound* $(PbS)_{1.14}NbS_2$, Microsc. and Microanal. **13** (Suppl. 3), 424, 2007.

[16] M. Garbrecht, E. Spiecker, W. Jäger, K. Tillmann: *Aberration-corrected HRTEM of the incommensurate misfit layer compound* $(PbS)_{1.14}NbS_2$, MRS Proceedings Volume 1026E "Quantitative Electron Microscopy for Materials Science", eds. E. Snoeck, R. Dunin-Borkowski, J. Verbeeck, and U. Dahmen, 1026-C10-01, 2007.

[17] German Research Foundation project DFG SP 648/2-1: *Microscopic Characterization of Incommensurate Interfaces in Modulated Misfit layer compounds by Ultra-High Resolution TEM.*

[18] DFG FOR 353/1-2: *Surface and Interface Phenomena of TMDC Layered Crystals.*

[19] Max T. Otten and Wim M. J. Coene: *High-resolution imaging on a field emission TEM*, Ultramicoscopy **48**, 77 (1993).

[20] P. A. Stadelmann: *EMS - a software package for electron diffraction analysis and HREM image simulation in materials science*, Ultramicoscopy **21**, 131 (1987).

[21] E. J. Kirkland: *Improved high resolution image processing of bright field electron micrographs: I. Theory*, Ultramicoscopy **15**, 151 (1984).

[22] W. Coene, G. Janssen, M. Op de Beeck and D. Van Dyck: *Phase retrieval through focus variation for ultra-resolution in field-emission transmission electron microscopy*, Phys. Rev. Lett. **69**, 3743 (1992).

[23] D. Gabor: *Microscopy by Reconstructed Wave-Fronts*, Proc. Roy. Soc. Ser. A **197**, 454 (1949).

[24] H. Lichte: *Parameters for high-resolution electron holography*, Ultramicoscopy **51**, 15 (1993).

[25] H. Bethe: *Theory of the diffraction of electrons in crystals*, Ann. Phys. **87**, 55 (1928).

[26] C. J. Humphreys: *The scattering of fast electrons by crystals*, Rep. Prog. Phys. **42**, 1864 (1979).

[27] J. M. Cowley and A. F. Moodie: *The scattering of electrons by atoms and crystals. I. A new theoretical approach*, Acta Cryst. **10**, 609 (1957).

[28] P. Goodman and A. F. Moodie: *Numerical Evaluation of N-Beam Wave Functions in Electron Scattering by the Multi-slice Method*, Acta Cryst. A **30**, 280 (1974).

[29] J. C. H. Spence, *Experimental High Resolution Electron Microscopy*, Oxford University Press, New York, Oxford (1988).

[30] G. H. Smith and R. E. Burge: *The analytical representation of atomic scattering amplitudes for electrons*, Acta Cryst. **15**, 182 (1962).

[31] P. A. Doyle and P. S. Turner: *Relativistic Hartree-Fock X-ray and electron scattering factors*, Acta Cryst. A **24**, 390 (1968).

[32] F. Zernike: *Phase contrast, a new method for the microscopic observation of transparent objects*, Physica **9**, 686 (1942).

[33] F. Zernike: *Phase contrast, a new method for the microscopic observation of transparent objects, part II*, Physica **9**, 974 (1942).

[34] H. Lichte: *Optimum focus for taking electron holograms*, Ultramicroscopy **38**, 13 (1991).

[35] M. Knoll and E. Ruska: *Das Elektronenmikroskop*, Z. Physik **78**, 318 (1932).

[36] O. Scherzer: *Über einige Fehler von Elektronenlinsen*, Z. Physik **101**, 593 (1936).

[37] O. Scherzer: *Sphärische und chromatische Korrektur von Elektronenlinsen*, Optik **2**, 114 (1947).

[38] M. Haider, S. Uhlemann, E. Schwan, H. Rose, B. Kabius and K. Urban: *Electron microscopy image enhanced*, Nature **392**, 768 (1998).

[39] M Haider, G. Braunshausen and E. Schwan: *Correction of the spherical aberration of a 200 kV TEM by means of a Hexapole-corrector*, Optik **99**, 167 (1995).

[40] M. Lentzen, B. Jahnen, C. L. Jia, A. Thust, K. Tillmann and K. Urban: *High-resolution imaging with an aberration-corrected transmission electron microscope*, Ultramicroscopy **92**, 233 (2002).

[41] C. L. Jia, M. Lentzen and K. Urban: *High-resolution transmission electron microscopy using negative spherical aberration*, Microsc. Microanal. **10**, 174 (2004).

[42] C. L. Jia and K. Urban, *Atomic-Resolution Measurement of Oxygen Concentration in Oxide Materials*, Science **303**, 2001 (2004).

[43] A. Thust, *Foacal-series reconstruction*, Matter and materials **34**, Forschungszentrum Jülich GmbH (2007).

[44] P. Schiske: *Image reconstruction by means of focus series*, Journal of Microscopy **207**, 154 (2002).

[45] W. O. Saxton: *Correction of Artifacts in Linear and Nonlinear High Resolution Electron Micrographs*, J. Micros. Spectrosc. Electron. **5**, 665 (1980).

[46] W. O. Saxton: *What is the focus variation method? Is it new? Is it direct?*, Ultramicroscopy **55**, 171 (1994).

[47] A. Thust, W. M. J. Coene, M. Op de Beeck and D. Van Dyck: *Focal-series reconstruction in HRTEM: simulation studies on non-periodic objects*, Ultramicroscopy **64**, 211 (1996).

[48] R. W. Gerchberg, W. O. Saxton: *A practical algorithm for the determination of the phase from image and diffraction plane pictures*, Optik **35**, 237 (1972).

[49] D. L. Misell: *An examination of an iterative method for the solution of the phase problem in optics and electron optics: I. Test calculations*, J. Phys. D: Appl. Phys. **6**, 2200 (1973).

[50] L. J. Allen, M. P. Oxley: *Phase retrieval from series of images obtained by defocus variation*, Optics Communications **199**, 65 (2001).

[51] A. Thust, M. Lentzen, K. Urban: *Non-linear reconstruction of the exit plane wave function from periodic high-resolution electron microscopy images*, Ultramicroscopy **53**, 101 (1994).

[52] A. Thust, M. H. F. Overwijk, W. M. J. Coene, M. Lentzen: *Numerical correction of lens aberrations in phase-retrieval HRTEM*, Ultramicroscopy **64**, 249 (1996).

[53] M. von Ardenne: *Das Elektronen-Rastermikroskop. Theoretische Grundlagen*, Z. für Physik **109**, 553, 1938.

[54] A. V. Crewe, J. Wall, L. M. Welter: *A High-Resolution Scanning Transmission Electron Microscope*, J. Appl. Phys. **39**, 5861, 1968.

[55] A. V. Crewe, J. Wall, J. Langmore: *Visibility of Single Atoms*, Science **168**, 1338, 1970.

[56] M. M. J. Treacy, A. Howie, C. J. Wilson: *Z contrast of platinum and palladium catalysts*, Phil. Mag. A **38**, 569, 1978.

[57] A. Howie: *Image contrast and localised signal selection techniques*, J. Microscopy **117**, 11, 1979.

[58] Z. L. Wang: *Elastic and Inelastic Electron Scattering in Electron Diffraction and Imaging*, Plenum Press, New york, 1995.

[59] S. J. Pennycook, L. A. Boatner: *Chemically Sensitive Structure Imaging with a Scanning Transmission Electron Microscope*, Nature, **336**, 565, 1988.

[60] E. J. Kirkland: *Advanced Computing in Electron Microscopy*, Plenum Press, New york, 1998.

[61] D. E. Jesson, S. J. Pennycook: *Incoherent Imaging of Thin Specimens Using Coherently Scattered Electrons*, Proc. Roy. Soc. A **441**, 261, 1993.

[62] P. Hartel, H. Rose, C. Dinges: *Conditions and reasons for incoherent imaging in STEM*, Ultramicroscopy **63**, 93, 1996.

[63] R. H. Friend, A. D. Yoffe: *Electronic properties of intercalation complexes of the transition metal dichalcogenides*, Adv. Phys. **36** 1 (1987).

[64] M. Inoue, H.P. Hughes und A. D. Yoffe : *The electronic and magnetic properties of the 3d transition metal intercalates of* TiS_2, Advances in Physics **38**, (5) 565 (1989).

[65] G. V. Subba Rao und M. W. Shafter: *Intercalation in Layered Transition Metal Dichalcogenides*, Intercalated Layered Material, ed. F. A. Lévy, (1979).

[66] G. Allan: *Surface core-level shifts and relaxation of group-IVA-element chalcogenide semiconductors*, Phys. Rev. B **43**, 9594 (1991).

[67] W. Hoffmann: *Ergebnisse der Strukturbestimmung komplexer Sulfide*, Z. Kristallogr. **92**, 161 (1935).

[68] Nimitz, *Lanoldt-Börnstein*, **vol. III**, (Springer, Berlin), p. 17f, (1983).

[69] W. Albers, C. Haas, H. J. Vink, J. D. Wasscher: *Investigations on SnS*, J. Appl. Phys. **32**, 2220 (1961).

[70] J. A. Leiro, K. Laajalehto, I. Kartio, M. H. Heinonen, *Surface core-level shift and phonon broadening in PbS(100)*, Surf. Sci. **412/413**, (1998).

[71] I. G. Batyrev, L. Kleinman: *Rumpled relaxation and surface core-level shift in PbS(001)*, Phys. Rev. B **70**, 073310 (2004).

[72] T. Grandke, M. Cardona: *Electronic Properties of Clean and Oxygen Covered (100) Cleaved Surfaces of PbS*, Surf. Sci. **92**, 385 (1980).

[73] B. M. Trafas, I. M. Vitomirov, C. M. Aldao, Y. Gao, F. Xu, J. H. Weaver: *Cr, Co, Pd, Au, and In overlayers on PbS(100): Adatom interactions and interface formation*, Phys. Rev. B **39**, 3265 (1989).

[74] F. Cerrina, R. R. Daniels, V. Fano: *Inversion layers at PbTe interfaces*, Appl. Phys. Lett. **43**, 182 (1983).

[75] J. Wulff, A. Meetsma, S. van Smaalen, R. J. Haange, J. L. de Boer, G.A. Wiegers: *Determination of the modulated structure of the inorganic misfit layer compound* $(PbS)_{1.18}TiS_2$, J. Solid State Chem. **84**, 118 (1990).

[76] J. Brandt, *Geometric and electronic structure of misfit layered compounds and epitaxial thin films of PbS on transition metal dichalcogenides*, Ph. D. thesis, Inst. f. Exp. u. Angew. Physik, University Kiel (2003).

[77] J. Kanzow, *Untersuchung der geometrischen und elektronischen Struktur von Heteroschichtsystemen: Epitaktisches* TaS_2 *auf* WSe_2 *und der Fehlanpassungskristall* $(PbS)_{1.14}NbS_2$, Diploma thesis, Inst. f. Exp. u. Angew. Physik, University Kiel (2000).

[78] G. A. Wiegers, A. Meetsma, R. J. Haange, J. L. de Boer, *Structure of Tin Hafnium Sulfide and Lead Hafnium Sulfide*, Acta Cryst. C textbf45, 847 (1989).

[79] J. Barthel, handout sheet, private communication (2008).

[80] J. Barthel: *Ultra-Precise Measurement of Optical Aberrations for Sub-Angström Transmission Electron Microscopy*, Ph.D. Thesis, RWTH-Aachen, Aachen, Germany, 2007.

[81] J. Barthel, handout sheet, private communication (2008).

[82] M. Lentzen, A. Thust and K. Urban: *The error of aberration measurements in HRTEM using Zemlin tableaus*, Microscopy and Microanalysis 10 (Suppl. 2, 2004), 980-981.

[83] W. Hamm: *Hochgenaue Untersuchungen zur Stabilität der Abbildungseigenschaften von hochauflösenden Transmissionselektronenmikroskopen*, Diploma Thesis, RWTH-Aachen, 2008.

[84] E. Spiecker, M. Garbrecht, W. Jäger, K. Tillmann: *Advantages of aberration correction for HRTEM investigation of complex layer compounds*, EM 2008, Zakopane, Poland, J. of Microsc. (submitted).

[85] R. W. Glaisher, A. E. C. Spargo, D. J. Smith: *A systematic analysis of HRTEM imaging of elemental semiconductors*, Ultramicroscopy **27**, 35 (1989).

[86] A. Rosenauer, private communication (2008).

[87] S. Bals, S. Van Aert, G. Van Tendeloo, D. Ávila-Brande: *Statistical Estimation of Atomic Positions from Exit Wave Reconstruction with a Precision in the Picometer Range*, Physical Review Letters **96**, 096106-1, 2006.

[88] A.J. den Dekker, S. Van Aert, A. van den Bos, D. Van Dyck: *Maximum likelihood estimation of structure parameters from high resolution electron microscopy images. Part I: A theoretical framework*, Ultramicroscopy, *104*, 2, pp 83-106, 2005.

[89] S. Van Aert, A.J. den Dekker, A. van den Bos, D. Van Dyck, J.H. Chen: *Maximum likelihood estimation of structure parameters from high resolution electron microscopy images. Part II: A practical example*, Ultramicroscopy, *104*, 2, pp 107-125, 2005.

[90] S. Van Aert, L. Y. Chang, S. Bals , A. I. Kirkland, G. Van Tendeloo: *Effect of Amorphous Layers on the Interpretation of Restored Exit Waves*, Ultramicroscopy, accepted.

[91] M. Kalläne, K. Rossnagel, M. Marczynski-Bühlow, L. Kipp, H.I. Starnberg, S.E. Stoltz: *Stabilization of the misfit layer compound* $(PbS)_{1.13}TaS_2$ *by metal cross substitution*, Physical Review Letters, **100**, 065502, 2008.

List of Publications

E. Spiecker, M. Garbrecht, C. Dieker, U. Dahmen, W. Jäger: *High resolution TEM and diffraction study of layer stacking and long-period undulations in the incommensurate misfit layer compound* $(PbS)_{1.14}NbS_2$, Microsc. and Microanal. **13** (Suppl. 3), 424, 2007.

M. Garbrecht, E. Spiecker, W. Jäger, K. Tillmann: *Aberration-corrected HRTEM of the incommensurate misfit layer compound* $(PbS)_{1.14}NbS_2$, MRS Proceedings Volume 1026E "Quantitative Electron Microscopy for Materials Science", eds. E. Snoeck, R. Dunin-Borkowski, J. Verbeeck, and U. Dahmen, 1026-C10-01, 2007.

Erdmann Spiecker, Dietrich Häußler, Magnus Garbrecht, Wolfgang Jäger: *Quantitative Transmission Electron Microscopy of Interfaces and Nanomaterials*, Proc. 2nd Stanislaw Gorczya ESTEMM Workshop on Electron Microscopy: New TEM Techniques, 1.-4.10.2008, AGH University of Science and Technology, Krakow, Poland (Eds. B. Dubiel, E. Stepniowska, A. czyrska-Filemonowicz, ISBN 978-83-60958-23-0), 31 (2008).

E. Spiecker, M. Garbrecht, W. Jäger, K. Tillmann: *Advantages of aberration correction for HRTEM investigation of complex layer compounds*, EM 2008, Zakopane, Poland, J. of Microsc. (submitted).

List of Conferences

E. Spiecker, M. Garbrecht, C. Dieker, W. Jäger, U. Dahmen, *High-resolution TEM and diffraction study of layer stacking and long-period undulations in the incommensurate misfit layer compound* $(PbS)_{1.14}NbS_2$, MC 2007, Saarbrücken.

M. Garbrecht, E. Spiecker, W. Jäger, K. Tillmann, *Aberration-corrected HRTEM of the incommensurate misfit layer compound* $(PbS)_{1.14}NbS_2$, MRS 2007 Fall Meeting, Boston USA. (Supported by a travel scholarship award from the EMS.)

M. Garbrecht, E. Spiecker, W. Jäger, K. Tillmann: *Aberrationskorrigierte HRTEM an inkommensurablen Grenzflächen in Dichalkogenid-Schichtstrukturen*, AK-HRTEM 2008, Bremen.

M. Garbrecht, E. Spiecker, W. Jäger, K. Tillmann: *Aberration-corrected HRTEM study of incommensurate misfit layer compound interfaces*, EMC 2008, Aachen.

M. Garbrecht, E. Spiecker, W. Jäger, K. Tillmann: *Probenpräparation für aberrationskorrigierte HRTEM von Fehlanpassungsschichten: Anwendungsbeispiele*, LEICA/BAL-TEC Anwendertreffen "Festkörperpräparation"2008, Kiel.

Funding

This work was funded by the German Research Foundation [17].

The misfit samples were fabricated and provided by the surface science group *Electronic Structure and Synchrotron Radiation* of Prof. Dr. Skibowski/ Prof. Dr. Kipp, Inst. of Exp. and Appl. Physics, CAU Kiel, during a collaboration funded by the DFG [18].

A travel scholarship award from the EMS for the MRS Boston 2007 conference is gratefully acknowledged.

Acknowledgement

I want to thank first my supervisor Prof. Dr. Wolfgang Jäger for his continuous support, advice, and the many discussions during the development of this thesis.

My special thanks go to Prof. Dr. Erdmann Spiecker for the experimental help, fruitful scientific discussions and support during the process of my work.

I am most grateful to Dr. Karsten Tillmann and the whole team of the Ernst Ruska-Centre in Jülich for kindly introducing me into the secrets of aberration-corrected HRTEM.

Dr. Dietrich Häußler, who helped me in particular at the beginning of my work with the microscope and the sample preparation deserves also special thanks.

Katrin Brandenburg is gratefully acklowledged for her kind and very helpful manner in the last three years.

Warm thanks go to my Ph. D. fellow Sen.-Eng. M. Sc. Fu Liu, who shared the office with me for a long time and made the daily life in the university much more pleasant.

I am very grateful to all members of the group of Prof. Dr. Föll, especially Dipl.-Ing. Jörg Bahr and Dr. Oliver Riemenschneider for their support in my many technical and hardware/software related questions.

Für die große Unterstützung jedweder Art während meiner gesamten universitären Ausbildung möchte ich meiner Familie und insbesondere Hilmar und Regina danken, die stets ein offenes Ohr für mich hatten und mir mit Rat und Tat zur Seite gestanden haben.

Meine ehemaligen Studienkollegen Andi, Lars, Roland, Jens, Viktor, Bennt und Mu, die mittlerweile über unterschiedlichste Bereiche der Physik verstreut sind, sollen an dieser Stelle im Besonderen Erwähnung finden für den stetigen Austausch und die lehrreichen, fächerübergreifenden Sommer-Symposien in Dänemark.

Für das Durchstehen auch schwierigerer Zeiten gilt zuletzt mein Dank Meike und Emma.

Eidesstattliche Erklärung

Hiermit erkläre ich an Eides statt, diese Arbeit selbständig angefertigt und keine weiteren Hilfsmittel außer den im Text angegebenen, sowie den bekannten Nachschlagewerken der Naturwissenschaften verwendet zu haben.

Kiel, den 22. April 2009.

Magnus Garbrecht